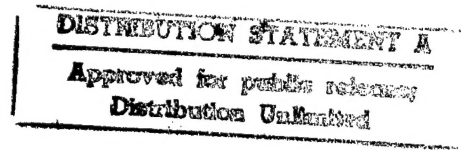


# Center for Ocean Technology

University of South Florida  
St. Petersburg, Florida



## Publications

As appendices to the final report for

### **Development of Sensing Systems and Unmanned Underwater Vehicles for land margin Continental Shelf Oceanographic and Environmental Measurements**

Project no. N00014-94-1-0963

- Ref: (1) Development of an underwater in-situ spectrophotometric sensor for seawater pH
- (2) Laser sensor development for Fluorescence detection of natural and artificial dissolved organic compounds in seawater

18 February, 1997

19970303 115

Prepared by

University of South Florida  
St. Petersburg, Florida

## REPORT DOCUMENTATION PAGE

MOVED  
OMB No. 0704-0188

The reporting burden for this collection of information is estimated to average 1 hour per response, including the time for reviewing instructions, searching existing data sources, gathering and maintaining the data needed and completing and reviewing the collection of information. Send comments regarding this burden estimate or any other aspect of the collection of information, including suggestions for reducing the burden to Washington Headquarters Services, Directorate for Information Operations and Reports, 1215 Jefferson Davis Highway, Suite 1204, Arlington, VA 22202-4302 and to the Office of Management and Budget, Paperwork Reduction Project (0704-0188), Washington, DC 20503.

1. AGENCY USE ONLY (Leave blank)		2. REPORT DATE	3. REPORT TYPE AND DATES COVERED	
		2-18-97	Final Report	7/94 - 7/96
4. TITLE AND SUBTITLE OF REPORT		Development of Sensing Systems and Unmanned Underwater Vehicles for Land Margin Continental Shelf Oceanographic and Environmental Measurements.		
6. AUTHOR(S)		Drs. Thomas Hopkins, Robert Byrne, Kendall Carder, Paula Coble, Kent Fanning, and Albert Hine		
7. PERFORMING ORGANIZATION NAME(S) AND ADDRESS(ES)		University of South Florida 140 Seventh Avenue South St. Petersburg, FL 33701  Dept. of Marine Science		
9. SPONSORING/MONITORING AGENCY NAME(S) AND ADDRESS(ES)		Office of Naval Research Ballston Towers One 800 N Quincy Street Arlington, VA 22217-5660		
11. SUPPLEMENTARY NOTES:				
12a. DISTRIBUTION AVAILABILITY STATEMENT		Unlimited	12b. DISTRIBUTION CODE	
13. ABSTRACT (Maximum 200 words)  Development of sensor, vehicle, communication, computer and integration technologies for multi-sensor, UUV based platforms that will improve Navy capability to characterize the coastal ocean environment.				
14. SUBJECT TERMS			15. NUMBER OF PAGES: 24	
			16. PRICE CODE	
17. SECURITY CLASSIFICATION OF REPORT: Unclassified	18. SECURITY CLASSIFICATION OF THIS PAGE Uncalssified	19. SECURITY CLASSIFICATION OF ABSTRACT Unclassified	20. LIMITATION OF ABSTRACT Unclassified	

## TABLE OF CONTENTS

(1) Development of an <i>In-situ</i> Spectrophotometric Sensor for Seawater pH	1
(2) Development of a Laser-Induced Fluorescence Experiment for the Detection of Trace Compounds in Water Using a Turntable UV-OPO System	9

# Development of an Underwater *In-situ* Spectrophotometric Sensor for Seawater pH

R.D. Waterbury, R.H. Byrne, J. Kelly, B. Leader, S. McElligott and R. Russell

Center for Ocean Technology, Department of Marine Science, University of South Florida  
St. Petersburg, FL 33701

## ABSTRACT

A pH sensor based upon spectrophotometric techniques has been developed for *in-situ* analysis of surface seawater. This sensor utilizes a spectrophotometric pH indicator (Thymol Blue) which has been calibrated for use in seawater as a function of temperature and salinity. Shipboard spectrophotometric pH analyses routinely demonstrate a precision on the order of  $\pm 0.0004$  pH units. *In-situ* analysis of seawater pH has demonstrated a precision on the order of  $\pm 0.001$  and an accuracy, using shipboard measurements as a standard, on the order of  $\pm 0.01$ .

The sensor is a self contained system which pumps seawater, meters in indicator, spectrophotometrically determines indicator absorbance and stores data with a 1Hz acquisition frequency. The sensor employs two absorbance cells, each with three wavelength channels, to obtain the spectrophotometric absorbance. The sensor system, rated for depths up to 500m, provides pH, conductivity, temperature and can be operated via computer or in a standalone mode with internal data storage. The sensor utilizes less than 12 watts of power and is packaged in a 29" long x 4.5" diameter aluminum housing.

Keywords: pH Sensor, Underwater Sensor, Oceanographic Instrument

## 1. INTRODUCTION

### 1.1 Objectives

The goal of this project was development of an *in-situ* sensor with capabilities for examining oceanic pH microstructure. Spectrophotometric procedures have been developed<sup>1,2,3,4,5</sup> for analysis of seawater pH because of the extraordinary precision, convenience and reproducibility of such measurements. Shipboard spectrophotometric pH measurements routinely exhibit a precision of  $\pm 0.0004$  pH units<sup>4</sup>. Alternative procedures for measurement of seawater pH are being developed which will ultimately result in small robust sensors with relatively low sampling frequency (i.e. immobilized dyes on polymer films, etc.). However, to study oceanic microstructure, precise and rapid *in-situ* measurements of seawater pH are required.

### 1.2 Measurement Technique

Thymol blue was selected as an ideal indicator for this project based upon the compatibility of its indicating range with the relatively high pH of the surface ocean. Seawater pH is determined through absorbance, salinity and temperature observations using the following equations:

$$pH_T = pK_2 + \log\left(\frac{R - e_1}{e_2 - R \cdot e_3}\right) \quad (1)$$

$$pK_2 = 4.706 \cdot S / T + 26.3300 - 7.17218 \cdot \log(T) - 0.017316 \cdot S$$

$$e_1 = -0.00132 + 1.600 \times 10^{-5} \cdot T$$

$$e_2 = 7.2326 - 0.0299717 \cdot T + 4.600 \times 10^{-5} \cdot T^2$$

$$e_3 = 0.0223 + 3.917 \times 10^{-4} \cdot T$$

Paper accepted for publication in *Chemical, Biochemical, and Environmental Fiber Sensors VIII*, R.A. Lieberman editor, Proc. SPIE, Vol 2836, 1996.

and  $R = \frac{596}{435} \frac{A}{A}$

where,  $A$  is the optical absorbance of thymol blue at wavelength  $\lambda$  (nm), S is salinity and, T is temperature in °K.

## 2. INSTRUMENT DEVELOPMENT

### 2.1 Design

The design goals for the *in-situ* pH sensor are given in Table 1. As can be seen from eq. (1), seawater temperature, salinity and thymol blue absorbance at two wavelengths are required for the pH determination, and depth is required for sample location. A sketch of the pH sensor is shown in Figure 1 and a functional block diagram is shown in Figure 2. A Falmouth Scientific Conductivity Temperature Depth Probe (CTD) was used to provide the salinity, temperature and depth data.

**Table 1. In-situ pH Sensor Design Goals**

- pH resolution:  $\pm 0.001$
- Operating Depth: 500m
- Measurement frequency: 1Hz
- Standalone or real-time operation
- Data storage within sensor
- Deployment time: 1 hour
- Continuously meter in indicator at constant mix ratio
- Primary indicator is thymol blue--maintain compatibility with other indicators such as *m*-cresol purple

#### 2.1.1 Optical Design

Several different optical sources, elements and detectors were experimentally evaluated. Within size and cost limitations, a design employing interference filters for wavelength selection was given preference over a grating spectrometer. Within each flow cell, absorbance measurements at 3 wavelengths are performed. Two of these wavelengths are directly used for computation (eq. 1) and the third wavelength, in the near-infrared, is used for monitoring high frequency absorbance variations which are not related to thymol blue. An overview of each channel of the optical design is shown in Figure 3. A folded cavity optical design was employed in order to eliminate electrical connections at one end of the optical cavity. This represents a significant savings since underwater feedthroughs and additional pressure bearing chambers add mechanical complexity and cost.

Light Emitting Diodes (LED's) were selected as optical sources for the following reasons: (1) they are commercially available with emitting wavelengths ranging from the low 400nm range up into the near-infrared (considering their wide spectral widths), (2) they are inherently more reliable than incandescent and halogen type lamps, and (3) they are small and inexpensive. In order to improve the collimation of the LED, a 4mm diameter GRIN Lens (NSG America) was butt-coupled to the LED after the plastic lens of the LED was polished away. Given the limited variety of LED's for use in the blue region, a Nichia "1000mcd" LED was selected for our application (peak wavelength 450nm, ~70nm spectral half width). A Toshiba "8000mcd" LED (peak wavelength 590nm, ~90nm FWHM spectral width) was used for the 596nm absorbance measurement.

For our application ( $0.2 \leq A \leq 0.8$ ) we were interested in concentrating as much light as possible onto the detector's active area (2.3mm square), about 12cm from the source. By shortening a .25 Pitch GRIN lens, it was possible to greatly improve the intensity of light on the detector's active area.

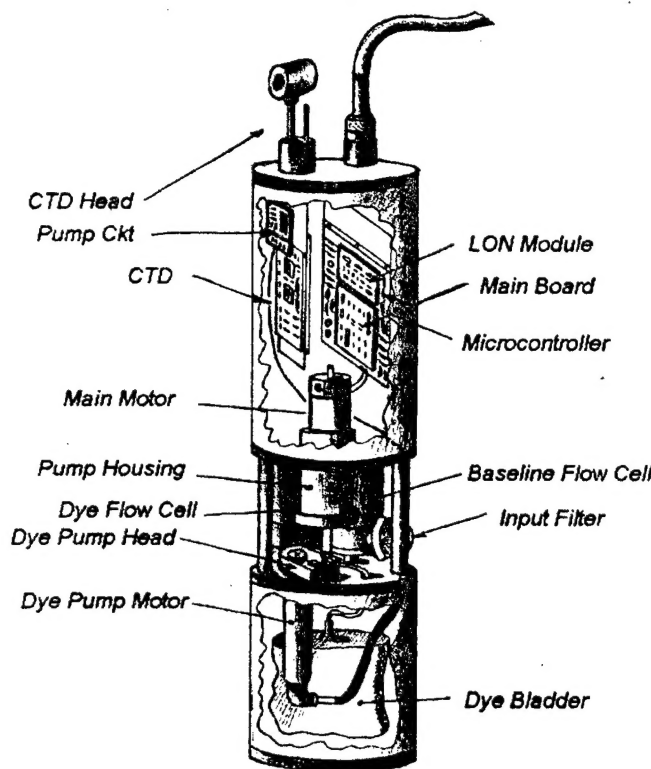


Figure 1. Sketch of pH Sensor

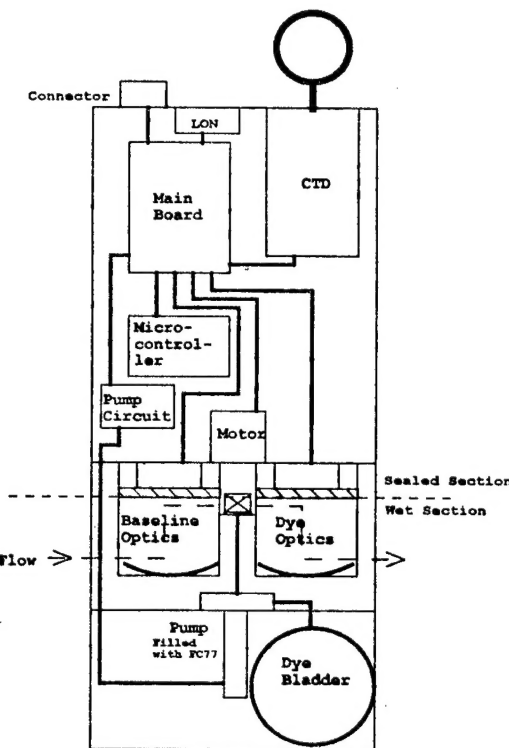


Figure 2. Block Diagram of pH Sensor

A concave second surface spherical mirror with a 50mm focal length folds the light back onto the detector. The light beam intersects the interference filter with a normal angle of incidence. Combination of the non-collimated light source and spherical mirror results in a maximum  $\pm 4^\circ$  deviation from a normal angle of incidence at the interference filter. An integrated photodiode and amplifier (Burr-Brown OPT201) was chosen for its gain, noise and size characteristics.

The absorbance terms ( $^{596}\text{A}$  and  $^{435}\text{A}$ ) in eq. 1, refer to the incremental absorbances due to the addition of thymol blue to seawater. In terms of optical power measurements, the absorbance ratio term can be written as:

$$R = \frac{^{596}\text{A}}{^{435}\text{A}} = \frac{\log(\frac{^{596}P_{wi}}{^{596}P_{wo}})}{\log(\frac{^{435}P_{wi}}{^{435}P_{wo}})} \quad (2)$$

where,  $^{\lambda}P_{wi}$  is the optical power measured with added indicator at wavelength  $\lambda$  and,  $^{\lambda}P_{wo}$  is the optical power measured without indicator (seawater only).

### 2.1.2 Fluid/Mechanical Design

To achieve the goal of one reading per second, a "continuous flow" sensor was employed. This choice resulted in some potentially problematic design features (i.e. separate measurement cells) which we have addressed. The first flow cell performs optical measurements on seawater alone and the second flow cell performs measurements on the seawater/indicator mixture. Inter-cell calibration of the optical measurements between the two flow cells is addressed in a later section.

After reviewing the variety of pumps which could be adapted for underwater applications, an Instech peristaltic pump was selected for delivery of indicator solution with a flow rate of 100  $\mu\text{l}$ iter/minute. Since current laboratory procedures employ a 1000:1 mix ratio between seawater and indicator, the seawater's flow rate was

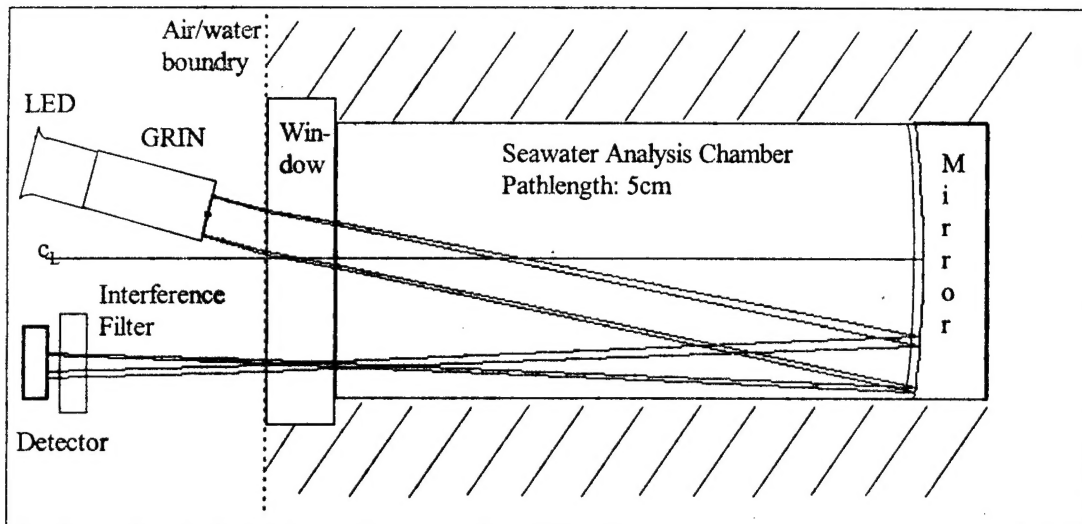


Figure 3. Ray trace of flow cell optics design (only 1 wavelength shown).

initially set to 0.1 liter/minute. The seawater pump (Little Giant) uses a DC motor to drive an impeller type pump head. Turbulence created inside this pump head effectively mixes indicator and seawater.

The sensor was originally designed for deployment in a vertical orientation. In this orientation, attempts to have the sensor automatically expel bubbles were met with limited success. A successful approach to this important problem was devised by deploying the sensor in a horizontal position, having electronic control of the main pump, and performing a predetermined series of starts and stops at normal and faster than normal flow rates.

As seen in Figure 1, the indicator pump is not housed in a pressure vessel. In order to eliminate pressure differentials, and contamination of the motor with seawater, the motor was backfilled with FC-77. This increased the current required to drive the motor from 25ma to 200ma.

The pressure bearing chamber was designed to withstand depths of 500m. Pressure tests demonstrated that the sensor was capable of operation at depths of 650m without catastrophic failure.

### 2.1.3 Electronic Design

A commercially available microcontroller (Blue Earth) was utilized for control within the sensor including communications to a remote computer. Circuitry and software were designed such that the sensor would perform startup operations and calibrations upon entering the water. The startup established the sensor's overall operating mode (i.e. standalone, real-time or data download), initiated a bubble elimination sequence, and provided for CTD initialization. The sensor's electronics utilized a 12 bit A/D converter to digitize six signals, three from each flow cell. The seawater/indicator mix ratio was adjusted from 1000:1 to 2200:1 so that the voltage levels were near the middle of the A/D Converter's range. This promotes the goal of minimizing indicator consumption.

The sensor requires +12V at 1A max. operating conditions. The sensor utilizes RS-422 communication protocol which, in this implementation, is RS-232 compatible. The sensor is also designed to communicate over Echelon's LonWorks Network.

## 2.2 Instrument Evaluation

The instrument is programmed to take absorbance readings once per second. Absorbance acquisition at 1Hz results in pH oversampling for the following reasons. The volume of the flow cells and the flow rate is such that the volume is completely exchanged every 12 seconds. Second, indicator's flow rate is not constant due to 0.25Hz pulsations at the peristaltic pump head. Thus a moving average with a period of 12 seconds, a multiple of both periods, was employed for pH calculations.

### 2.2.1 Inter-cell Calibration

Instead of calibrating each measurement cell independently, cells were calibrated in a relative sense. Accordingly eq. 2 becomes:

$$R = \frac{\log[C_o(\frac{^{596}P_{wi}}{^{596}P_{wo}})]}{\log[C_b(\frac{^{435}P_{wi}}{^{435}P_{wo}})]} \quad (3)$$

with

$$C_o = \left| \frac{^{596}P_{wo}}{^{596}P_{wi}} \right|_{\text{without indicator in system}}$$

and

$$C_b = \left| \frac{^{435}P_{wo}}{^{435}P_{wi}} \right|_{\text{without indicator in system}}$$

It was initially thought that this inter-cell calibration would be required relatively infrequently. However two variables (size and location of bubbles and salt residue on mirrors and windows) dictated an inter-cell calibration on each cast. Inter-cell calibration is performed automatically at the start of a cast by calculating  $C_o$  and  $C_b$  factors prior to pumping indicator into the flow cell. This automatic inter-cell calibration eliminates some of the maintenance which an operator would otherwise perform between casts. In other words, windows and mirrors do not need to be spotless prior to each deployment. Flushing the cells with tap water after each cast is adequate maintenance for this system.

### 2.2.2 Temperature Compensation

Several of the components in the optical measurements require temperature compensation. This compensation is performed by measuring the temperature dependence of each channel and applying compensation factors. With temperature compensation factors, eq. 3 becomes:

$$R = \frac{\log\{C_o[\frac{^{596}P_{wi}(1 - \Delta t \cdot S_{oi})}{^{596}P_{wo}(1 - \Delta t \cdot S_{oo})}]\}}{\log\{C_b[\frac{^{435}P_{wi}(1 - \Delta t \cdot S_{bi})}{^{435}P_{wo}(1 - \Delta t \cdot S_{bo})}]\}} \quad (4)$$

where,  $\Delta t$  is the difference between the temperature at which  $C_o$  and  $C_b$  were determined and the current pH measurement temperature, and the compensation factors,  $S_{bi}$ ,  $S_{oi}$ ,  $S_{bo}$  and,  $S_{oo}$ , are  $-3.8\text{mv}/^\circ\text{C}$ ,  $33.1\text{mv}/^\circ\text{C}$ ,  $2.2\text{mv}/^\circ\text{C}$  and  $22.5\text{mv}/^\circ\text{C}$  respectively.

## 2.3 Standard Deployment

Given the intended mission scenarios and the previously described calibration requirements, standard deployment proceeds as follows. Once power is applied to the sensor, the sensor remains in standby mode until it enters the water. At this point in time, inter-cell calibration and pre-programmed bubble elimination processes are initiated. Since these are critically important processes, the software prescribes a minimum time and depth before the standard measurement mode is initiated. As such, surface water pH is measured only on the up cast. This sacrifice generally results in loss of initial data to a depth of 50m provided the down cast is not extremely rapid. The sensor acquires pH data until it exits the water. For initial deployments the sensor was programmed to repeat the inter-cell calibration every 15 minutes.

The above scenario describes a data logging deployment, in which case sensor data is not monitored real-time and the sensor mission is pre-programmed. With a sensor operating in real-time mode, the sensor can be held just under the surface until the acquisition mode is initiated. In this preferred operating mode the user is in complete control of all sensor functions with optional bypass of predefined setpoints.

## 2.4 Test Results

Several types of experiments were attempted to quantify sensor precision. Unfortunately, we were not able to develop a fully satisfactory laboratory evaluation. In the laboratory it is difficult to insure that a large tank of water has constant pH over a long experiment in which the sensor is discharging thymol blue into the test tank. Other effects such as CO<sub>2</sub> exchange between the atmosphere and water also may effect pH in the thousandths and ten-thousandths of a pH unit range. Figure 4 shows a graph of the absorbance ratio term (R) and pH using domestic Floridian tap water. For this type of precision evaluation, tap water actually amplifies the imprecision of the instrument compared to seawater. The sensitivity of pH with respect to the absorbance ratio ( $\partial\text{pH}/\partial R$ ) is  $\sim 3$  for an absorbance ratio in typical tap water ( $0.1 \leq R \leq 0.2$ ) while,  $\partial\text{pH}/\partial R$  is 1 or slightly less for absorbance ratios in surface seawater ( $0.5 \leq R \leq 1$ ). This highlights the fact that sensor pH precision is dependent upon pH and that different indicators have different optimal indicating ranges. For our low pH test system, the precision of the absorbance ratio can be used to assess pH sensor precision in the surface ocean. This is a reasonable evaluation for thymol blue in surface seawater, because  $(\partial\text{pH}/\partial R) \approx 1$ . Figure 4 indicates that the standard deviation of the absorbance ratio is in the range of  $\pm 0.0002$  to  $\pm 0.0008$ . While more definitive experiments need to be performed, this precision is within the  $\pm 0.001$  pH unit design goal of the instrument.

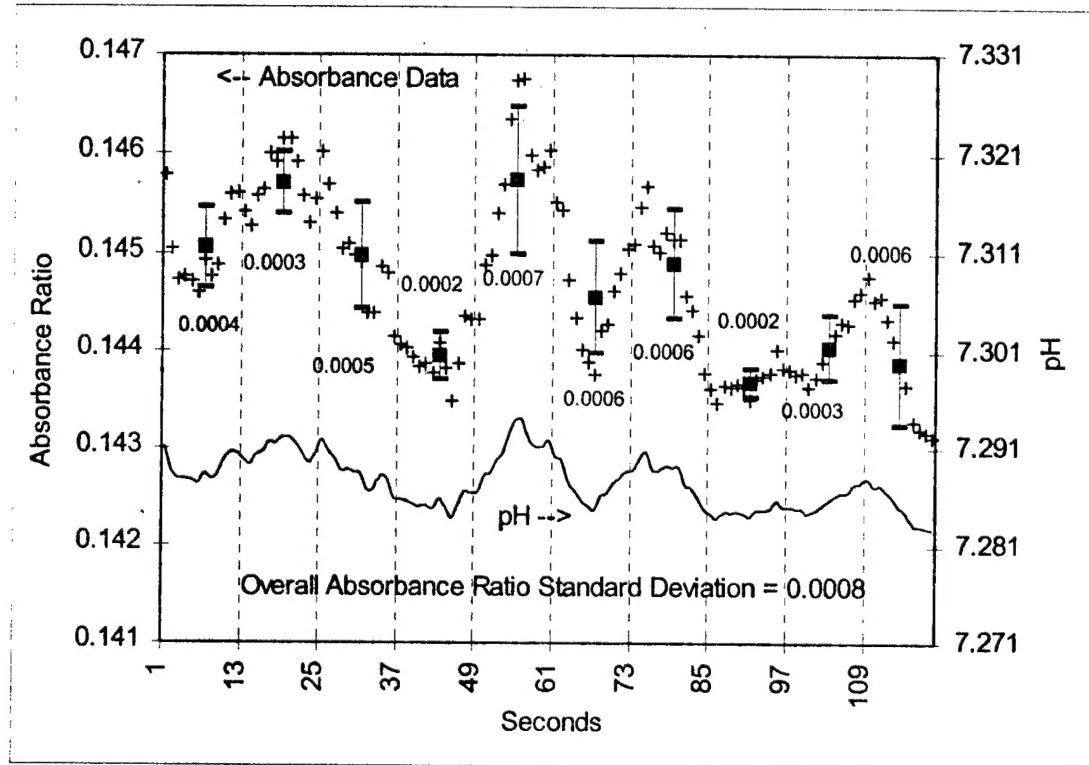


Figure 4. Absorbance Ratio and pH for domestic tap water. Absorbance ratio data include 1-sigma error bars. Standard deviation is calculated for 10 sets of 12 readings.

## 2.5 Cruise Results

The sensor was deployed in the South Pacific and Antarctic Oceans during NOAA CO<sub>2</sub>-system investigations (Jan. - Mar. 1996) aboard the R/V Discoverer. The sensor was deployed once a day for a total of roughly 60 casts. Figure 5 shows the pH, salinity and temperature recorded on two casts. Most of the casts' pH distributions had similar shapes. This figure exhibits some of the oceanic CO<sub>2</sub>-system microstructure which can be revealed with precise *in-situ* pH instrumentation.

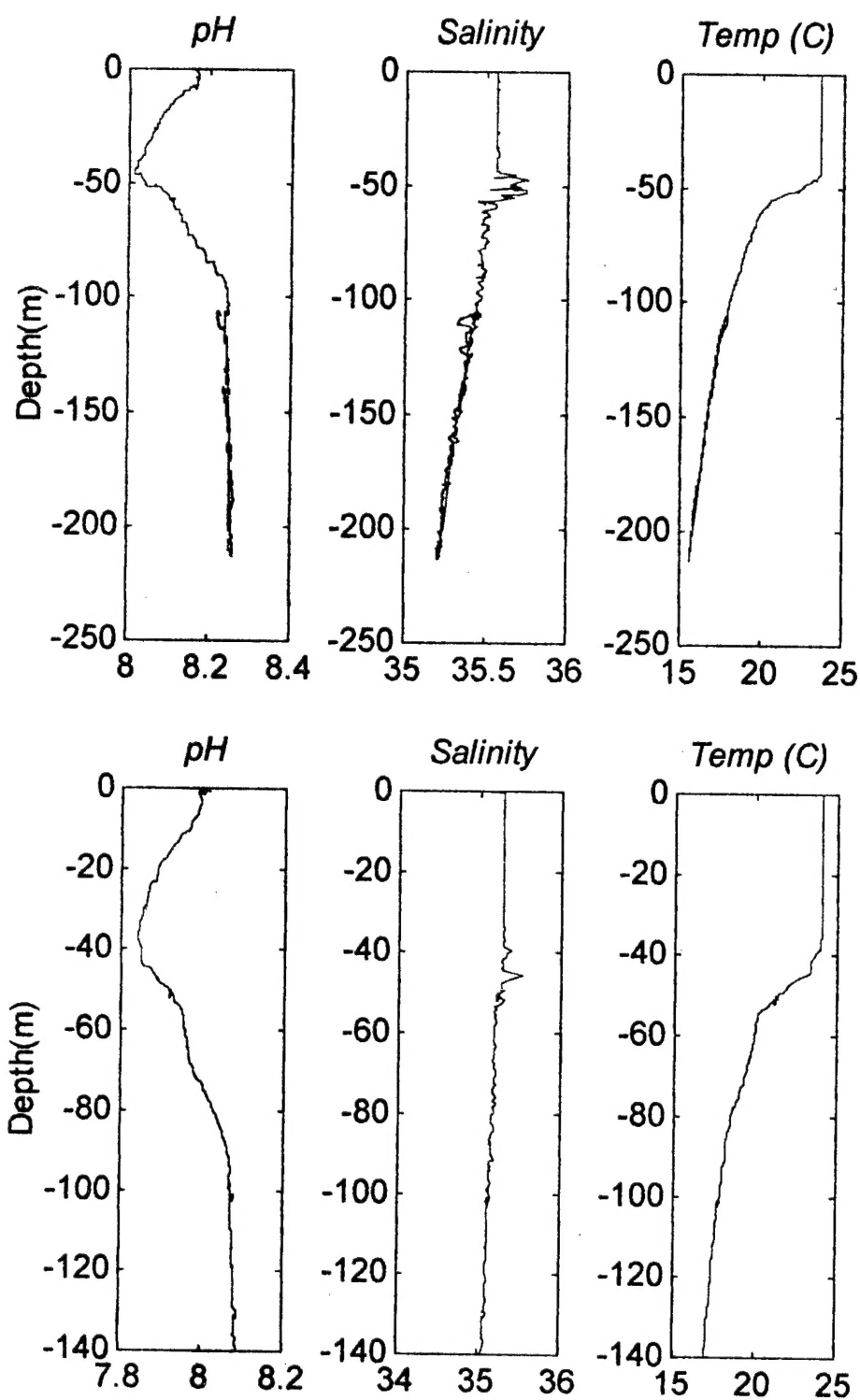


Figure 5. Typical pH, Salinity and Depth profiles from the South Pacific and Antarctic Oceans

### **3. FUTURE ENHANCEMENTS**

Various features of the present system allow for improvement in the quality of *in-situ* measurements. Several casts in the South Pacific did not provide useful data because the main pump and/or the indicator pump jammed. The motor controllers for these two pumps are being fitted with over-current indicators so that a "safe shutdown" can be effected when an error condition exists. In the laboratory, flow rate measurement is difficult since the measurement technique introduces sufficient back pressure to retard the flow rate slightly. The main pump head is being redesigned to make it more robust.

While the second surface mirrors perform adequately in current applications, improvement in the reliability of this sensor is required for long term deployments at sea (i.e. 6 months). In long term deployments, the optical cavity will be unfolded, thereby eliminating the mirror for this application. It is desirable, for most all applications, that the sensor has a "power down" mode with minimal power consumption. The necessary circuitry can be redesigned to "power down" on as little as 60mW.

While the near infrared channels are used for gross bubble detection, there is also hope that such measurements can be used to eliminate scattering effects of the water as employed in other absorption meters<sup>6,7</sup>. Further assessment of our *in-situ* data set is being used to better understand the influence of scattering on absorbance ratio observations.

### **4. CONCLUSIONS**

The *in situ* pH sensor described here provides continuous profiles of seawater pH to 500m. While additional experiments are needed to better assess our instrument's true precision, the system's short term 3-sigma precision is currently no worse than .003 pH units. Additional activities are planned to improve the instrument's precision until it closely approaches that of shipboard measurements.

### **5. ACKNOWLEDGMENTS**

This work was supported by the Office of Naval Research through Grant No. N00014-94-0963 and the National Oceanic and Atmospheric Administration through Grant No. NA56GP0305

### **6. REFERENCES**

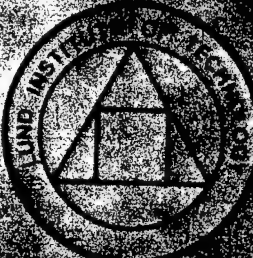
1. G.L. Robert-Baldo, M.J. Morris and R.H. Byrne, "Spectrophotometric Determination of Seawater pH Using Phenol Red," *Analytical Chemistry*, 57, 2564-67, 1985.
2. R.H. Byrne, "Standardization of Standard Buffers by Visible Spectrometry," *Analytical Chemistry*, 59, 1479-81, 1987.
3. R.H. Byrne and R.H. Breland, "High Precision Multiwavelength pH Determinations in Seawater Using Cresol Red," *Deep-Sea Research*, 36(5), 803-10, 1989.
4. T.D. Clayton and R.H. Byrne, "Spectrophotometric pH Measurements: Total Hydrogen Ion concentration Scale Measurements and At-Sea Results," *Deep-Sea Research*, 40, 2315-29, 1993.
5. H. Zhang and R.H. Byrne, "Spectrophotometric pH Measurements of Surface Seawater at *In-situ* Conditions: Absorbance and Protonation Behavior of Thymol Blue," *Marine Chemistry*, 52, 17-25, 1996.
6. J.R.V. Zaneveld, J.C. Kitchen, A. Bricaud and C. Moore, "Analysis of *in situ* spectral absorption meter data," in *Ocean Optics XI*, Gary D. Gilbert, Editor, Proc. SPIE 1750, 187-99 (1992).
7. J.R.V. Zaneveld, J.C. Kitchen, and C. Moore, "The Scattering Error Correction of Reflecting-Tube Absorption Meters," in *Ocean Optics XII*, Jules S. Jaffe, Editor, Proc. SPIE 2258, 44-55 (1994).

Lund Reports on Atomic Physics

**Development and Evaluation of a Laser-  
Induced Fluorescence Experiment for the  
Detection of Trace Compounds in Water Using  
a Tuneable UV-OPO System**

Master Thesis  
by  
Magnus Bengtsson and Lars-Gunnar Nilsson

Lund Reports on Atomic Physics, LRAP-197  
Lund, June 1996



## ABSTRACT

An experimental set-up for the detection of dissolved organic matter (DOM) in seawater by means of Excitation Emission Matrix (EEM) laser-induced fluorescence spectroscopy has been constructed and evaluated. The evaluation included a characterisation of the commercial frequency doubled BBO OPO-system that was used as a light source to generate continuously tuneable UV laser light over the wavelength range of 220 nm to 340 nm at an output energy of 1-10 mJ. The detection of the entire fluorescence spectrum was accomplished using a CCD, mounted on a single grating spectrometer. Testing and evaluation of the set-up was carried out using a quinine sulphate fluorescence standard. The sensitivity of the method and the observation of limiting factors such as photochemical destruction were studied. Of importance is the preliminary measurement of EEM spectra of plastic compound contaminants dissolved in water which demonstrated the sensitivity and selectivity of the system for the first time.

## Errata

<u>Page</u>	written	should be
40, <i>Fig. numbers</i>	4.9, 4.10	4.11, 4.12
41, <i>Fig. numbers</i>	4.11	4.13
41, <i>first paragraph</i>	Figure 4.11	Figure 4.13
65, <i>Fig. 7.7</i>	(14)	(55)
76, <i>Fig. 9.4-5, Captions</i>	<i>Fig. 9.4 is for low power excitation and vice versa</i>	

## TABLE OF CONTENTS

CHAPTER 1. INTRODUCTION	1
1.1 Optical Parametric Oscillators	1
1.2 Laser-Induced Fluorescence	2
1.3 Thesis Outline	3
CHAPTER 2. OPO THEORY	5
2.1 Nonlinear Optical Interactions	5
2.2 Induced Polarisation	6
2.3 Parametric Amplification	7
2.4 Nonlinear Materials and Phase Matching	10
2.5 Optical Parametric Oscillator	12
2.6 Tuning Curves	13
2.7 Properties of Nonlinear Crystals	14
2.8 Injection Seeding	17
CHAPTER 3. MOPO DESCRIPTION	19
3.1 GCR-250 Nd:YAG Pump Laser	20
3.2 Spectra-Physics 730-10 MOPO	22
3.2.1 The Master Oscillator	23
3.2.2 The Power Oscillator	26
3.2.3 Optical Beam Path within the MOPO	26
3.3 Frequency Doubling of OPO	27
3.4 Electronic Operation and Look-up Tables	30
CHAPTER 4. OPTICAL DIAGNOSTICS OF OPO SYSTEM	33
4.1 Characterisation Measurements	33
4.2 Troubleshooting and Experience	41
CHAPTER 5. BACKGROUND THEORY: LASER-INDUCED FLUORESCENCE	45
5.1 Basic Fluorescence Theory	45

# CHAPTER 1

## INTRODUCTION

### 1.1 Optical Parametric Oscillators

Optical parametric oscillators (OPOs) are powerful optical sources of broadly tuneable coherent radiation ranging from the near UV to the mid IR part of the spectrum. The light generated by OPOs has the characteristics of laser light, and the tunability makes it easy to reach wavelength regions where there are no lasers readily available. Hence, these devices have many potential applications in research and industry.

Optical parametric oscillators are by no means new devices, with the theory of OPOs having been developed in the early 1960's by Kroll [29] and by Armstrong et al. [3]. The first demonstration of optical parametric oscillation was made in 1965 by Giordmaine and Miller [18]. The potential of a tuneable source of coherent radiation was clear from the beginning, however the lack of suitable nonlinear optical materials hindered the development of practical OPOs. The recent development of new, high quality optical materials such as potassium titanyl phosphate (KTP) [59],  $\beta$ -barium borate (BBO) [10] and lithium borate (LBO) [8] has led to renewed interest in OPOs. Today there are several commercial OPO-systems available.

An OPO uses a high-power laser pump beam and a nonlinear optical material to convert each high frequency pump photon into two lower frequency photons, called signal and idler photons. Energy conservation requires that the sum of the signal and idler frequencies be equal to the pump frequency. The nonlinear optical material usually sits in an optical cavity. The signal or idler or both frequencies may be resonant in the cavity but the pump frequency is not. If the gain of the resonant frequency is higher than its losses, oscillation will occur. The frequencies of the generated photons are determined by the so called phase-matching condition, which is a momentum conservation condition. By changing the phase-matching condition in the nonlinear optical material, different output frequencies will be generated. The OPO looks similar to a laser with an optical cavity and a gain medium inside it, but unlike the laser there is no energy storage in an OPO. The process is instantaneous and only takes place while the pump beam is present. The nonlinear processes require high optical intensities in order to be efficient. Because of this, OPOs are almost always pulsed systems.

We used a frequency doubled OPO in our experiments as a source of tuneable UV radiation in the wavelength region 220-330 nm to conduct laser-induced fluorescence (LIF) experiments of com-pounds in seawater. The fluorescence method used required tuneable output or at least many different excitation wavelengths. In order to gain a better understanding of the OPO and its functions, we performed several measurements on the output. These were measurements that sought to characterise the OPO output, such as linewidth, output power, temporal characteristics, etc.

The OPO used in our experiments was a Spectra-Physics 730-10 MOPO pumped by a frequency tripled Q-switched Nd:YAG laser at 355 nm. The OPO-system was equipped with a frequency doubler and was able to produce tuneable output ranging from 220 nm to 2  $\mu$ m.

## 1.2 Laser-Induced Fluorescence

Fluorescence has been widely used for the past 50 years in both environmental and oceanographic applications as a method to detect and analyse trace compounds in gases, liquids and solids. It has been used to measure a wide variety of trace species including pollution of groundwater and surface waters by petroleum products and pesticides, chlorophyll and yellow-coloured dissolved organic matter in the ocean and has been shown to be one of the best single indicators of the origin of crude oil. [2,51,56]

Usually, fluorescence optical instruments use conventional UV light sources to excite the trace species. However, during the past 10 to 20 years, UV lasers have become available that offer some advantages over the conventional light sources in intensity and spectral linewidth. As such lasers are now widely used for UV fluorescence detection of selected species especially for very low concentrations (ppt or lower).

Recently, a new spectrometric technique has been developed which shows the variations in the fluorescence output spectrum as a function of both the excitation and emission wavelength. This technique is called Excitation-Emission Matrix (EEM) spectroscopy and gives more information and selectivity of the trace species compared to the background fluorescence spectrum. Figure 1.1 shows an example of an EEM spectrum. As can be seen in Fig. 1.1, the specific fluorescence signature of the species is easily detected as the excitation wavelength is changed.

5.2	Laser-Induced Fluorescence Set-up	48
5.3	The Ideal Fluorescence Equation	49
<b>CHAPTER 6. TRANSMISSION AND EFFICIENCY CONSIDERATIONS FOR LIF DETECTION OPTICS</b>		53
6.1	Properties of the Atmosphere	53
6.2	Lens Collection System	54
6.3	Transmission of Optical Materials	56
6.4	Properties of Monochromators and Detectors	58
<b>CHAPTER 7. PREVIOUS FLUORESCENCE MEASUREMENTS OF QUININE SULPHATE AND COMPOUNDS IN WATER</b>		61
7.1	Optical Properties of Water	61
7.2	Fluorescence of Organic and Plastic Compounds in Water	62
7.3	Use of Quinine Sulphate as a Standard	64
<b>CHAPTER 8. LASER-INDUCED FLUORESCENCE EXPERIMENTAL SET-UP</b>		67
8.1	Laser Source	68
8.2	Cuvet and Collection Optics	68
8.3	Spectrometer	69
8.4	CCD Detector	70
8.5	Spectrometer Control and CCD Data Processing	71
8.6	Alignment and Calibration Procedures of Spectrometer and CCD	72
<b>CHAPTER 9. LASER-INDUCED FLUORESCENCE EXPERIMENTS</b>		73
9.1	LIF Measurements of Quinine Sulphate	73
9.2	Measurements of Photobleaching and Possible Saturation	75
9.3	Noise Measurements	77
9.4	Measurements of Different Water Samples	80
9.5	Comparison between Different Concentrations of Quinine Sulphate	82
9.6	Signal to Noise Ratios	85

CHAPTER 10. TUNEABLE UV LASER EXCITATION-EMISSION MATRIX (EEM) EXPERIMENTS	87
10.1 EEM for Quinine Sulphate	87
10.2 EEM for a Plastic Contaminant Dissolved in Water	88
CHAPTER 11. CONCLUSIONS AND FUTURE WORK	91
ACKNOWLEDGEMENTS	93
LIST OF REFERENCES	95
APPENDIX A. ALIGNMENT PROCEDURE FOR UV FLUORESCENCE SET-UP	99

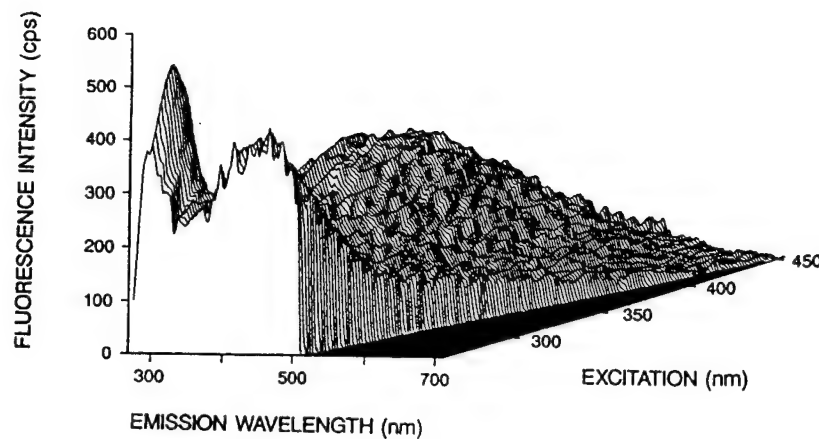


**Figure 1.1** A typical EEM spectrum showing the specific profile of a couple of different compounds in seawater. [11]

Using a laser as an excitation source in EEM spectroscopy has an evident purpose - to increase the sensitivity and the signal to noise ratio (SNR). Tuneable laser sources in the UV region are rare. Wavelengths down to 320 nm can be obtained with dye lasers. The problem is that the dye has to be changed over the wavelength region and that the dyes may be cancerous. With the advent of tuneable OPOs, it became possible to scan continuously over the desired wavelength region. Wavelengths in the UV region are accomplished either by frequency doubling, as used in our experiments, or by frequency mixing.

### 1.3 Thesis Outline

Our thesis consists of LIF spectroscopy experiments using a new frequency-doubled, tuneable, narrow-linewidth OPO. The fluorescence signal was detected with a CCD camera. Quinine sulphate was mostly used as a sample because of the well known fluorescence properties of the substance. The purpose of our study was to investigate the sensitivity and SNR of the system and to some extent compare the results with a commercial spectrofluorometer system used for fluorescence detection of several contaminants in water. Overall, our EEM and LIF experiments were successful, but also indicated some new effects, involving photodestruction.

The results of our study are given in the following chapters. Chapter 2 contains a theoretical description of how an OPO works. Chapter 3 is a description of the Spectra Physics OPO system that was used and Chapter 4 describes the measurements that were made to characterise the OPO system; our experiences and problems with the system are also discussed. Chapter 5 is a theoretical background of LIF theory. Chapter 6 contains a description of

optics, spectrometers and detectors that may be used in LIF experiments. Chapter 7 gives a background of previous studies of fluorescence of water and the use of quinine sulphate as a standard. Chapter 8 describes the experimental set-up that was used in our measurements. Chapter 9 contains LIF experimental results. A discussion about photodestruction, saturation and noise is also included. Chapter 10 contains EEM fluorescence spectra of quinine sulphate and a plastic contaminant dissolved in water. Conclusions made from this research and suggestions for future work in this area are given in Chapter 11.

This work was conducted in the Laser Laboratory at the University of South Florida under a joint co-operative research study with Lund Institute of Technology.

However only one, if any, of these frequencies will be present with an appreciable intensity. This restriction is imposed by the conservation of momentum, also called the phase-matching condition in nonlinear optics.

### 2.3 Parametric Amplification

Before we look at OPOs, we will study a process known as optical parametric amplification (OPA). In this scenario three optical waves with frequencies  $\omega_1$ ,  $\omega_2$  and  $\omega_3$  interact in a lossless nonlinear medium. A high intensity pump beam, with frequency  $\omega_3$ , is used to amplify a weaker signal beam with frequency  $\omega_1$  ( $\omega_3 > \omega_1$ ). Energy conservation require that a third frequency  $\omega_2$  is generated in the process. Mathematically, energy conservation is written as  $\omega_3 = \omega_1 + \omega_2$ . Conservation of momentum also has to be fulfilled, as described by

$\mathbf{k}_3 = \mathbf{k}_1 + \mathbf{k}_2$ , where  $\mathbf{k}_i$  is the wave propagation vector. A schematic of this process is shown in Fig. 2.1.

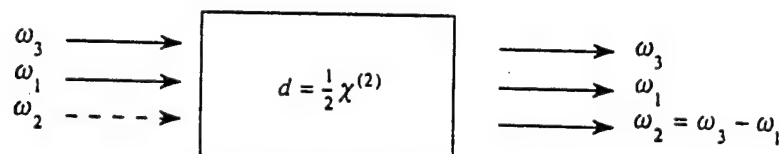


**Figure 2.1** Schematic of parametric amplification. The electromagnetic fields interact via the nonlinear susceptibility of the material. [6]

Here follows brief mathematical description of optical parametric amplification. More detailed derivations can be found in [4,6,42]. The incident fields are

$$\begin{aligned}\tilde{E}_3(t) &= E_3 e^{i(k_3 z - \omega_3 t)} && \text{(pump)} \\ \tilde{E}_1(t) &= E_1 e^{i(k_1 z - \omega_1 t)} && \text{(signal)}\end{aligned}\tag{2.5}$$

where

$$k_i = \frac{n_i \omega_i}{c}, \quad n_i = \sqrt{1 + \chi^{(1)}(\omega_i)}, \tag{2.6}$$

and where  $E_i$  is the amplitude. We make the following approximations:

- Slowly varying amplitude approximation, stating that the change in the amplitude of the fields over a wavelength is negligible.
- The conversion efficiency is low, i.e. only a fraction of  $\tilde{E}_3(t)$  is used, so that its amplitude can be considered constant. This is called the undepleted pump approximation.

With these approximations the wave equation, Eq. (2.3) can yield a set of coupled differential equations that describe the growth of the signal and idler amplitudes,  $E_1$  and  $E_2$  respectively, as [4,6,42]

$$\begin{aligned}\frac{dE_1}{dz} &= -i\eta_1\omega_1 d_e E_3 E_2^* e^{-i\Delta kz} \quad (\text{signal}) \\ \frac{dE_2^*}{dz} &= i\eta_2\omega_2 d_e E_3 E_1^* e^{i\Delta kz} \quad (\text{idler})\end{aligned}\tag{2.7}$$

where

$$\Delta k = k_3 - k_1 - k_2,\tag{2.8}$$

$\eta_i$  is the impedance of the medium, and  $d_e$  is an effective nonlinear (scalar) coefficient, calculated from  $\chi^{(2)}$  [6]. If  $\Delta k$ , called the phase mismatch, is zero the growth of the signal will be

$$I_1 = I_{10} \cosh^2(\Gamma l),\tag{2.9}$$

where  $I_1$  is the intensity of the amplified beam,  $I_{10}$  is the intensity of the incident beam,  $l$  is the length of the nonlinear medium, and the gain coefficient,  $\Gamma$  is defined by the equation

$$\Gamma^2 = \frac{4\pi^2 d_e^2 |E_3|^2}{n_1 n_2 \lambda_1 \lambda_2}.\tag{2.10}$$

where  $n_1$  and  $n_2$  are the refractive indices of the signal and idler, and  $\lambda_1$  and  $\lambda_2$  are their free-space wavelengths. Equation (2.9) implies that both the signal and idler experience approximately exponential growth in the low conversion limit, i.e. when the pump beam is undepleted.

## CHAPTER 2

### OPO THEORY

The theory of Optical Parametric Oscillators (OPOs) has been reviewed by several authors [3,4,6,29,42]. In this chapter a brief overview of this theory is presented. Also, the optical properties of some of the materials used in nonlinear optics are covered. All equations are given in SI (MKS) units.

#### 2.1 Nonlinear Optical Interactions

Nonlinear optical interactions are processes in which the intensity of the optical field modifies the optical properties of a material system. Although there are many different types of nonlinear optical interactions, in this section we will give a brief background to the nonlinear interactions important in an optical parametric oscillator (OPO), namely the generation of new frequencies.

The propagation of electromagnetic waves through space can be described by the wave-equation, which is derived from Maxwell's equations. In vacuum for example, this equation becomes [9]

$$\nabla^2 \tilde{\mathbf{E}} - \frac{1}{c^2} \frac{\partial^2 \tilde{\mathbf{E}}}{\partial t^2} = 0, \quad (2.1)$$

where  $\tilde{\mathbf{E}}$  is the electric field strength and  $c$  is the speed of light. The tilde in Eq. (2.1) is used to denote a quantity which varies rapidly in time. For the case of a wave propagating in an optical medium where there are no free charges or currents, the material is nonmagnetic and the electric displacement  $\tilde{\mathbf{D}}$  and the polarisation  $\tilde{\mathbf{P}}$  are related by [6,9]

$$\tilde{\mathbf{D}} = \epsilon_0 \tilde{\mathbf{E}} + \tilde{\mathbf{P}}. \quad (2.2)$$

In this case, the wave equation can be written as [6]

$$\nabla \times \nabla \times \tilde{\mathbf{E}} + \frac{1}{c^2} \frac{\partial \tilde{\mathbf{E}}}{\partial t^2} = -\frac{\eta_0}{c} \frac{\partial^2 \tilde{\mathbf{P}}}{\partial t^2}. \quad (2.3)$$

This expression can be interpreted as an inhomogenous wave equation where the polarisation  $\tilde{\mathbf{P}}$  drives the electric field,  $\tilde{\mathbf{E}}$ .  $\tilde{\mathbf{P}}$  may contain components of other frequencies than those of the original electric field and these components will generate electric fields with their own frequencies. We will take a closer look at  $\tilde{\mathbf{P}}$  to try to understand how new frequencies can be generated.

## 2.2 Induced Polarisation

The linear response of a lossless and dispersionless dielectric<sup>1</sup> is an induced polarisation which can be written as [6]

$$\tilde{P}(t) = \epsilon_0 \chi^{(1)} \tilde{E}(t), \quad (2.3)$$

where  $\tilde{P}(t)$  is the induced polarisation,  $\epsilon_0$  is the permittivity of free space,  $\chi^{(1)}$  is the linear susceptibility and  $\tilde{E}(t)$  is the electric field strength. In a nonlinear material, the response can often be written as a power series in the electric field as [6]

$$\begin{aligned} \tilde{P}(t) &= \epsilon_0 (\chi^{(1)} \tilde{E}(t) + \chi^{(2)} \tilde{E}^2(t) + \chi^{(3)} \tilde{E}^3(t) + \dots) = \\ &= \tilde{P}^{(1)}(t) + \tilde{P}^{(2)}(t) + \tilde{P}^{(3)}(t) \dots \end{aligned} \quad (2.4)$$

$\chi^{(2)}$  and  $\chi^{(3)}$  are called the second and third order susceptibilities, respectively. In the general case where  $\tilde{P}(t)$  and  $\tilde{E}(t)$  are vector quantities and not scalars, the susceptibilities will be tensors. In this model  $\chi^{(2)}$  is responsible for second harmonic generation,  $\tilde{P}^{(2)}(t)$  will contain components with twice the frequency of the incident electric field  $\tilde{E}(t)$  because of the squared term. If there are two different incident frequencies  $\tilde{P}^{(2)}(t)$  will also contain the sum- and difference-frequencies of these fields. All in all  $\tilde{P}^{(2)}(t)$  will contain four different nonzero frequencies, and as stated above  $\tilde{P}^{(2)}(t)$  will then generate electric fields at these frequencies.

---

<sup>1</sup> This allows us to say that the polarisation only depends on the instantaneous value of the electric field. [6,28]

$$\frac{1}{n_e(\theta)^2} = \frac{\sin^2(\theta)}{n_e^2} + \frac{\cos^2(\theta)}{n_o^2}. \quad (2.13)$$

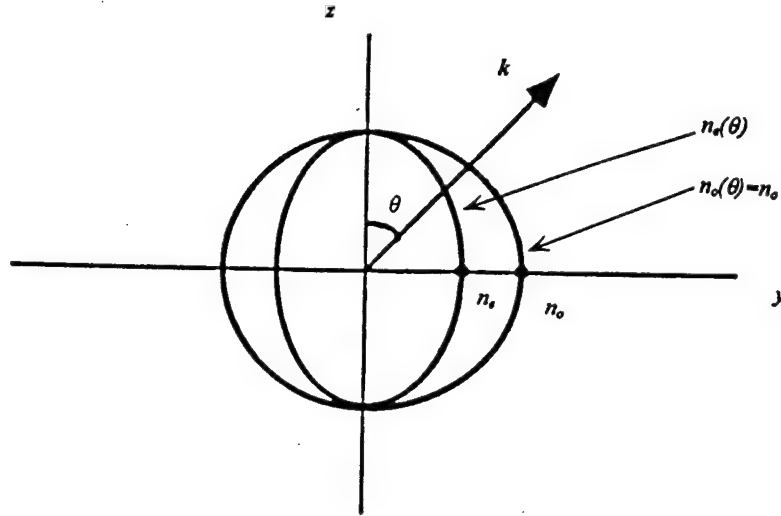


**Figure 2.3** Birefringence in a negative uniaxial crystal.  $z$  is parallel to the optic axis and  $\theta$  is the angle between the optic axis and the propagation vector  $k$ . [57]

In order to achieve phase matching in a birefringent crystal, the highest-frequency wave  $\omega_3 = \omega_1 + \omega_2$ , is polarised in the direction that gives the lower of the two possible refractive indices. In a negative uniaxial crystal the pump beam should have the extraordinary polarisation direction. The phase matching condition can then be changed by changing of the angle between the optic axis and the wave propagation vector.

Phase matching of two different frequencies,  $\omega$  and  $2\omega$ , in a negative uniaxial crystal is shown in Fig. 2.4. At the angle  $\theta$   $n_e(2\omega)$  equals  $n_o(\omega)$  and phase matching can be achieved. This case is easier to illustrate graphically because only two waves interact. The phase matching condition in this case is

$$n_e(2\omega, \theta) \cdot 2\omega = n_o(\omega)\omega + n_o(\omega)\omega \Rightarrow n_e(2\omega, \theta) = n_o(\omega). \quad (2.14)$$

In an OPO, where there are three fields interacting, the polarisation of the lower-frequency fields can be chosen in two ways, if the waves have the same polarisation it is referred to as Type I, and referred to as Type II if the waves have orthogonal polarisations.

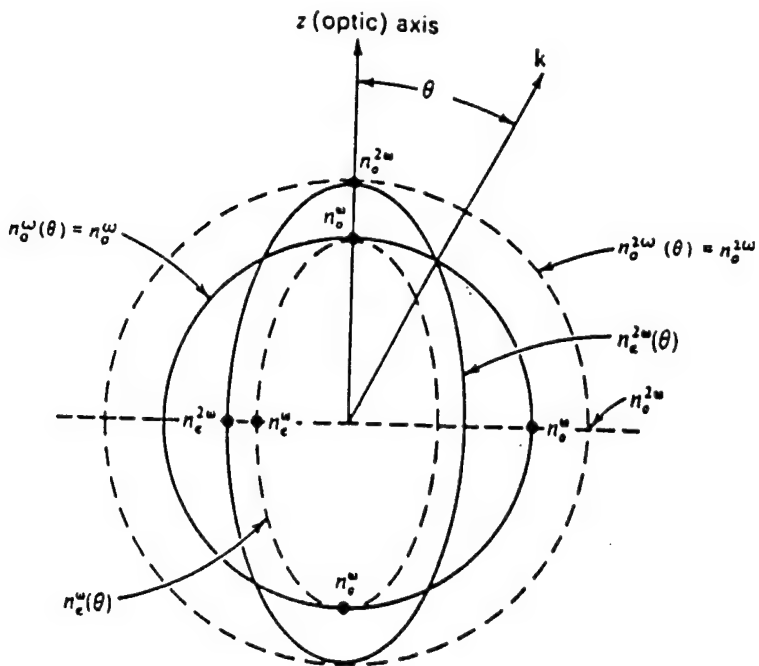


**Figure 2.4** Phase matching at angle  $\theta$  of two waves with different frequencies,  $\omega$  and  $2\omega$ , in a negative uniaxial crystal. [57]

## 2.5 Optical Parametric Oscillators

In an OPO, we take the OPA process and add an optical cavity as shown in Fig. 2.5. The mirrors of the cavity are highly reflectant at one of the signal and idler frequencies (sometimes both) but not at the pump frequency. Oscillation will occur if the gain inside the nonlinear medium of the resonant frequency is greater or equal to the losses at the mirrors. In a

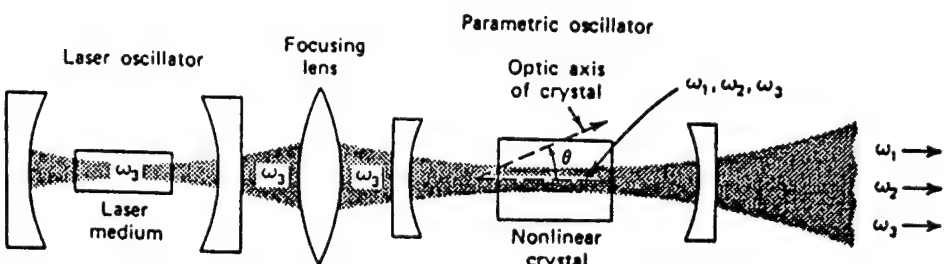


**Figure 2.5** Schematic diagram of an OPO which is pumped by a laser at frequency  $\omega_3$ . The optical cavity is resonant at frequency  $\omega_2$  or  $\omega_1$ . [57]

pulsed OPO, a gain much higher than the cavity losses is necessary to achieve an observable output. A thorough discussion of thresholds can be found in [4,42]. In a pulsed OPO, the

In the case of high conversion, the solution will take the form of Jacobi elliptic functions and this solution can be found in e.g. [3,42]. The case where  $\Delta k=0$  is called perfect phase matching. If  $\Delta k$  is nonzero, frequency conversion is still possible but the efficiency decreases rapidly with increasing  $\Delta k$ . There will also be a maximum effective length of the interaction, after which the energy will start flowing from the signal and idler beams back into the pump beam.

As can be seen in Eq. (2.10), the intensity of the pump beam ( $I_3 \propto |E_3|^2$ ) plays an important role in the conversion efficiency. Figure 2.2 shows how the gain in a AgGaSe<sub>2</sub> crystal varies with pump pulse peak power.

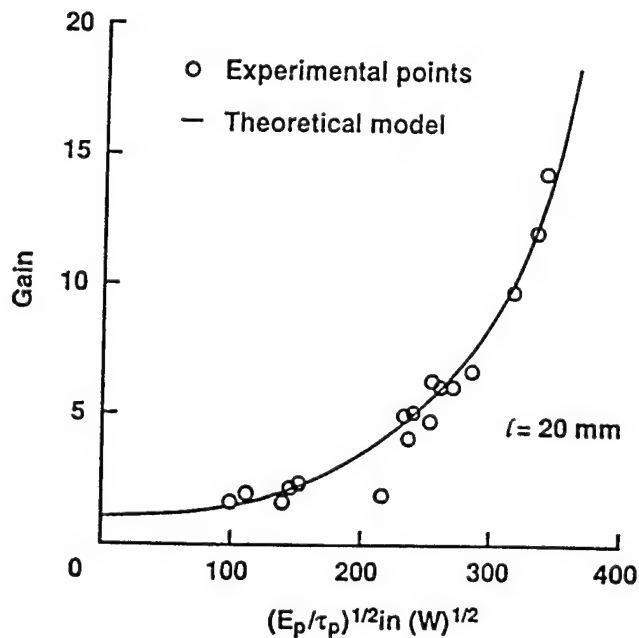


**Figure 2.2** Single-pass gain of an OPA as a function of input pump power, shown for the case of a 3.39  $\mu\text{m}$  HeNe laser beam in a AgGaSe<sub>2</sub> crystal pumped by a 1.73  $\mu\text{m}$  pulsed Er:YLF laser. The gain was measured at the peak of the pump pulse as a function of  $E_p/\tau_p$  where  $E_p$  is the pump energy and  $\tau_p$  is the pulse length. [4]

In optical parametric amplification at least one of the two lower frequency components is nonzero initially and the subsequent amplification can be described by our equations. If there is no lower frequency field present it would still be possible to generate lower frequencies starting with just the pump beam and amplifying noise photons created by parametric scattering. In the parametric scattering process the initial number of photons at  $\omega_1$  and  $\omega_2$  are zero.

The above theory, however, does not suffice since it only describes interaction of already existing fields. This nonlinear optical emission can be properly described only by quantizing the fields. [42].

The word parametric has come to denote a process in which the initial and final quantum-mechanical states of the system are identical. Thus, in a parametric process there are only transitions to virtual levels which only can be populated for a brief time determined by the uncertainty principle.

## 2.4 Nonlinear Materials and Phase matching

In this section we will take a closer look at the so called phase-matching condition or

$$\mathbf{k}_3 \equiv \mathbf{k}_1 + \mathbf{k}_2. \quad (2.11)$$

For the case of collinear phase matching (all k-vectors parallel) this can be rewritten in scalar form as

$$n(\omega_3)\hbar\omega_3 = n(\omega_1)\hbar\omega_1 + n(\omega_2)\hbar\omega_2. \quad (2.12)$$

This condition has to be fulfilled for efficient frequency conversion to take place. Unfortunately  $n(\omega)$  grows monotonically with  $\omega$  for normally dispersive materials, i.e. when  $\omega$  is far from a resonance in the material, and makes phase-matching impossible. Many crystals however, are anisotropic so that the refractive index experienced by a wave varies with the direction of polarisation [23]. These crystals are called birefringent. Birefringent crystals with one symmetry (optic) axis are called uniaxial crystals. In a uniaxial crystal waves with a polarisation direction normal to the optic axis and the propagation vector are called ordinary waves, and waves with a polarisation direction normal to the propagation vector and the ordinary polarisation direction are called extraordinary waves. The extraordinary waves will experience different refractive indices depending on the direction of propagation whereas the ordinary waves will have a constant index of refraction. Fig 2.3 shows the case of a negative uniaxial crystal, i.e.  $n_e < n_o$ . In a uniaxial crystal the extraordinary index of refraction  $n_e(\theta)$  depend on the angle  $\theta$  between the optic (z) axis and  $\mathbf{k}$  according to the relation [5]

allows phase matching, preferably over a wide range of frequencies. However, if the nonlinearity is too large, angle tuning of the crystal will be too sensitive to be practical. The material must also have a wide range of transmission so that the generated radiation can propagate through the material.

**Table 2.1** Properties of common nonlinear optical materials. The data in columns 4 and 5 are valid at typical pump wavelengths for each material, for BBO at 355 nm, and for KTP and LiNbO<sub>3</sub> at 1 μm. [4,6,15,40]

Crystal	Point Group	Transmission (μm)	Index of Refraction	Nonlinear Coeff. (10 <sup>-12</sup> m/V)
BBO (β-BaB <sub>2</sub> O <sub>4</sub> )	3m	0.20-2.2	n <sub>o</sub> = 1.6551 n <sub>e</sub> = 1.5426	d <sub>22</sub> = 2.22 d <sub>31</sub> = 0.16
KTP (KTiOPO <sub>4</sub> )	mm2	0.35-4.5	n <sub>x</sub> =1.7386 n <sub>y</sub> =1.7458 n <sub>z</sub> =1.8287	d <sub>31</sub> = 6.5 d <sub>32</sub> = 5.0 d <sub>15</sub> = 6.1 d <sub>24</sub> = 7.6 d <sub>33</sub> = 13.7
LiNbO <sub>3</sub>	3m	0.33-5.5	n <sub>o</sub> = 2.2340 n <sub>e</sub> = 2.1554	d <sub>22</sub> = 2.76 d <sub>31</sub> = -5.44

KTP has two optical axes, this type of material is called biaxial. The point group refers to what symmetry group a particular crystal belongs. The nonlinear coefficients are the nonzero components of the tensor  $d_{ijk} = \frac{1}{2} \chi_{ijk}^{(2)}$ . The effective nonlinear coefficient, in Eq. (2.10) can be calculated with knowledge of point group and nonlinear coefficients. For second harmonic generation in a 3m crystal, with Type I phase matching, the effective value of  $d_e$  is given by [4,6]

$$d_e = d_{31} \sin \theta - d_{22} \cos \theta \sin 3\phi, \quad (2.16)$$

where  $\theta$  and  $\phi$  describe the orientation of the polarisation in a spherical co-ordinate system with the z-axis parallel to the optic axis.

As can be seen in Table 2.1 the nonlinear coefficients are very small, of the order 10<sup>-12</sup> m/V. This should be compared to the first order susceptibility which is close to unity. The first order polarisation in Eq. (2.4) was,  $\tilde{P}^{(1)}(t) = \epsilon_0 \chi^{(1)} \tilde{E}(t)$ , and the second order polarisation was,  $\tilde{P}^{(2)}(t) = \epsilon_0 \chi^{(2)} \tilde{E}^2(t)$ . If the second order polarisation should not be completely negligible high optical intensities are required.

Figure 2.7 shows the tuning curve for a BBO OPO and Fig. 2.8 shows the bandwidth of the generated frequencies.

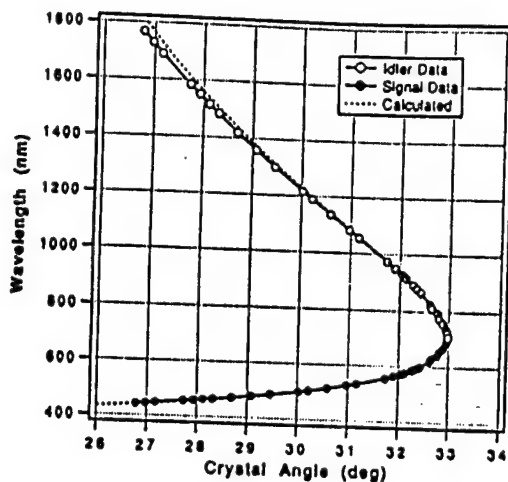


**Figure 2.7** Signal and idler wavelengths for an angle tuned Type I phase matched BBO ( $\beta\text{-BaB}_2\text{O}_4$ ) OPO for a pump wavelength of 355 nm. [27]

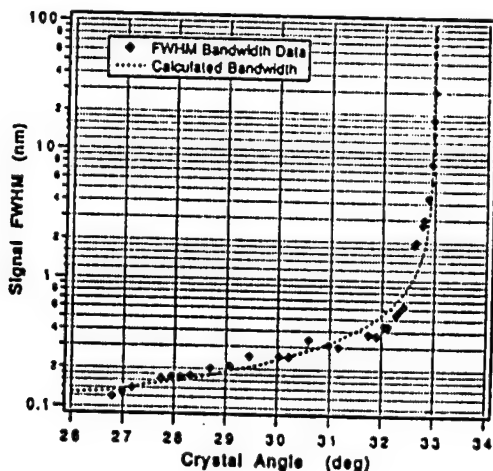


**Figure 2.8** FWHM spectral bandwidth for the signal and idler wavelengths in Fig. 2.7. The bandwidth increases dramatically close to the degeneracy angle at 33°, where the signal and idler wavelengths are identical. [27]

## 2.8 Injection Seeding

To spectrally narrow the output of an OPO, it is common to use injection seeding. This means that immediately prior to the arrival of the pump pulse, narrow-band radiation at the desired signal (or idler) wavelength is inserted into the cavity. This will make the OPO oscillate on the inserted frequency, provided it fulfils the phase matching condition.

output pulse may be slightly shorter than the pump pulse because of lower intensities at the beginning and end of the pump pulse, and hence much lower conversion.

The characteristics of the output from an OPO depend on several factors. It is necessary that the pump pulse have low divergence and a narrow bandwidth. In a broadband pump pulse for example, only a small fraction of the radiation will satisfy the phase matching condition. If the pump pulse is divergent, parts of the beam with different directions will satisfy different phase matching conditions and hence create a more broadband output. Both of these factors contribute to decreasing the efficiency of the interaction since they "smear" the pump intensity over a larger frequency interval. [58]

The nonlinear material itself will also contribute to the spectral broadening of the signal and idler, because the phase-matching condition can be satisfied by frequencies within an interval, it has a certain gain bandwidth. To lower the bandwidth, it is possible to insert dispersive elements into the cavity to increase losses for all but a narrow frequency-band, as is often done in lasers. These elements are typically etalons or gratings. However if the pump power is raised to increase the output power, frequencies that were suppressed by high losses in e.g. an etalon may once again reach threshold and broaden the linewidth of the output. This makes it very hard to obtain narrow-band high power output from an OPO and makes the design of OPOs much more difficult. In pulsed OPOs, there is a way around this, so called injection seeding, where the OPO is seeded with narrow-band radiation just prior to the arrival of the pump pulse.

## 2.6 Tuning Curves

It is possible to generate many different output frequencies with an OPO by changing the phase matching condition, which means a physical rotation of the crystal. For different crystal angles  $\theta$ , there will be different pairs of frequencies  $\omega_1, \omega_2$  that are phase matched. This is called angle tuning. For a negative uniaxial crystal ( $n_e < n_o$ ) the equation is [6]

$$n_e^e \omega_3 = n_i^o \omega_1 + n_s^o \omega_2 \quad (2.15)$$

If the frequency dependence of the refractive index is known or can be modelled it is possible to calculate so called tuning curves for different materials, i.e. curves which display

output frequencies as a function of crystal angle. Fig. 2.6 shows a tuning curve for LiNbO<sub>3</sub>, the linewidth of the generated light is also shown. For a derivation of the equations describing these curves see e.g. [42].

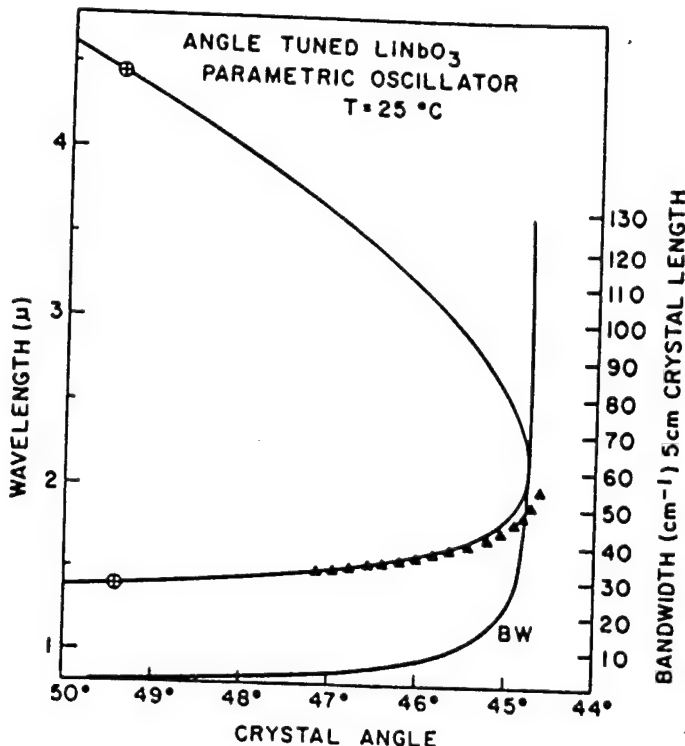


**Figure 2.6** Tuning curve and gain bandwidth for an angle-tuned LiNbO<sub>3</sub> parametric oscillator. [42]

One problem with the angle tuning method is that for extraordinary waves, the propagation vector  $\mathbf{k}$  and the energy flow, or Poynting vector  $\mathbf{S}=\mathbf{E}\times\mathbf{H}$ , are not parallel whenever  $\theta\neq 0^\circ, 90^\circ$ . This is an effect of the birefringence and is called "walk-off". Because of this, ordinary and extraordinary waves with parallel propagation vectors will diverge. This limits the spatial overlap of the waves, and thus decreases the efficiency of the process.

## 2.7 Properties of Nonlinear Crystals

In this section properties of some of the most common nonlinear crystals are presented. LiNbO<sub>3</sub> was the material used by Giordmaine and Miller in the first OPO [18]. BBO is a commonly used crystal in OPOs in the visible domain and also the material used in the Spectra-Physics OPO. For a crystal to be a good choice, it must be sufficiently nonlinear so that it

## CHAPTER 3

### MOPO DESCRIPTION

The OPO used in our experiments was a Spectra-Physics 730-10 MOPO pumped by a Spectra-Physics GCR-250 Nd:YAG laser. In this chapter the OPO and the pump source will be described and explained to give the reader some fundamentals in how the OPO-system works. The components will be reviewed in the order in which the beam reaches them, i.e. with the pump source first. Both the OPO and the Nd:YAG have electronic control boxes to aid the user. Figure 3.1 shows an outline of the whole system. The third harmonic from the infrared Nd:YAG laser is used to pump the OPO. The OPO output can then be frequency doubled to produce tuneable output in the UV region. In Fig. 3.2 the full tuning range of the OPO output is shown. A more technical presentation of this system with emphasis of the frequency doubler can be found in [30].

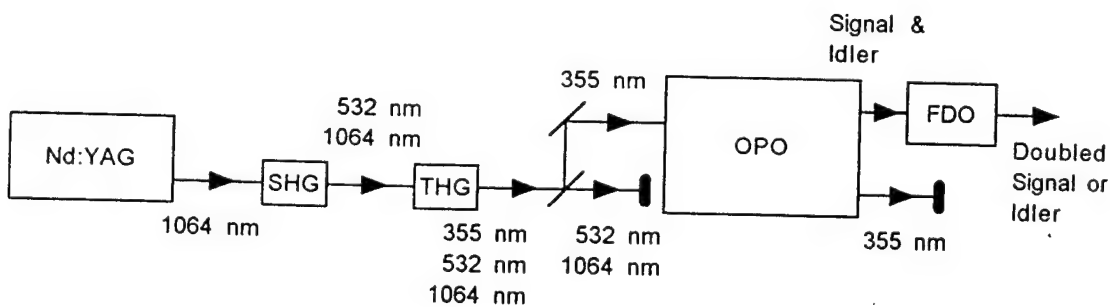
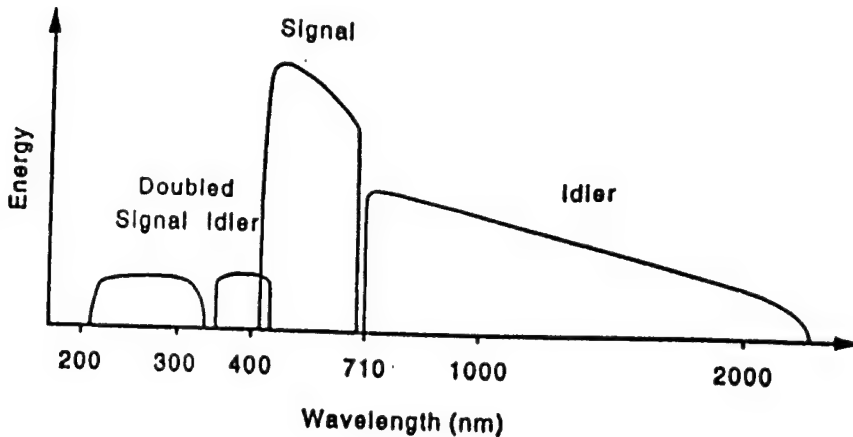


Figure 3.1 Schematic of Spectra-Physics 730-10 MOPO system with pump source and frequency doubler option (FDO). The Nd:YAG pulse is frequency doubled in the second harmonic generator (SHG) and the third harmonic is obtained by mixing the fundamental and the second harmonic in the third harmonic generator (THG). The undesired radiation at 532 nm and 1064 nm is removed by use of two dichroic mirrors after the THG. Inside the OPO the 355 nm pump-pulse generates signal and idler pulses within the tuning range. In the FDO (frequency doubler option) either the signal or the idler can be frequency doubled.



**Figure 3.2** MOPO output at different wavelengths. The tuning range is 440 nm to 690 nm for the signal and 735 to 1800 for the idler. The FDO extends the tuning range from 220 nm to 345 nm and 366 nm to 440 nm for the doubled signal and idler, respectively. As is expected no output is observed at the degeneracy wavelength 710 nm. [47]

### 3.1 GCR-250 Nd:YAG Pump Laser

The GCR-250 is used as a pump source to the OPO. It is a Q-switched single longitudinal mode Nd:YAG laser operating at 10 Hz. It produces transform limited output pulses with an almost flat-top transverse power distribution.

Figure 3.3 shows an outline of the laser. The cavity is an unstable resonator design which produces a well collimated output beam. The Nd:YAG rod is surrounded by two quarter-wave plates that create circularly polarised light inside the Nd:YAG rod, in order to avoid spatial hole burning effects. The Q-switch is made of a quarter-wave plate, a Pockels-cell [37] and a polariser. There is a total of three Nd:YAG rods in the laser, two oscillator rods and a single pass amplifier rod. All rods are pumped by flashlamps.

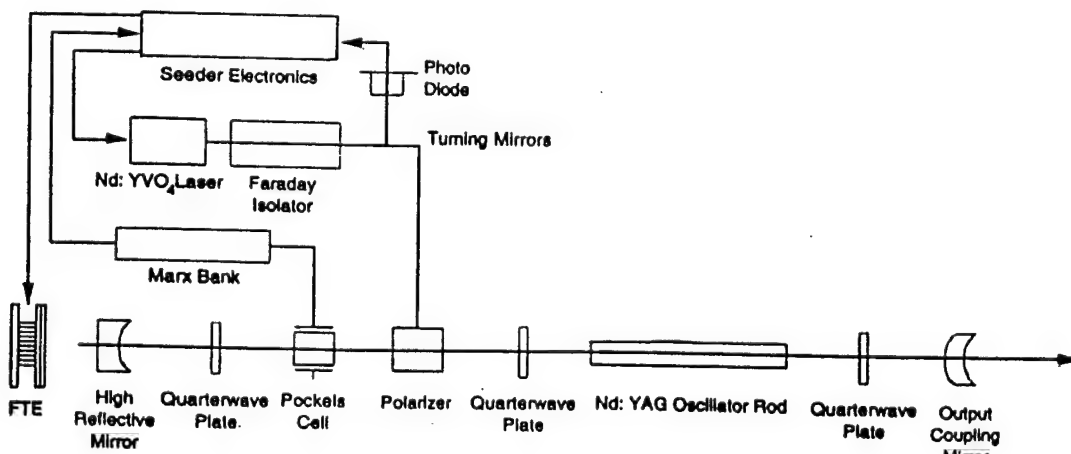


**Figure 3.3** Schematic of generic Spectra-Physics injection seeded GCR Nd:YAG lasers. The GCR 250 contains two Nd:YAG oscillator rods, instead of one as in the figure, followed by one single pass amplifier rod. [48]

In an unseeded OPO the radiation grows from noise photons that have been generated by parametric scattering. The growth of the fastest growing cavity modes, i.e. the modes under the gain profile of the crystal which have the lowest loss in the cavity, will initially be exponential. If even just minute amounts of the right frequency is inserted into the cavity this will represent a head start of several orders of magnitude with respect to the noise photons. Fix *et al.* [17] has reported at least partial seeding from stray light scattered in the lab. Even if the seed frequency does not match the fastest growing cavity modes exactly, but is close, it will still grow exponentially and will reach threshold faster than those frequencies generated by noise. The modes that first reach threshold will start to deplete the pump pulse and thus slow the growth of other modes. If the pump pulse is sufficiently long, however, the lowest loss modes will eventually be the ones oscillating in the cavity.

Injection seeding does not only allow narrow-linewidth output but also increases output energy per pulse in that it reduces the build-up time and increases the depletion in the beginning of the pump pulse.

To illustrate the difference between seeded and unseeded or free-running mode of operation, Fig. 2.9 shows spectral profiles of a BBO OPO as its peak gain frequency is shifted away from the seed frequency.

A complete theoretical presentation of injection seeding is presented in [7].

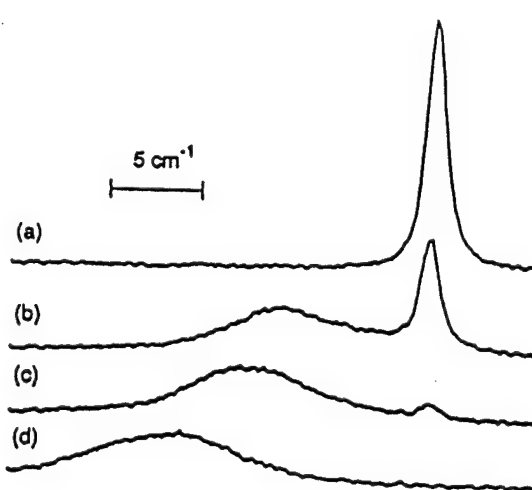


**Figure 2.9** Injection seeding of a BBO OPO pumped at 355 nm. The OPO goes from seeded (a) to free-running (d) mode of operation as the phase-matching angle of the crystal is changed. [17]

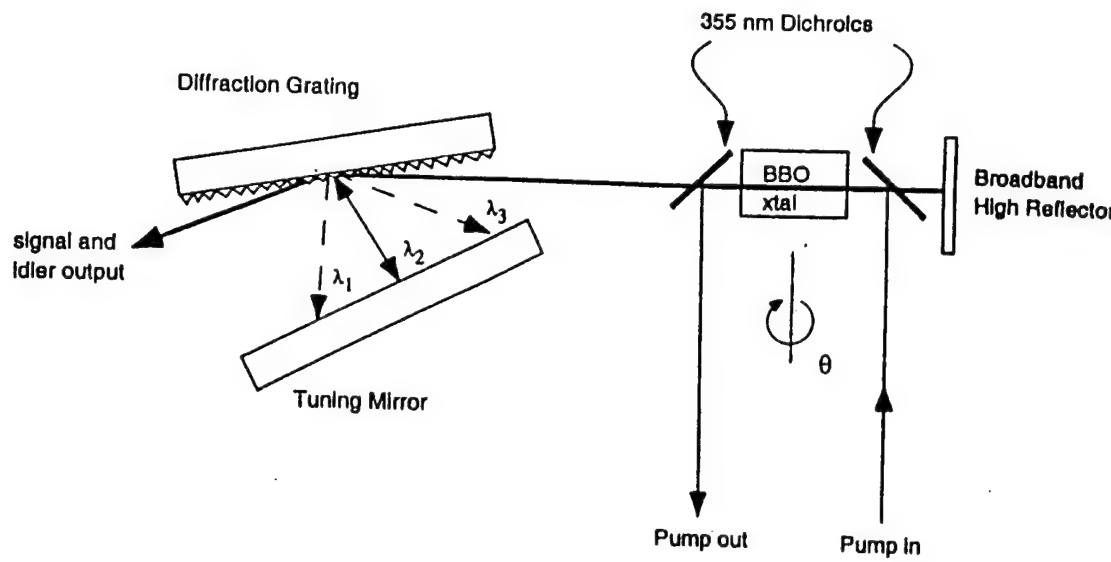


**Figure 3.8** Schematic of the Master Oscillator cavity. The Master Oscillator is a singly resonant OPO which uses a grating as an intracavity dispersive element to reduce the linewidth of the output pulse. This design is called a Littman cavity. The Master Oscillator is tuned by changing the crystal angle (i.e. the phase matching condition) and by moving the tuning mirror to select what signal wavelength is resonant in the cavity. The signal linewidth is about  $0.2 \text{ cm}^{-1}$  corresponding to 4-6 longitudinal cavity modes. [47]

The 355 nm pump beam is brought into and out of the cavity by two UV reflecting dichroic mirrors that sit on either side of the BBO crystal. By changing the angle of the BBO crystal, the refractive index of the vertically polarised pump beam will change and so will the phase matching condition. The signal and idler beams are horizontally polarised. The BBO crystal is cut for Type I phase matching at a  $28^\circ$  angle to the optic axis. Since BBO is a negative uniaxial crystal, the pump beam is the extraordinary wave and the signal and idler are both ordinary waves. The wavelength tuning of the master oscillator is somewhat complex in that the tuning mirror and the BBO crystal angle must both be moved. To aid the user this is done electronically by a control unit.

Because of the high losses in the cavity, high intensities are needed to pump the master oscillator. The pump beam passes through a Galilean telescope to increase the intensity. About 30 % of the 500 mJ pump pulse is sent into the master oscillator. The output energy is about 8-12 mJ. The linewidth is less than  $0.2 \text{ cm}^{-1}$  which corresponds to about 4-6 longitudinal modes. Thus the master oscillator is really continuously tuneable [22].

The output from the master oscillator is sent via two mirrors, S-TM1 and S-TM2, through a slit and through the power oscillator broad-band high reflector (PO-BBHR) into the

power oscillator cavity. There may be variations in linewidth across the seed beam and the slit acts as a spatial filter to further narrow the linewidth of the seed beam.

### 3.2.2 Power Oscillator

The power oscillator cavity is a confocal unstable resonator, shown in Fig. 3.9, with a high reflectance concave rear mirror and a lower reflectance convex output coupler. The advantage with this design, as opposed to e.g. a flat-flat resonator, is a low divergence output. As in the master oscillator the pump beam is brought into and out of the cavity via two UV reflecting dichroic mirrors. The BBO crystal in the power oscillator is identical to the one in the master oscillator.

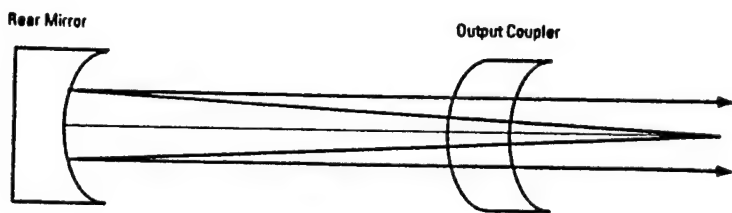


**Figure 3.9** Schematic of an unstable resonator cavity, which gives a Gaussian like spatial mode with low beam divergence. [47]

When the three beams, i.e. pump signal and idler, travel through the BBO crystal at a skew angle they are displaced vertically. To compensate for this, a fused silica crystal compensator is rotated to the opposite angle of the BBO crystal. Figure 3.10 shows the power oscillator cavity.

### 3.2.3 Optical Beam Path within the MOPO

Here follows a complete description of the beam paths of the MOPO, shown in Fig. 3.6. When the UV pump pulse enters the MOPO unit it first reaches a beam splitter (UVBS) that splits the pulse into two parts, with approximately 30 % to the master oscillator. In the master oscillator branch the beam bounces off mirrors MO-TM1 and MO-TM2 and goes through a Galilean telescope to mirror MO-TM3. The UV reflecting dichroic mirrors MO-TM4 and MO-TM5 take the beam into and out of the master oscillator. MO-TP1 sends the remainder of the pump beam to an external beam dump. The master oscillator signal is sent via mirror S-TM1 to

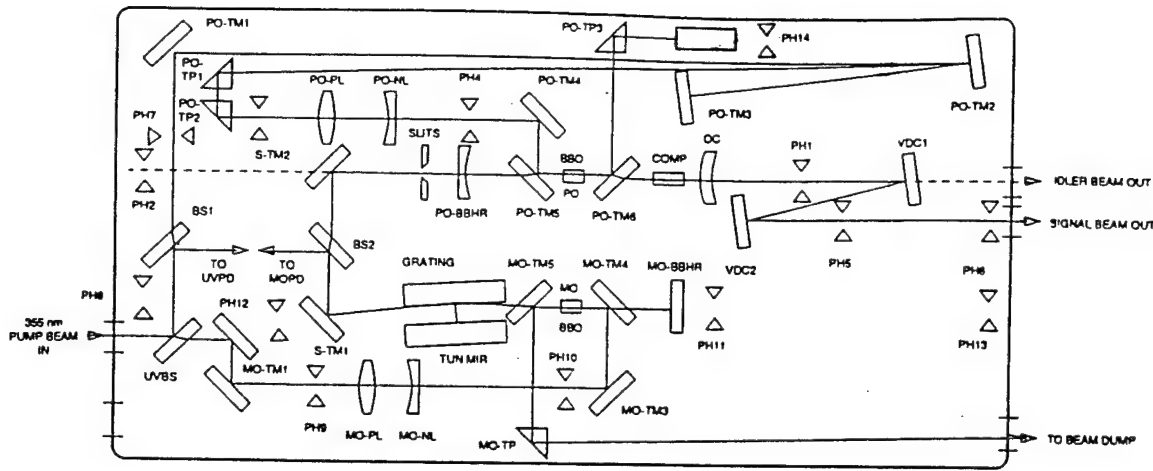


**Figure 3.6** Schematic of Spectra Physics 730-10 MOPO. The incoming 355 nm pump beam is split into two parts of which one pumps the Master Oscillator (lower half of figure) and one pumps the Power Oscillator (top half). The signal and idler are separated by a pair of dichroic mirrors. [47]

Figure 3.7 is a photo of the 730-10 MOPO. The photo does not cover the right part of the MOPO with mirrors PO-TM2 and VDC-1. The bright square in the right central part of the photo sits between the master and power oscillators. The two arms protruding on either side of it is where the master and power oscillator crystals are mounted.

All of the components inside the MOPO box are mounted on a single plate to minimise thermal effects. For the same reason the MOPO and the Nd:YAG laser must be mounted on the same optical table. The system is purged with N<sub>2</sub> gas to keep humidity at a minimum.

### 3.2.1 Master Oscillator

The master oscillator, shown in Fig. 3.8, is a singly resonant OPO that produces narrow-linewidth output used to seed the power oscillator. The cavity contains a dispersive element in the form of a diffraction grating that introduces high losses for all wavelengths but the desired one. The cavity contains a broad-band high reflector (MO-BBHR) at one end and a diffraction grating and a tuning mirror at the other. The zeroth order (specular) reflection of the grating is always reflected at the same angle and constitutes the output. In the first order reflection, different wavelengths will be reflected at different angles, and the position of the tuning mirror will decide which wavelength that is sent back into the cavity. As shown in Fig. 3.8, by changing the position of the tuning mirror, different wavelengths will be resonant in the cavity [24].

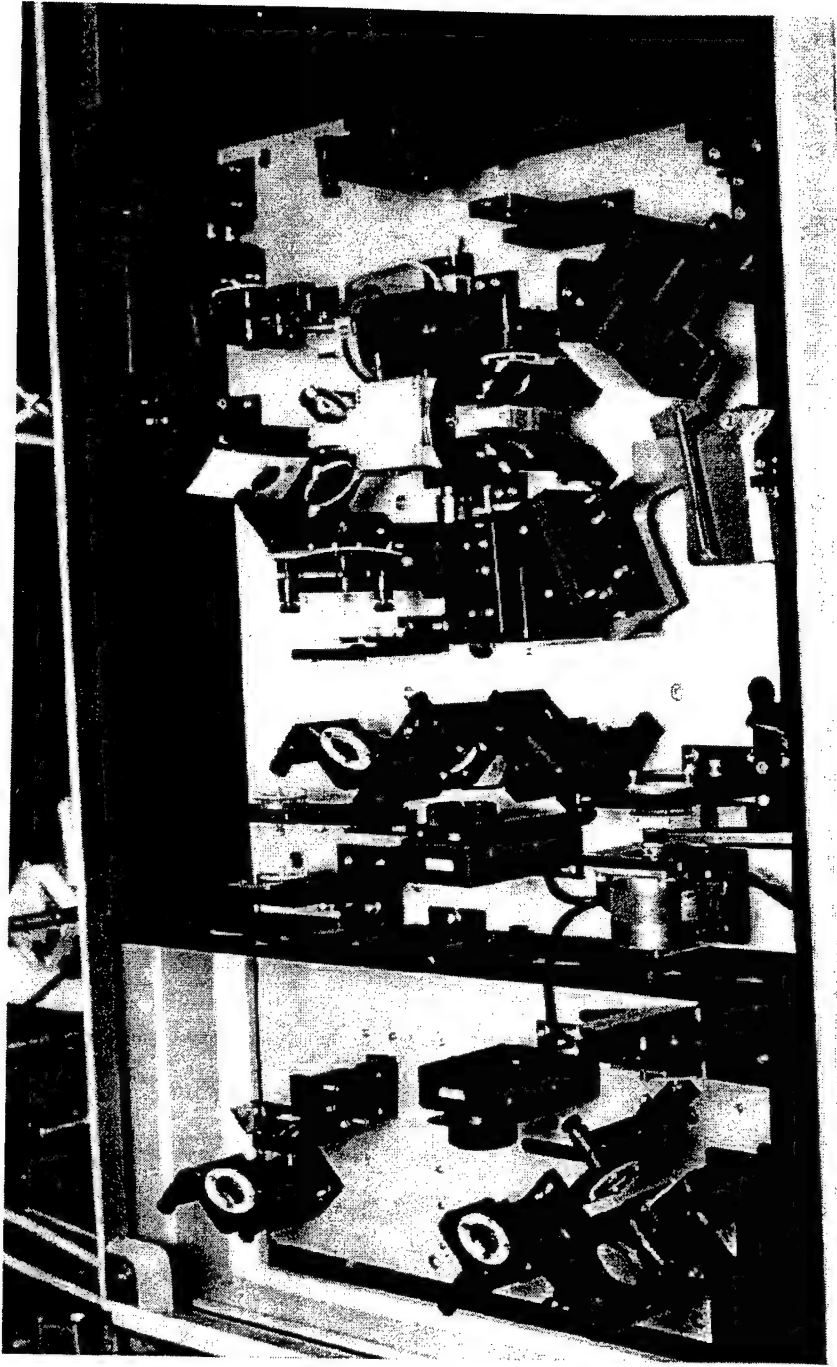
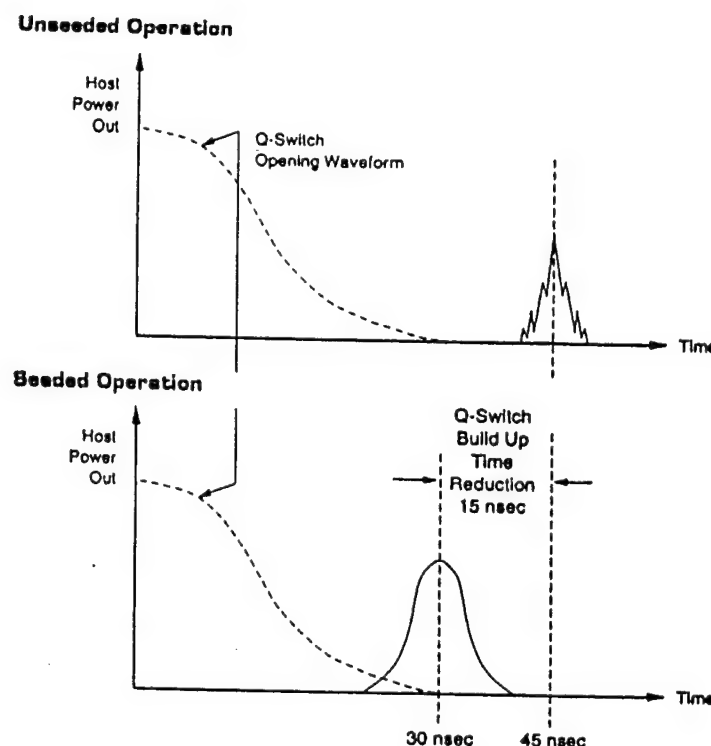


Figure 3.6 Photograph of the Spectra-Physics 730-10 MOPO.

To obtain a narrow-band output, the laser is seeded by a diode-pumped single longitudinal mode CW Nd:YVO<sub>4</sub> laser, which can be tuned to exactly match the centre of the Nd:YAG gain profile at 1064 nm. If the Nd:YAG laser is not seeded there will be several cavity modes under the laser gain profile that will oscillate simultaneously, resulting in a poor temporal profile and a more broad-band output, as shown in Fig. 3.4. The cavity length is continuously adjusted by a piezo-electric device to match the desired cavity mode.



**Figure 3.4** Timing diagram of Nd:YAG laser output pulse showing seeded and unseeded operation. The unseeded pulse is initiated by quantum noise which increases the build up time and also permits multiple longitudinal modes oscillating simultaneously which leads to a poor temporal profile. [48]

To produce the shorter wavelengths desired for OPO pumping, the 1064 nm IR radiation is first doubled frequency to 532 nm (green) in the so called second harmonic generator (SHG). The 355 nm third harmonic is produced by means of sum-frequency mixing of the fundamental and second harmonic in the third harmonic generator (THG). Two UV reflecting dichroic mirrors are used to separate the 355 nm beam from the 1064 nm and 532 nm beams which are sent into a beam dump. The 1064 nm and 532 nm radiation is sent into a beam dump. Figure 3.5 shows a photo of a GCR-290, which contains two single pass amplifiers instead of one as the GCR-250 does.

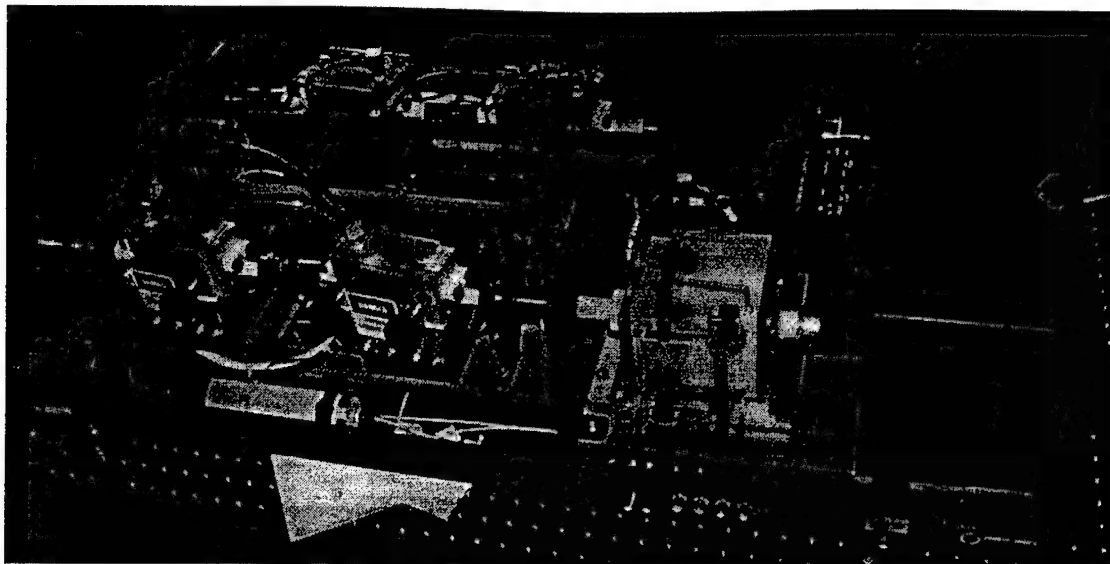


**Figure 3.5** Photograph of GCR-290 Nd:YAG Laser. The cavity contains two Nd:YAG oscillator rods (top of photo) and two single pass amplifier rods (bottom left). The steel housing at the bottom right contains the two KD\*P crystals used for second and third harmonic generation.

The energy per pulse for the 1064 nm fundamental is roughly 1.5 J and the 355 nm third harmonic is around 0.5 J. The IR pulselength is about 10 ns and the UV pulse length is about 7 ns.

### 3.2 Spectra-Physics 730-10 MOPO

The MOPO, displayed in Fig. 3.6, contains two singly resonant OPOs, the master oscillator, which is a low-power narrow-linewidth OPO, and the power oscillator, which is a high-power broadband OPO. The two oscillators are pumped by the same pulse, which is split into two parts by a beam splitter (UVBS), as it reaches the MOPO box. One part goes into the master oscillator (lower half of Fig. 3.6) and the other part, about 70 %, goes into a delay line before it reaches the power oscillator (upper half of Fig. 3.6). The master oscillator is used to seed the power oscillator to obtain narrow linewidth output and the delay line is necessary to obtain a proper timing of the two pulses. Both master and power oscillators are resonant on the signal frequency. After the power oscillator, the signal and idler are separated by two dichroic mirrors, VDC1 and VDC2, or sent into the frequency doubler, which is discussed in Chapter 3.3.

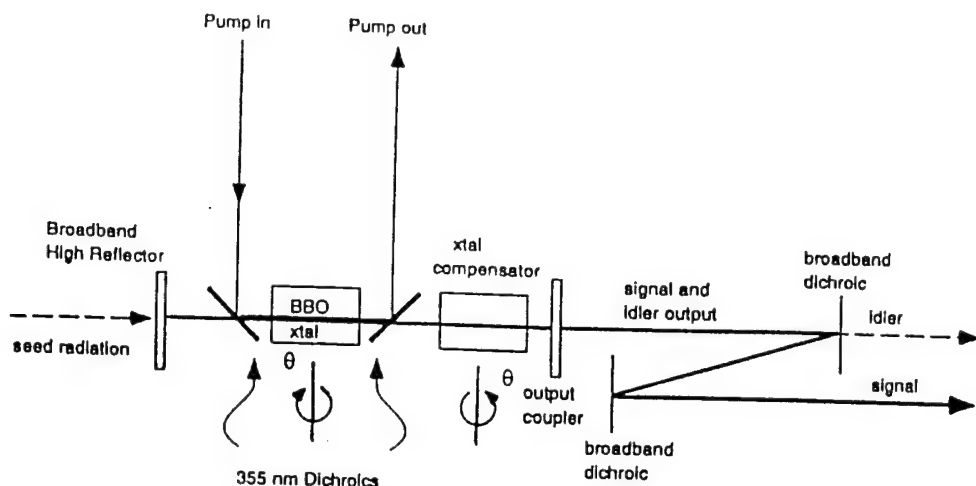


**Figure 3.10** Schematic of the Power Oscillator cavity which is an unstable resonator. It contains a crystal compensator to compensate for beam displacement due to the angular tuning of the BBO crystal. [47]

a beamsplitter, BS2, that picks off a fraction of the beam to a photodiode detector that monitors the master oscillator output. The rest goes through BS2 to mirror S-TM2, which sends the beam through a narrow slit and to PO-BBHR. Approximately 1 % of the seed beam goes through the PO-BBHR.

The pump beam in the power oscillator branch is directed by the UVBS beamsplitter to the BS1 beamsplitter, which picks off a fraction of the pump beam to monitor the pump power. The remaining part goes into a delay line to ensure that the seed pulse is already present in the power oscillator when the pump pulse arrives. The optics are PO-TM1, PO-TM2, PO-TM3 and the two prisms PO-TP1 and PO-TP2. A Galilean telescope ensures a well collimated beam with the right intensity. The dichroic mirrors PO-TM4, PO-TM5 and PO-TM6 takes the beam into and out of the cavity. PO-TP3 sends the pump beam into a beam dump.

If the frequency doubler option (FDO, see chapter 3.3) is used, a prism is inserted just after PH1 to direct both signal and idler into the doubler. Otherwise the signal and idler are separated by the broad-band dichroic mirrors VDC1 and VDC2.

### 3.3 Frequency Doubling of OPO

Frequency doubling of OPOs is considered harder than frequency doubling of lasers because OPOs normally have divergencies and linewidths inferior to many lasers. The angular acceptance of BBO for frequency doubling at 500 nm is less than 0.5 mrad, which is difficult to accomplish in an OPO.

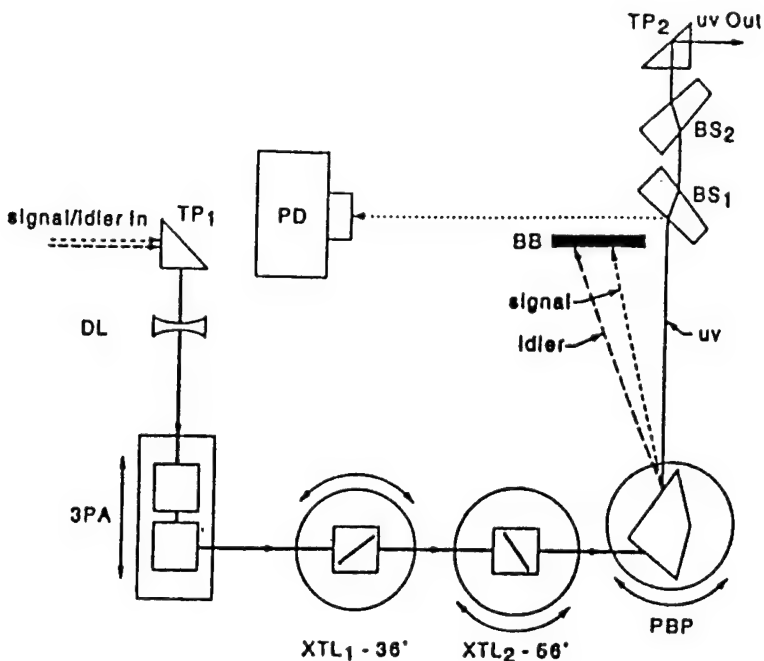


**Figure 3.11** The frequency doubler contains two BBO crystals with different cuts with respect to their optic axis in order to cover the entire tuning range. Also, in this design the crystals cancel their respective beam displacement. The Pellin-Broca prism is used to separate the different wavelengths, i.e. signal, idler and doubled. [45]

Figure 3.11 shows the frequency doubler option, FDO. The signal and idler beams are directed through two prisms that rotate the polarisation 90°. Two BBO crystals are used to cover the entire tuning range. They are cut at different angles with respect to their optic axes. Frequency doubling only takes place in one crystal at a time. The crystals are mounted on counter rotating stages so that the beam displacement of one crystal will be cancelled by the other. A Pellin-Broca prism is used to separate the three beams, signal, idler and doubled. The doubled output passes through two wedged optics before it is sent out. A pyro-electric detector monitors the output.

Figure 3.12 is a photograph of the FDO and shows how it is mounted inside the MOPO box. To the left in the photo the master and power oscillator can be seen.

The theory behind frequency doubling is similar to the OPO theory presented in Chapter 2. It is somewhat simpler because only two fields and, not three, interact. Instead of one photon being split into two, two photons with the same energy is converted into one photon with twice the energy. Figure 3.13 shows a tuning curve for frequency doubling in BBO.

during the alignment procedure. If the system is performing poorly the user can write new tables.

The electronics also allows a closed loop operation where the crystal angle is continuously peaked, by monitoring the master oscillator output.

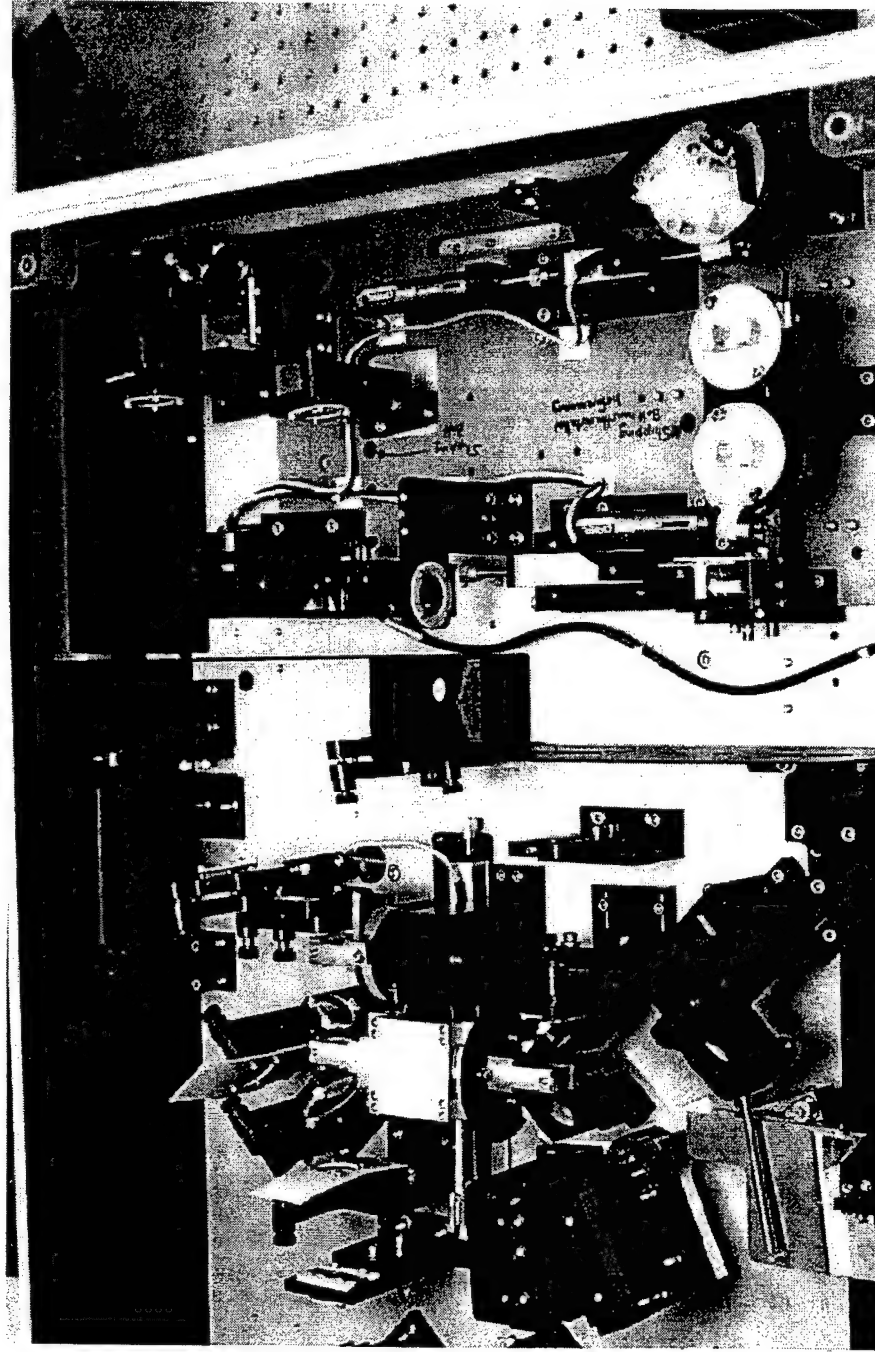
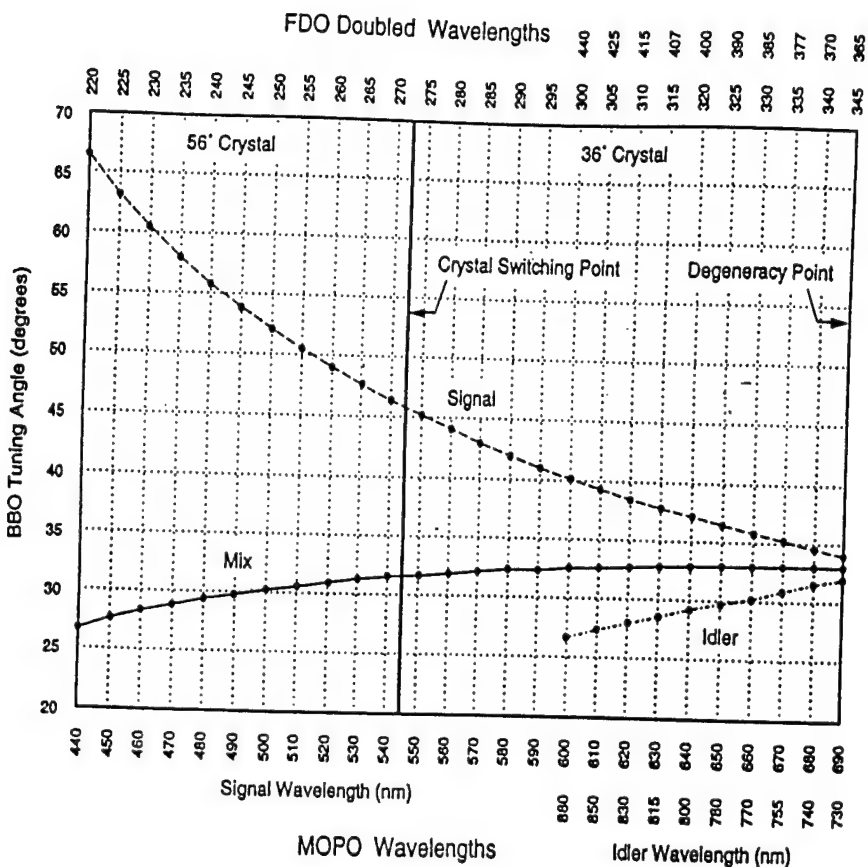


Figure 3.11 Photograph of the Frequency Doubler Option (FDO).



**Figure 3.13** Angle tuning curve for frequency doubling in BBO. [45]

### 3.4 Electronic Operation and Look-up Tables

When a certain output wavelength is desired several components of the system has to be adjusted. The tuning mirror in the master oscillator has to be set at a certain angle to make the desired signal wavelength resonant in the cavity. The master oscillator BBO crystal has to be rotated to achieve phase matching at the desired wavelength and the power oscillator BBO crystal also has to be set at the same angle as the master oscillator crystal. If the frequency doubler is used, the two BBO crystals in the FDO are rotated to achieve phase matching for frequency doubling in one of them and the Pellin-Broca prism also has to be rotated.

To aid the user, all of this is done electronically in the control unit. At all times the output wavelengths are displayed on the control unit. The control unit uses tables with set-points for the different devices. Each device, i.e. crystal, mirror etc., has its own table. The master and power oscillator crystals only have one table and their relative position are set

transmission of about 0.11 at 500 nm. The power meter used was a Scientech 361 power meter with a Scientech 3600 laser power meter head. Figure 4.3 shows how the attenuator was used. The measurements have a low degree of accuracy ( $\pm 20\%$ ) owing to uncertainties in the calibration of the attenuator and in the calibration of the power meter. We wanted to know how much the output power varied not necessarily the absolute value. The results are presented in Fig. 4.4 for the signal, Fig. 4.5 for the doubled signal, and Fig. 4.6 for the idler. These are rather typical in the size of the variations. The exact shape however, varied on a day to day basis. The attenuator was only used during measurements of the signal power.

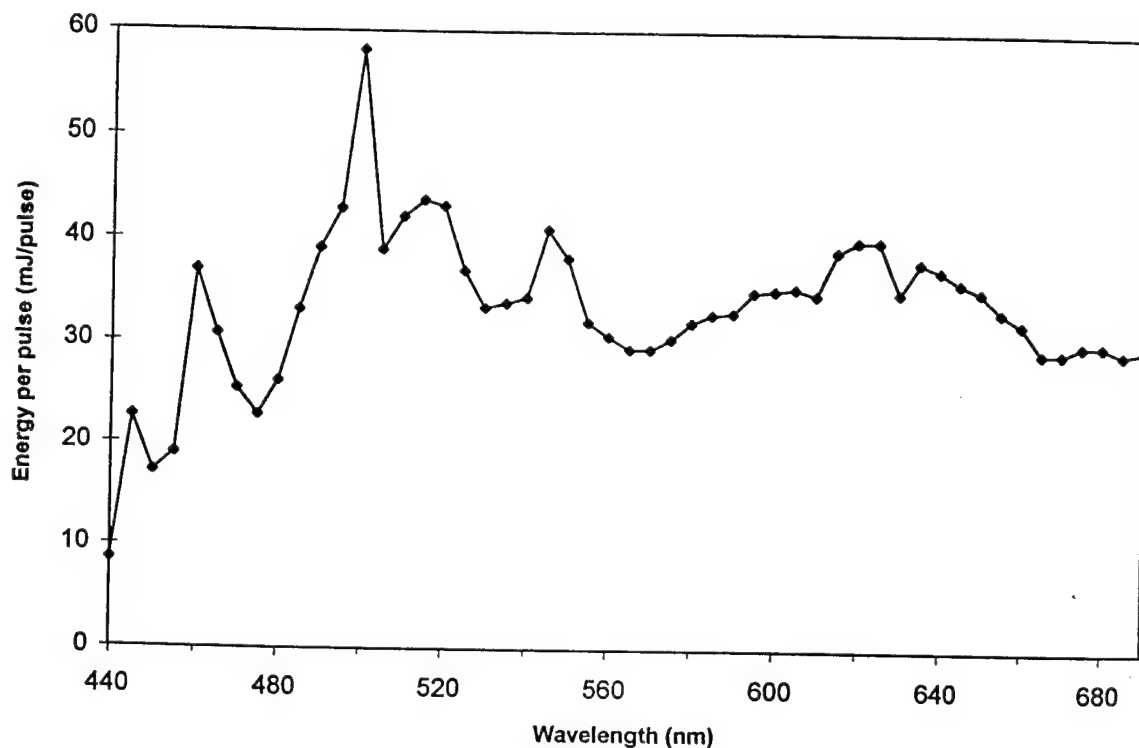


Figure 4.4 Measured output energy of the OPO signal as a function of wavelength

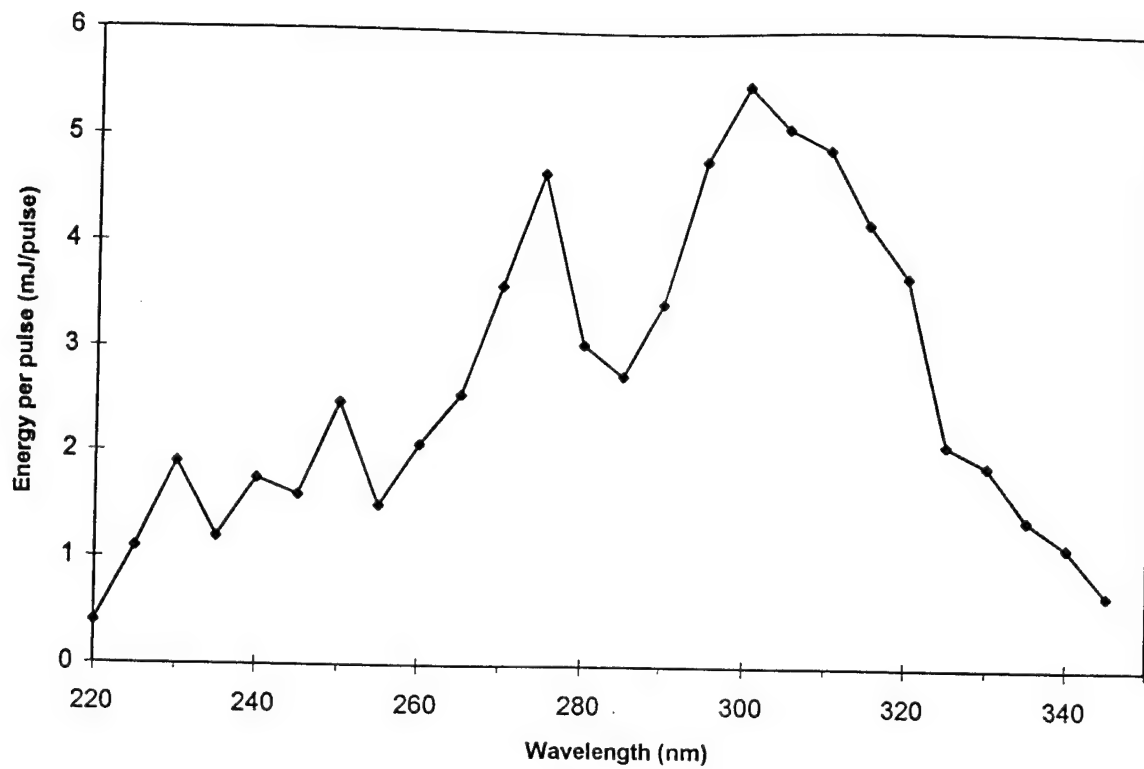


Figure 4.5 Measured output energy of the frequency doubled OPO as a function of wavelength.

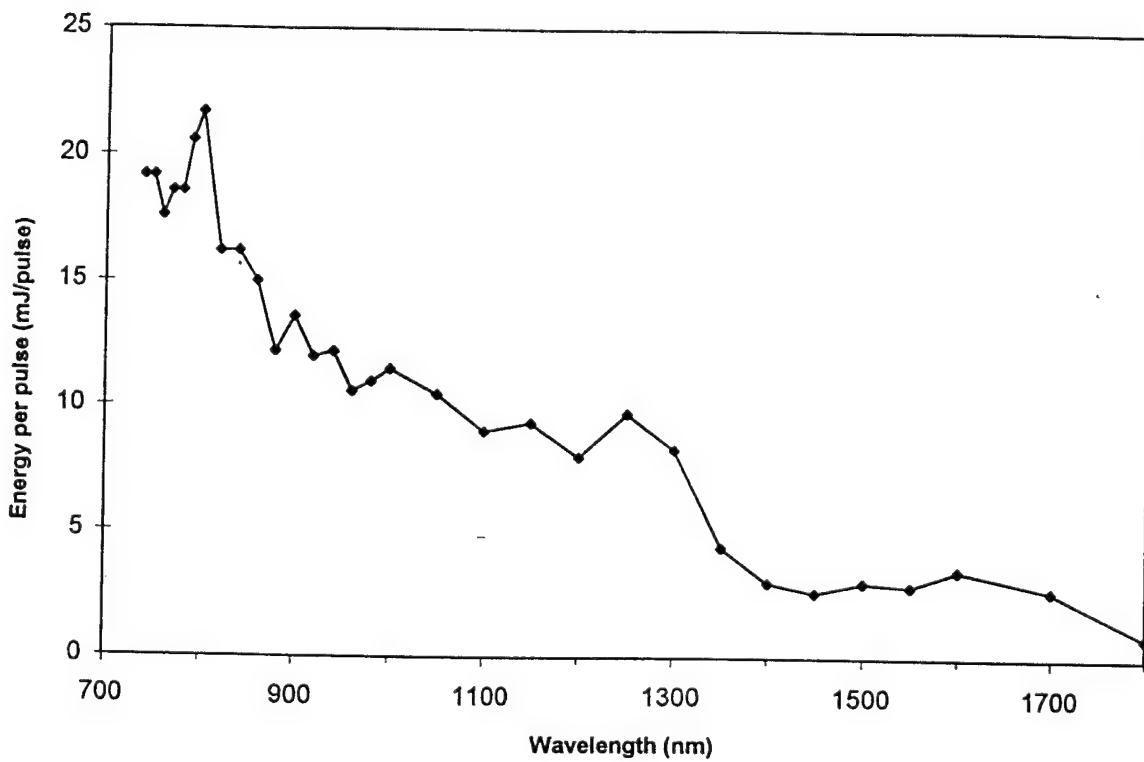


Figure 4.6 Measured output energy of the OPO idler as a function of wavelength.

# CHAPTER 4

## OPTICAL DIAGNOSTICS OF OPO SYSTEM

Before using the OPO system as a laser light source in the fluorescence experiments, several diagnostic measurements of the OPO output were performed. The purpose was to make sure the system performed according to the specifications and to gain some experience in using it. The first section of this chapter describes the measurements that were made. In the second section there is a discussion of some of the problems encountered and general experience.

### 4.1 OPO Charachterisation Measurements

The linewidth of the OPO was measured mainly to make sure the alignment of the system was good. The narrow linewidth of the OPO was necessary for good conversion efficiency in the FDO but not for the fluorescence experiments themselves. The linewidth of both the master and the power oscillator was measured at 500 nm using a  $1 \text{ cm}^{-1}$  FSR Fabry-Perot interferometer, as shown in Fig. 4.1. The Fabry-Perot fringes were observed on a target screen and later also focused down onto a Panasonic CCD chip (Model WL-BL 200 CCD camera) and displayed on a video monitor. The thickness of the fringes was estimated to less than one fifth of the fringe distance indicating a FWHM less than  $0.2 \text{ cm}^{-1}$ , which is the specified linewidth.

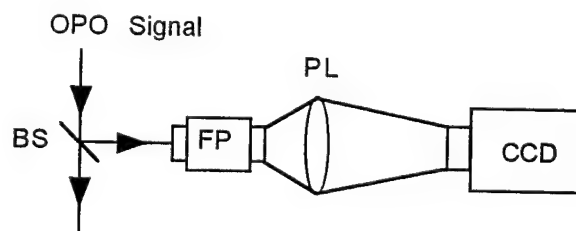


**Figure 4.1** To measure the linewidth a fraction of the OPO signal beam was picked off with a beamsplitter (BS) and sent into a  $1 \text{ cm}^{-1}$  FSR Fabry-Perot (FP). The Fabry-Perot fringes were then focused down onto a CCD chip with positive lens (PL).

The OPO system is wavelength calibrated by the manufacturer and the output wavelengths are displayed on the control unit during operation. The wavelength calibration of the OPO-system was checked against several line sources. The OPO signal and the line source were coupled into an optic fiber attached to an Ocean Optic, Inc. fiber optic spectrometer (Model SD 1000). The set-up is shown in Fig. 4.2. The following lines were used in the experiment: 435.8 (Hg), 543.5 (GreNe), 546.1 and 579.4 (Hg) and 632.8 (HeNe) [21]. The estimated deviation was less than the resolution of the spectrometer of about 0.4 nm. This was sufficient for the floorescence experiments.

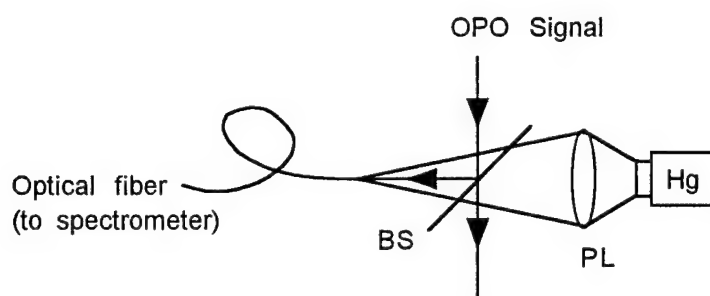


**Figure 4.2** The OPO signal and a line source were simultaneously coupled into a spectrometer to control the wavelength calibration.

The output power was measured for the signal, idler and doubled signal over the tuning range. Because of the relatively high peak power of the OPO signal ( $\sim 10^7$  W) an attenuator was used in front of the power meter to avoid damage. The attenuator was constructed by stacking 15 microscope slides at a  $30^\circ$  angle. The attenuator was calibrated and had a

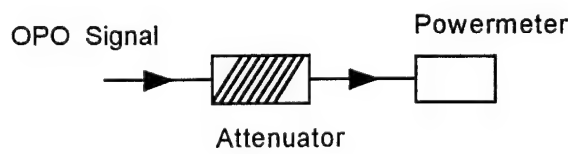


**Figure 4.3** Measurement of the OPO signal power.

Using the same experimental set-up as for the pulse lengths, the pulse-to-pulse stability for the OPO was measured by comparing the peak values of successive oscilloscope traces. Measurements were performed at 250 nm, 300 nm, 500 nm, and 600 nm and are displayed in Fig. 4.10. The specified pulse stability of the signal is  $\pm 8\%$  and for the frequency doubler  $\pm 15\%$ . The signal values are close to the specifications, but as can be seen the frequency doubled output is not.

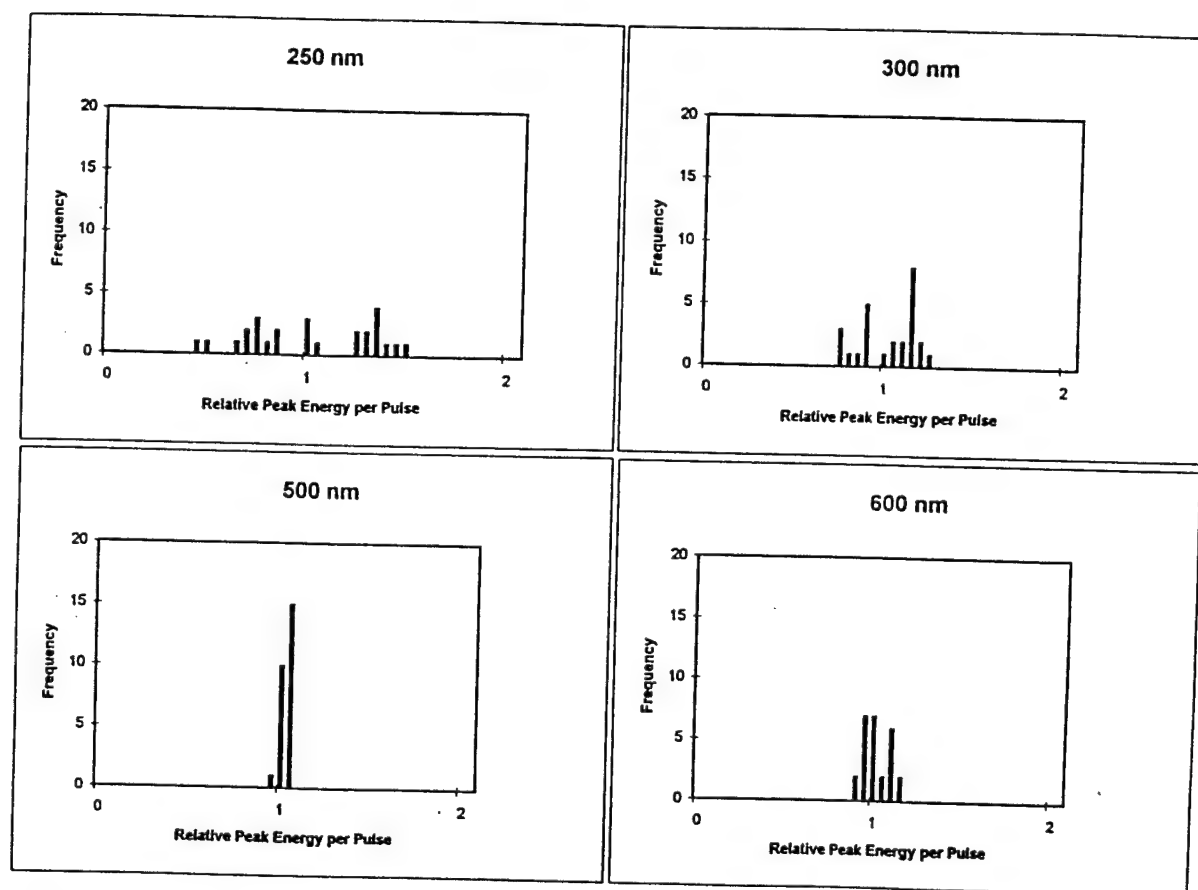


**Figure 4.10** Measured histogram of the OPO pulses showing pulse to pulse stability at different wavelengths.

To study the spatial distribution of the output, a beamsplitter picked off a fraction of the beam which was expanded and studied on a screen. Figure 4.11 and 4.12 shows two such spatial profiles at 550 nm and 275 nm recorded with a Hitachi Color Camera (model GP 5U). The photos have been filtered using computer software. The filter process has increased the contrast and the spatial variations are thus exaggerated in the figures. In Fig. 4.10 especially, the spatial mode is rather poor.

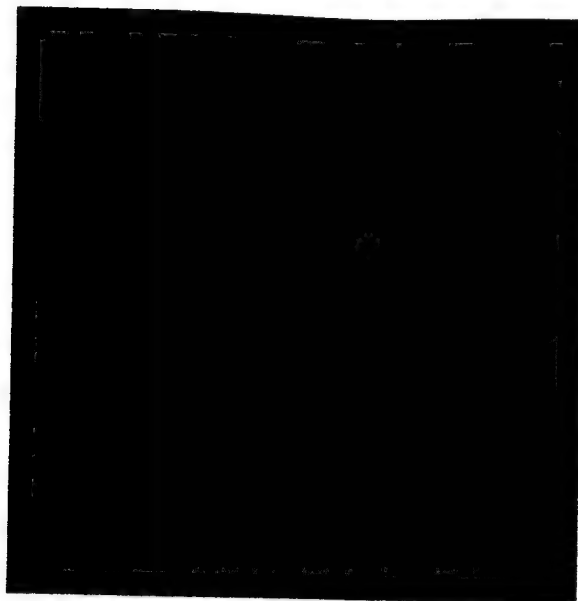


**Figure 4.9** Measured spatial profile of the OPO signal beam at 550 nm. The output signal beam was expanded and recorded with a videocamera.

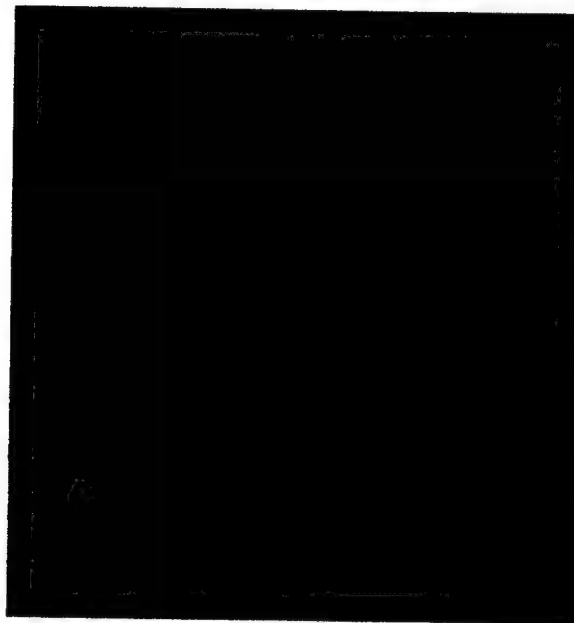


**Figure 4.10** Measured spatial profile of the doubled OPO signal beam at 275 nm, measured using a video camera. The videocamera image was produced by fluorescence of the UV beam in a white paper target .

Pulse-lengths and pulse-shapes from the Nd:YAG and the OPO were studied with a Si-detector, (Model Thorlabs, Inc. Det2-Si), and Tektronix Programmable oscilloscope (Model 11302). Single pulses were captured from the oscilloscope screen with a Tektronix CCD camera (Model C1001) interfaced with a PC computer using special software. The traces were stored and later analysed in the computer. Figure 4.7 shows an oscilloscope trace of the 355 nm UV pump pulse. The Si-detector was situated about 0.4 m from the pump beam at a 90° angle capturing scattered light. Figure 4.8 shows an oscilloscope trace of the OPO signal at 500 nm. The detector captured light scattered off of a black sandpaper. Black sandpaper was used to avoid any fluorescence in the target.

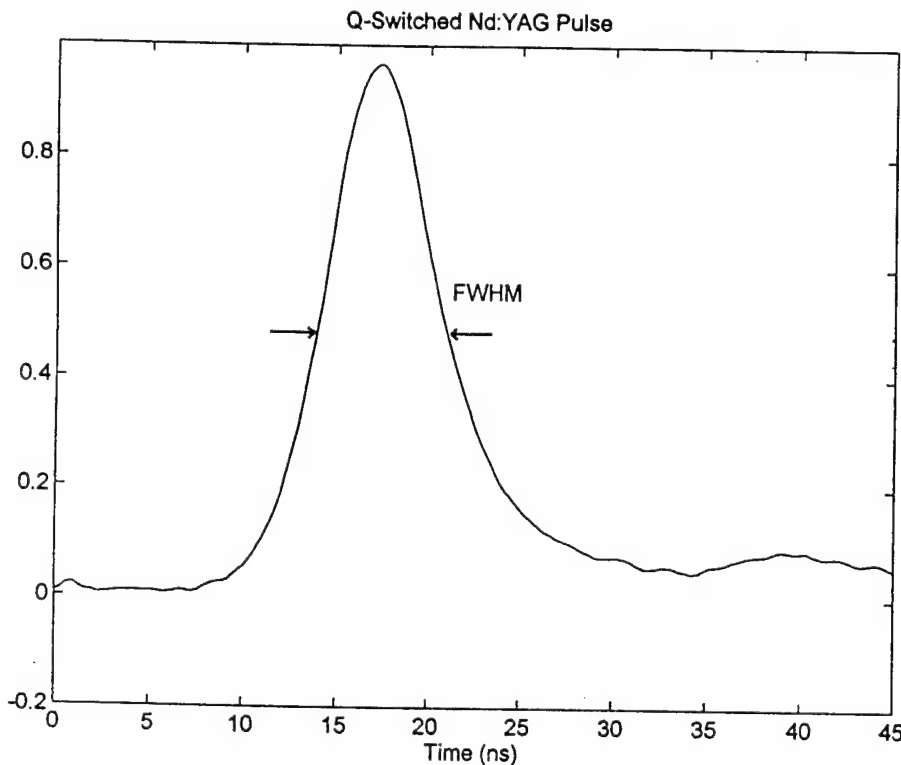
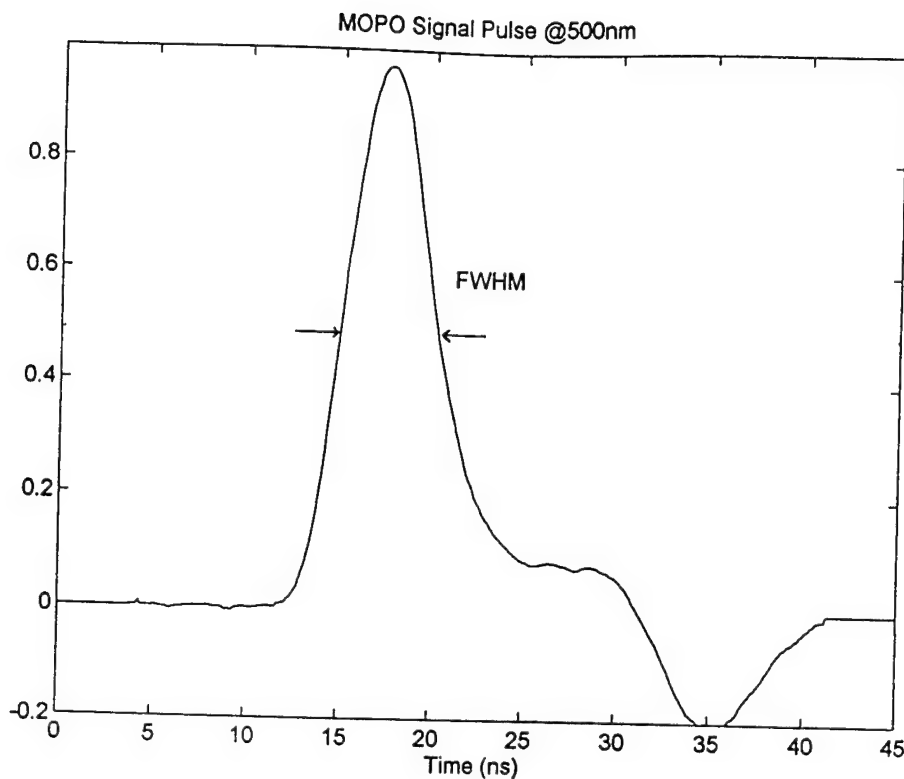
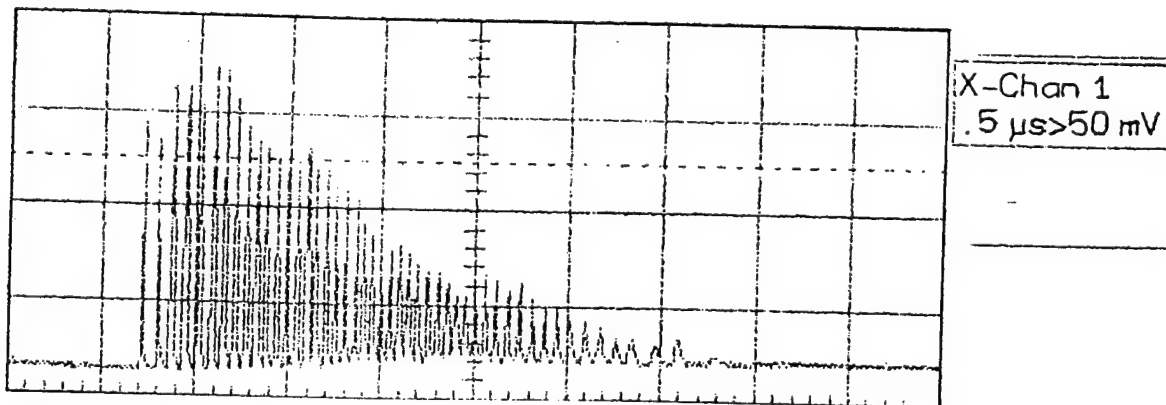


Figure 4.7 Measured Q-switched Nd:YAG laser pulse. FWHM is 7.3 ns.



**Figure 4.8** Measured OPO pulse at 500 nm. FWHM is 5.4 ns. The dip after the pulse is due to ringing in the cables.

Figure 4.9 shows an oscilloscope trace of spiking in Nd:YAG laser. The Nd:YAG laser is not Q-switched in this case but the Q-switch is continuously open. The oscilloscope used was a LeCroy 9400 Dual 125 MHz Digital Oscilloscope.



**Figure 4.9** Oscilloscope-trace of non Q-switched normal mode Nd:YAG pulse, showing relaxation oscillations.

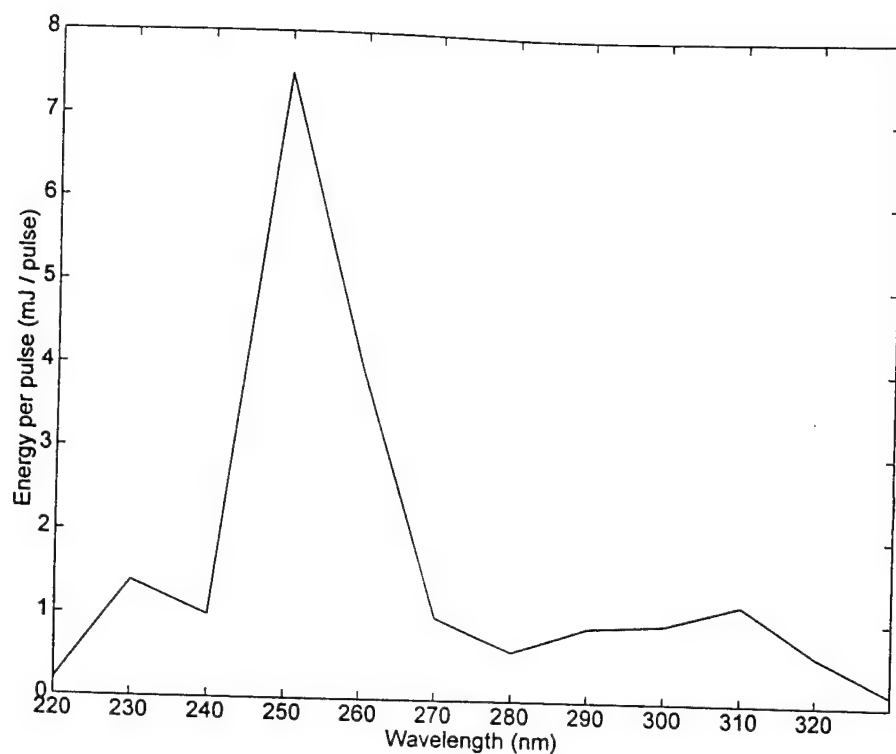


**Figure 4.15** Measured output energy of the frequency doubled OPO as a function of wavelength for the case where the Nd:YAG laser output power was down and pumping the OPO (Master Oscillator) barely above threshold.

The spatial distribution of the UV pump beam was studied using exposed polaroid film.

Figure 4.11 shows a burn pattern of the pump beam.

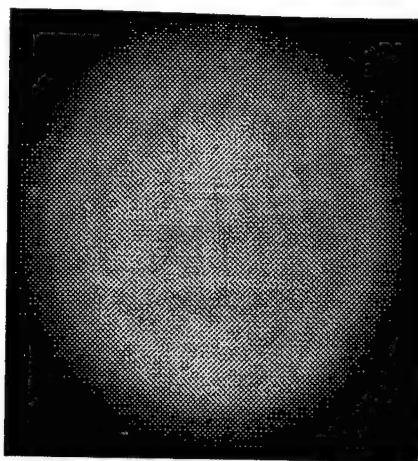


**Figure 4.11** Tripled Nd:YAG burn pattern taken on exposed Polaroid film.

## 4.2 Troubleshooting and Experience

When the measurements on the OPO were made several problems were encountered. In this section some of these problems are discussed together with their possible causes and what can be done to solve or avoid these problems.

The OPO system is sensitive to external influence, such as mechanical impact, temperature changes and drafts. Especially the master oscillator is very sensitive, since a small change in the direction of the pump beam will change the phase matching condition and a different wavelength will be generated. This wavelength will not be resonant in the cavity unless the position of the tuning mirror is changed.

A small displacement of the pump beam can be cancelled by a small rotation of the BBO crystal as shown in Fig 4.14. This is done by changing the setpoints of the crystal in the control unit while the tuning mirror setpoints remain constant. If the displacement is too large, the pump beam will travel at a skew angle in the cavity and collinear phase matching (all k-vectors parallel) is no longer possible. This will limit the tuning range and also affect how the gain of the master and power oscillator overlap at different wavelengths. A full re-alignment is normally not necessary when these problems are encountered. By carefully adjusting some of the pump beam mirrors, the system can be brought back to where it was.

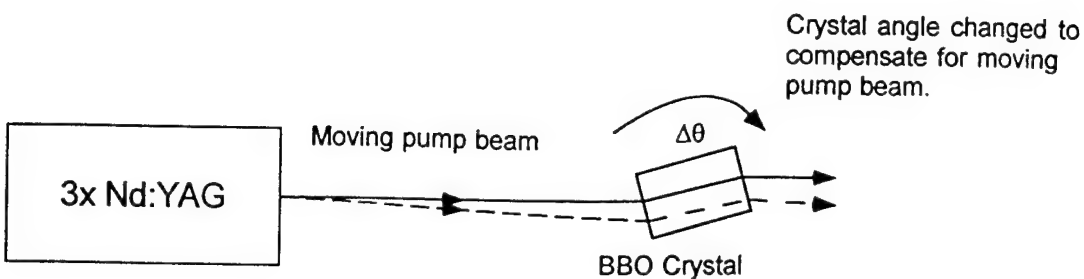


**Figure 4.14** MOPO alignment procedures. A drop in MOPO output often is the result of a minute shift in the direction of the pump beam. According to the manual such daily shifts can be compensated for by changing the crystal angle. However, large or small accumulative changes cannot be corrected by this method but needs to be corrected inside the MOPO.

If the output power of the OPO drops it is useful to know whether the pump power has dropped or not. If the pump power is constant this could indicate a mere displacement of the beam as described above. To aid the user in monitoring the pump power a photo diode inside the MOPO continuously measures the pump power. When using the OPO system we consistently found that the reading of the photo diode dropped during the day. The reasons are probably twofold. The response of the photo diode changes as it is exposed to UV light over a long time. It could also be a heating effect in the KD\*P crystals in the SHG and THG which changes the refractive index of these crystals. During re-alignments of the system we also found that the photo diode reading was affected by where it was hit by the pump beam, so that if the pump beam moved the photo diode reading changed. Unfortunately we had no other way of measuring the pump power other than the photo diode because the high peak powers ( $\sim 10^8$  W) of the pulse combined with its wavelength (355 nm) could destroy our power meters.

A small change in the output power is not necessarily serious since the power oscillator is pumped well above threshold and the changes in the output power will be acceptable. The master oscillator however, is closer to threshold in certain wavelength regions. Should the master oscillator fail, the power oscillator will not be seeded and the output power will drop dramatically. If the FDO is used, the decrease in power will lead to poorer conversion. More important, the OPO output will have a large linewidth and only part of the beam can be properly phase matched. Figure 4.15 shows the doubled output when the power oscillator only is properly seeded around 500 nm.

on the distance between the atoms in the molecule. The rotational and vibrational transitions are dependent on the movement of the nuclei and the energy gaps are small compared to electronic transitions. Electronic transitions have typical energies in the visible and UV region. [50]

Different kinds of scattering processes compete with the absorption in the medium. When the scattering is elastic, i.e. the scattered light has the same energy as the incoming light, it is called Rayleigh or Mie scattering. Rayleigh is due to scattering from smaller particles, less than the light wavelength, while Mie scattering is due to scattering from larger particles. Rayleigh scattering is highly angle dependent with a minimum of scattering perpendicular to the incoming beam. The Raman effect is inelastically scattered light. The molecule is picking up some of the photon energy and transfers it to rotational or vibrational motion. Raman scattering can be shifted both to higher and lower frequencies. [50]

Table 5.1 shows cross sections for different radiation and scattering processes. The values are typical but vary depending on the medium. As can be seen, the cross section for Raman scattering is three orders of magnitude smaller than the cross section for Rayleigh scattering. It is also notable that the fluorescence process has a cross section several orders of

magnitude greater than Rayleigh scattering. The intensity of Mie scattering depends on factors such as particle radius and absorption.

In atomic spectroscopy, specific transitions can be resolved and detected. The spectral resolution is dependent on many parameters, e.g. linewidth of the excitation source and type of detection equipment. As was mentioned, large complex molecules

Process	Cross section $\sigma$ [cm <sup>2</sup> ]
Resonance absorption	$10^{-16}$
Fluorescence	$10^{-16}$
Fluorescence (quenched)	$10^{-20}$
Rayleigh scattering	$10^{-26}$
Raman scattering	$10^{-29}$
Mie scattering	$10^{-26} - 10^{-8}$

Table 5.1 Comparison between typical cross sections for different radiation and scattering processes. [50]

have many more energy levels forming wide energy bands resulting in broad fluorescence spectra. These spectra are harder to resolve because the very small energy gaps due to vibrational and rotational transitions may be overlapped. Instead of studying the specific lines, the shape of the fluorescence spectrum is studied over a wider wavelength range.

The fluorescence is dependent on the environment and the signal may be reduced due to several factors. The intense UV light (from e.g. a laser) may cause photochemical destruc-

tion (photobleaching) in the fluorescent medium. The fluorescence intensity will gradually decrease and thus result in an incorrect intensity reading.

Quenching, competing deactivation processes, can also be a problem. The quenching can have different origin such as collisions between excited molecules and molecules from the solvent. Temperature quenching may result in a decrease in the fluorescence signal for some compounds with as much as 50% for a 10°C temperature change. It is therefore important that the compounds are kept at the same temperature during the fluorescence measurements. Another quenching process is oxygen quenching. The fluorescence intensity can be reduced as much as 20% due to oxygen quenching and the degree of oxygen quenching should be investigated for every solution. [19]

Reabsorption may be another reason for an incorrect fluorescence signal. This happens when the emitted photons are reabsorbed either by the fluorescing medium or the solvent.

When using a bright excitation source such as a laser, the electronic transitions may be saturated. This happens when almost every molecule is excited. An increase in the photon flux will then not result in a higher fluorescence signal. All the factors above must be considered when quantitative measurements are made. [19,52]

## 5.2 Laser-Induced Fluorescence Set-up

Lasers are widely used in spectroscopic applications due to their high intensity and narrow linewidth. Lasers can be used in both pulsed and continuous mode. With pulsed lasers, higher peak powers are obtained and pulsed lasers are often used for fluorescence lifetime measurements. Continuous lasers on the other hand can be constructed with a narrower linewidth, which are used in detection of single transitions in atoms and molecules.

Figure 5.4 shows a typical LIF set-up. A tuneable laser is used as light source. It is then possible to tune the laser to an allowed dipole transition wavelength in the medium. A focusing lens is used to increase the photon intensity of the laser beam. If the laser is operating in the UV region, the lens must be made of a UV graded material. The light that is not absorbed or scattered in the probe volume is captured in a beam dump. A collecting lens is used to increase the detectable fluorescence light and to match the F number of the spectrometer. The focusing lens and the collection lens define the probe volume. A filter or spectrometer is used to select

## CHAPTER 5

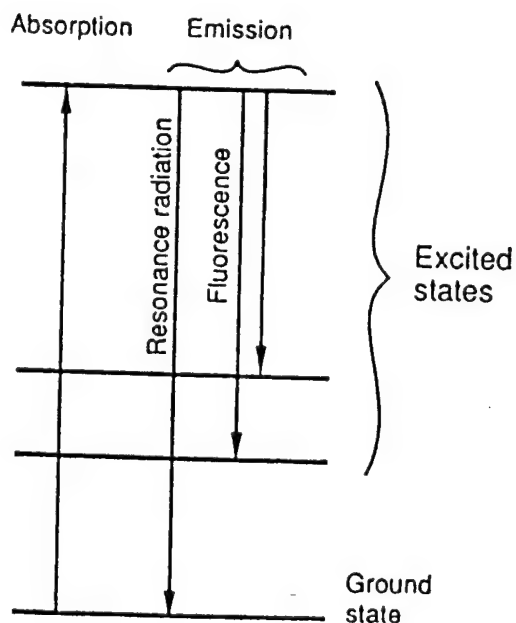
### BACKGROUND THEORY: LASER-INDUCED FLUORESCENCE

Fluorescence is a radiational deexcitation process which occurs after light has been absorbed by an atom or a molecule. Fluorescence spectroscopy is used as a method to detect small concentrations of specific atoms or molecules. By using a laser as a light source (laser-induced fluorescence), the sensitivity and the signal to noise ratio is increased. A laser also has a high intensity within a narrow frequency region increasing the spectral resolution. This chapter discusses the theory behind fluorescence spectroscopy. The different parts in a typical LIF set-up are discussed and an equation for the ideal fluorescence intensity is discussed.

#### 5.1 Basic Fluorescence Theory

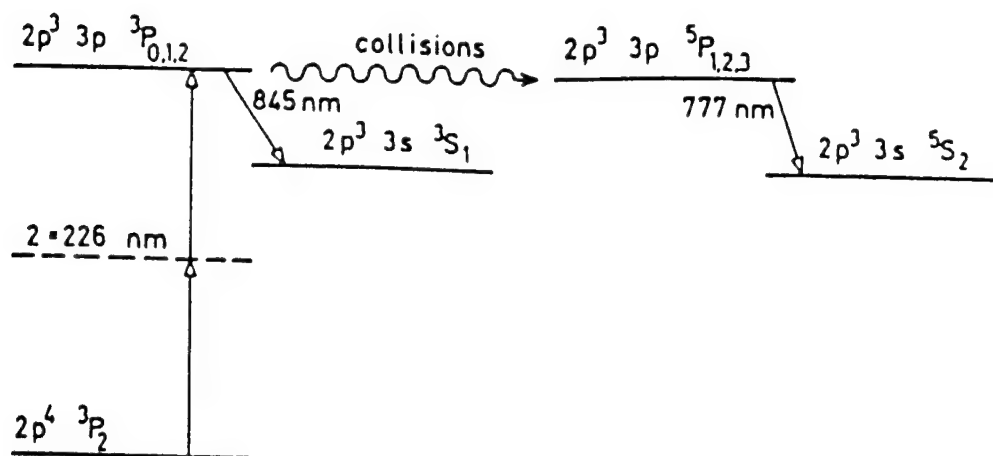
When light is sent into a medium, the photons interact with the medium in different processes. The photons may be absorbed by the atoms in the medium or scattered with or without losing energy (inelastic or elastic scattering).

Resonance absorption occurs when the excitation light energy corresponds to an allowed transition in the atom. Fluorescence occurs when the excited atom deexcites to energy



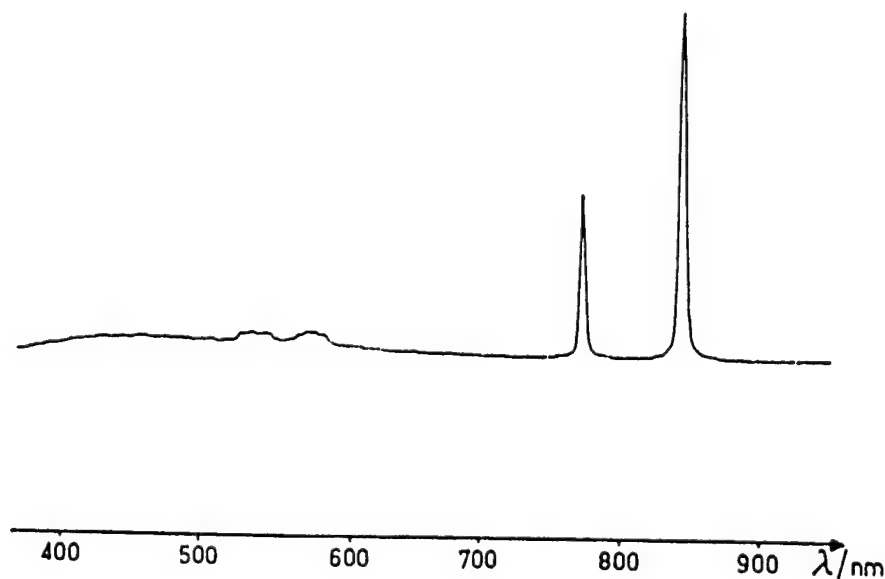
levels above the ground state by emitting a photon of lower energy (longer wavelength) than the excitation light [50]. Figure 5.1 shows the principle of the fluorescence process. The possible transitions are determined by certain optical transition selection rules [20,50]. These selection rules are determined by laws of conservation of angular momentum and considerations of symmetry. The number of energy levels is increased with the complexity of the molecule due to rotational and vibrational transitions and bands of energy levels are common in large molecules.

Figure 5.1 Schematic of energy levels and transitions involved in fluorescence [50].



**Figure 5.2** Typical LIF showing two-photon excitation (226 nm) scheme for oxygen atoms and fluorescence transitions occurring at 845 nm and 777 nm. [50]

Figure 5.2 shows a two-photon excitation scheme for oxygen with two possible fluorescence transitions. Figure 5.3 shows the relevant fluorescence spectrum from the fluorescence transitions in Fig. 5.2.



**Figure 5.3** Laser-induced fluorescence spectra from oxygen atoms in a  $C_2H_2$  welding torch for two-photon excitation at 226 nm. [50]

Vibrational transitions are possible when the molecules consist of two or more atoms while rotational transitions are possible for molecules consisting of at least two different atoms. Rotational transitions occur when the rotation of the molecule is changed. Vibrational transitions are due to the change in the dipole moment of the molecule. The dipole moment depends

lens has approximately 5% reflectance in every surface. The efficiency of the grating is 50% and the mirrors in the spectrometer have a total reflectance of 90%. This results in a total transmission efficiency of 40%. A CCD detector is used and the quantum efficiency is 20%. It is assumed that there is no saturation in the sample. This fluorescence set-up would result in a measurable fluorescence intensity,  $I_f$  of  $0.5 \text{ mW/cm}^2$  which is an easily detectable signal.

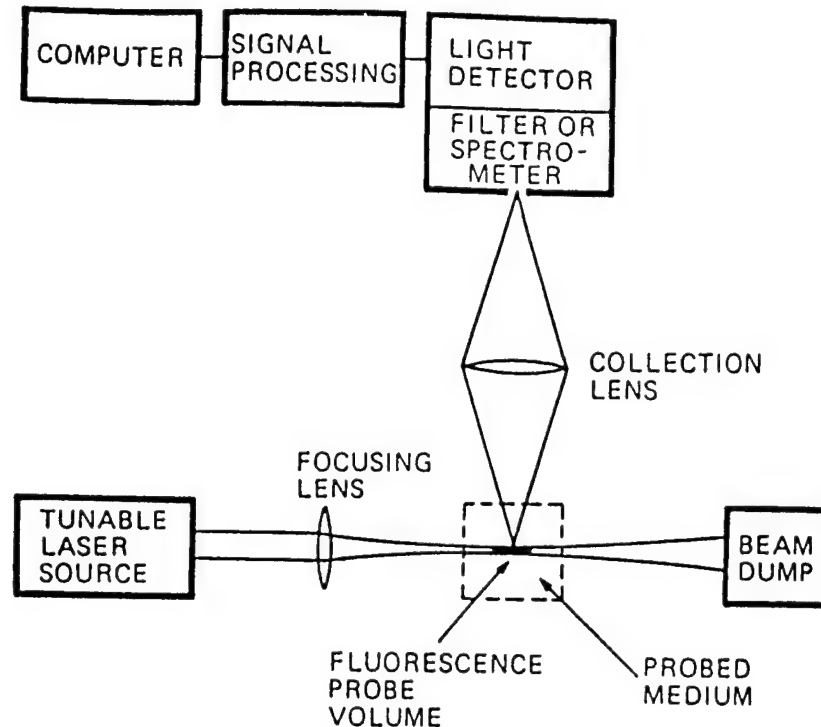


**Figure 5.4** Schematic diagram of a typical laser-induced fluorescence experiment set-up. [39]

the wavelength region of interest. In the spectrometer, a grating or a prism is used to convert the wavelengths to angles. The detector could be a photo multiplier tube (PMT) or a CCD camera. The detector is transforming the photon energy to an electronic charge or voltage and the signal is then processed and displayed with the help of a computer as shown in the diagram.

### 5.3 The Ideal Fluorescence Equation

This chapter will discuss the different variables in an ideal fluorescence equation. The detected fluorescence signal is not only dependent on the fluorescing compound but also the collection optics and the detector.

When the laser photons hit the compound, the molecules absorb the photons. The absorption is dependent on the laser intensity,  $I_0$ , the absorption cross section,  $\sigma_{abs}$ , for the compound, the number of molecules per unit volume,  $N$ , the absorption path length,  $l$ , and the number of molecules in the absorbing state,  $\Delta n/n$ , due to the Boltzmann distribution. If the laser intensity is very high, the transitions will be saturated. A correction for saturation,  $Y$ , must be added to the equation. When the molecules are excited, some of them return to the ground

state by emitting fluorescence light and others deexcite through relaxation and collisions. The fluorescence quantum yield,  $f$ , is the ratio of the number of quanta emitted as fluorescence to the quanta absorbed. The fluorescence is emitted uniformly in all directions and the collection lens covers a solid angle of  $\Omega$  radians. This gives a collection efficiency of  $A_{lens} / 4\pi r^2$ , where  $A_{lens}$  is the area of the lens and  $r$  is the distance from the probed medium to the lens. The total transmission efficiency  $T$  includes absorbed, reflected and scattered light through the collection lens and the spectrometer. Finally, the detector has a quantum efficiency  $\eta$ . This results in the fluorescence equation [19,26,52]

$$I_f = I_0 \cdot \sigma_{abs} \cdot l \cdot N \cdot f \cdot \frac{\Omega}{4\pi} \cdot \frac{\Delta n}{n} \cdot Y \cdot T \cdot \eta. \quad (5.1)$$

In this equation, it is assumed that the absorption is uniform through the medium. This is true for dilute concentrations of the species. It is also considered that there is no photodestruction. The following example will give the reader an idea of order of the fluorescence intensity that is detectable. The numbers are realistic, estimated values for a typical LIF experiment in a gas sample.

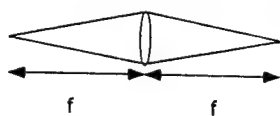
### Example

In this example, a continuous laser with an intensity of  $10 \text{ mW/cm}^2$  is used. A gas sample with concentration  $2 \cdot 10^{19}$  molecules per  $\text{cm}^3$  is used. This is the concentration of molecules in an ideal pure gas at normal pressure and room temperature. It is assumed that all of the molecules are in the ground energy state. The absorption cross section for our species is  $1 \cdot 10^{-16} \text{ cm}^2$  and the absorbing path length is 2 mm. The fluorescence quantum yield is calculated by using the lifetime for fluorescence and for nonradiative processes.

$$f = (1/\tau_{rad}) / (1/\tau_{rad} + C_{rel+coll}) \quad (5.2)$$

where  $\tau_{rad}$  is the radiative lifetime of the excited state and  $C_{rel+coll}$  is the sum of collision and relaxation rate for the excited state. Assume that the two processes have the same lifetime which results in a quantum yield of 0.67. The diameter of the collection lens is 20 mm and it is mounted 80 mm from the sample. This gives a collection efficiency of 0.2%. The collection

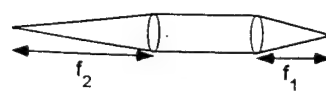
### I. One lens collection system



$$\text{Input F\#} = \text{Output F\#} = f / D$$

$$\text{Collection efficiency: } (1/4 \text{ F\#})^2 = D^2 / 16 f^2$$

### II. Two lens collection system



$$\text{Input F\#} = f_1 / D; \text{ Output F\#} = f_2 / D$$

$$\text{Collection efficiency: } D^2 / 16 f_1^2$$

Note: Second lens is used to match F\# of spectrometer

**Figure 6.2** Collection efficiency and F number (F#) for a one-lens system and a two-lens system. The lens diameter is D and focal length is f.

#### Example comparing a one-lens collection system with a two-lens collection system

A spectrometer with  $F\# = 4$  and a lens with diameter  $D$  and a focal length  $f$  is given. The collection efficiency is given by the area of the lens divided by the area of a sphere with radius  $f$ .

#### One-lens collection system

The collection efficiency will be  $\frac{\left(\frac{D}{2}\right)^2 \pi}{4\pi \cdot f^2} = \left(\frac{D}{4f}\right)^2$  and the  $F\#(\text{Lens}) = \frac{f}{D}$ . This results in the collection efficiency  $\left(\frac{1}{4F\#}\right)^2$ .

The collection efficiency will in this example be  $1/256 = 0.4\%$

#### Two-lens collection system

The collection efficiency will be  $\frac{\left(\frac{D}{2}\right)^2 \pi}{4\pi \cdot f_1^2} = \left(\frac{D}{4f_1}\right)^2$  and the  $F\#(\text{Lens2}) = \frac{f_2}{D}$ . The first lens is

chosen to give a high collection efficiency e.g.  $D = 20$  mm and  $f_1 = 35$  mm resulting in a collection efficiency of 2%.

The second lens is chosen to match the spectrometer.  $D = 20$  mm and  $f_2 = 80$  mm give a correct F#.

As can be seen in the above example, the two-lens collection system is about five times more efficient than the one-lens system (i.e. 0.4% compared to 2%). However, in a two-lens collection system, a fast focusing lens is used to collect as much light as possible and a problem

using these thick lenses may be aberrations. Aberrations may cause a distorted image on the detector and influence the wavelength calibration.

### 6.3 Transmission of Optical Materials

When light is propagating through an optical material, it loses intensity due to reflectance at the surfaces and absorption in the material. The reflectance at every surface is approximately 4 % at perpendicular incidence although the reflectance can be reduced using AR coated surfaces. Less than 2 % of the light is absorbed in the lenses in the visible wavelength region for most materials as shown in Figs. 6.3-6.5.

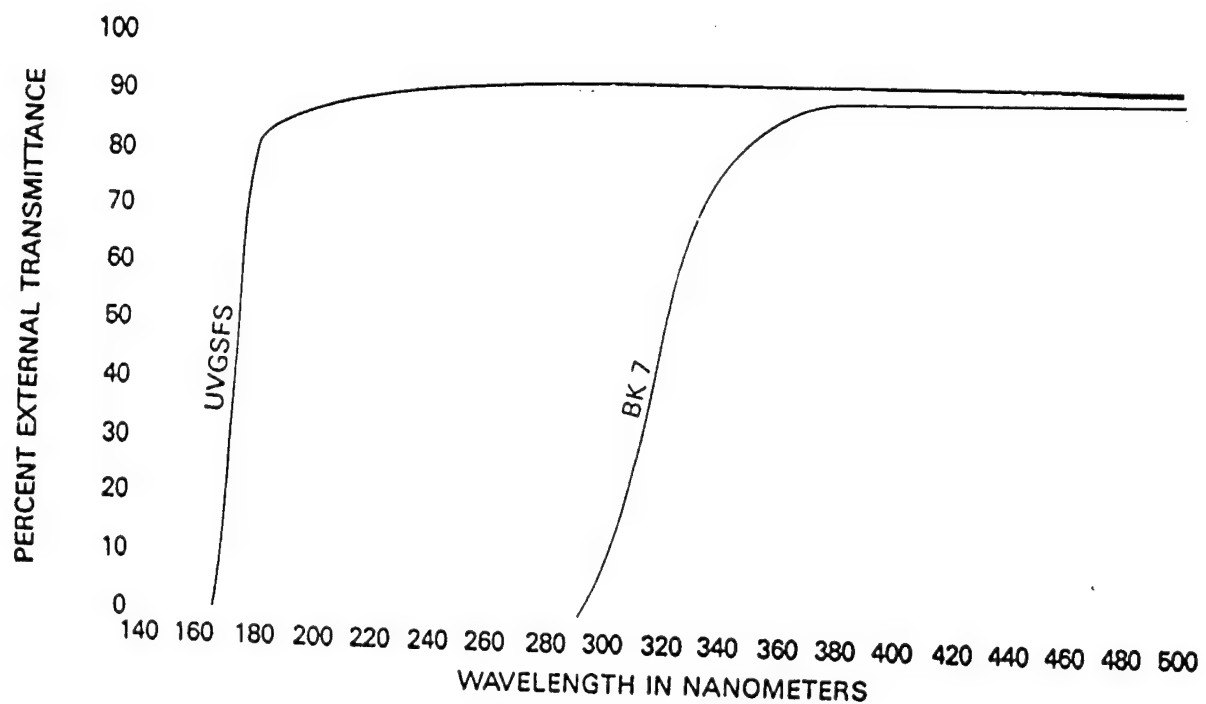


Figure 6.3 Transmittance curve for UV grade fused silica (UVGSFS) and BK 7 glass (1 cm thick). [35]

The absorption is rapidly augmented in the UV region for normal glass such as Pyrex and BK 7 glass and the glass is emitting a bright fluorescence light. The transmission curves for these materials are shown in Figs. 6.3 and 6.5. There are several optical materials which do not absorb in the UV region such as UV grade fused silica and UV grade calcium fluoride. Transmission curves for these materials are shown in Figs. 6.3-4. UV grade fused silica is a high quality quartz glass.

## CHAPTER 6

### TRANSMISSION AND EFFICIENCY CONSIDERATIONS FOR LIF DETECTION OPTICS

Only a fraction of the emitted fluorescence light is detected. The purpose of this chapter is to discuss optical properties of the different components in a collection and detection system to optimise the fluorescence signal. The optics must be suited to the intense UV laser light as well as the faint UV fluorescence light.

#### 6.1 Properties of the Atmosphere

The transmission of the atmosphere is dependent upon the absorption of optical radiation due to different molecules in the atmosphere. Figure 6.1a shows the transmission and absorption of the atmosphere for a 1 km path and Fig. 6.1b shows the calculated

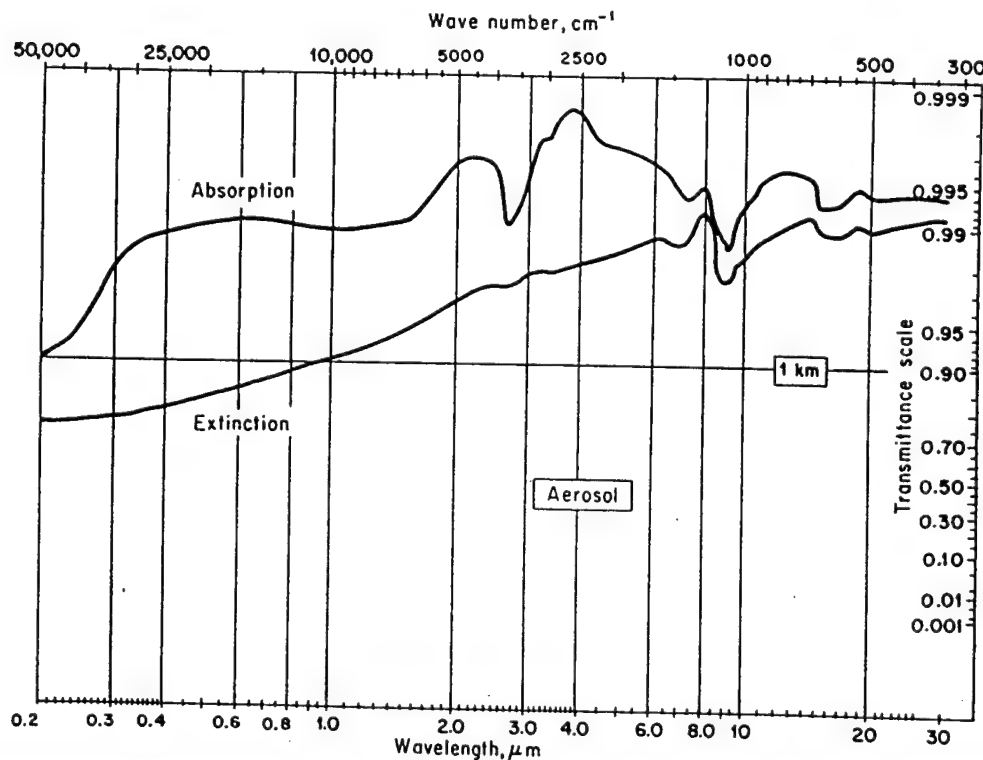


**Figure 6.1a** Transmission of the Ambient Atmosphere showing contributions due to aerosol absorption and extinction (absorption + scattering) for a 1 km path length. [32]

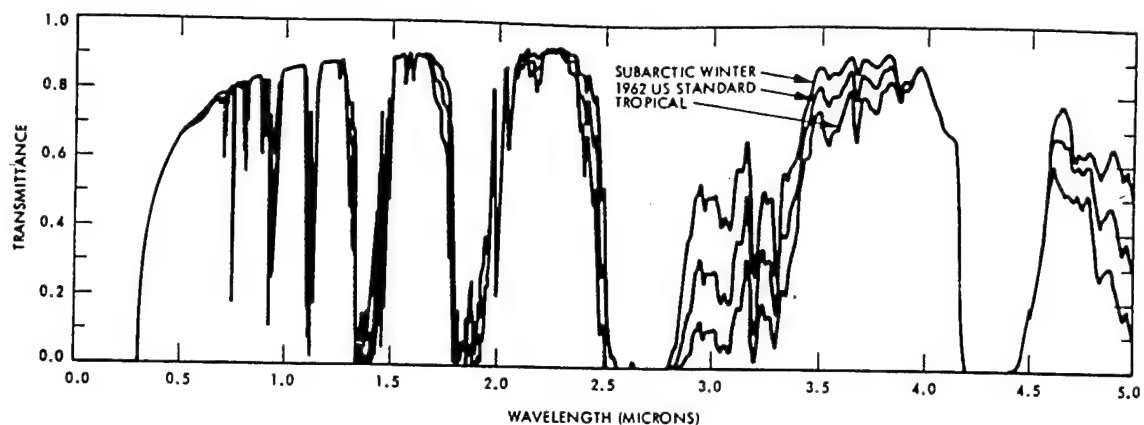


**Figure 6.1b** Calculated transmission of the atmosphere using the LOWTRAN broadband molecular spectra model. [33]

transmission through the entire atmosphere using the LOWTRAN database. As can be seen, the molecular absorption is quite strong in those spectral regions where the molecules have strong resonant absorption lines, but relatively clear in the visible spectral region. As is evident, the attenuation in the UV (near 300 nm) is quite strong and increasing with frequency, mostly due to ozone in the atmosphere and some other constituents.

## 6.2 Lens Collection System

There are three main reasons to use a collection lens. First, the F number ( $F\#$ ) of the lens must be matched with the  $F\#$  of the spectrometer to optimise the collection of the light and the resolution of the spectrometer. Second, the object plane must be well-defined to make sure that the fluorescence signal comes from the probe volume. The third and last reason to use a collection lens is to increase the collection efficiency. The bigger lens that is used and the closer to the sample it is placed the more light is collected. Therefore, a lens with a big diameter and a short focal length is chosen. By using only one lens, the collection efficiency cannot be freely chosen without changing the  $F\#$ . To solve this problem a two-lens collection system is used. The first lens (closest to the sample) gives the desired collection efficiency. The second lens is chosen to match the  $F\#$  of the spectrometer. The difference in collection efficiency between a one- and a two-lens collection system is shown in the example below and the different set-ups are shown in Fig. 6.2.

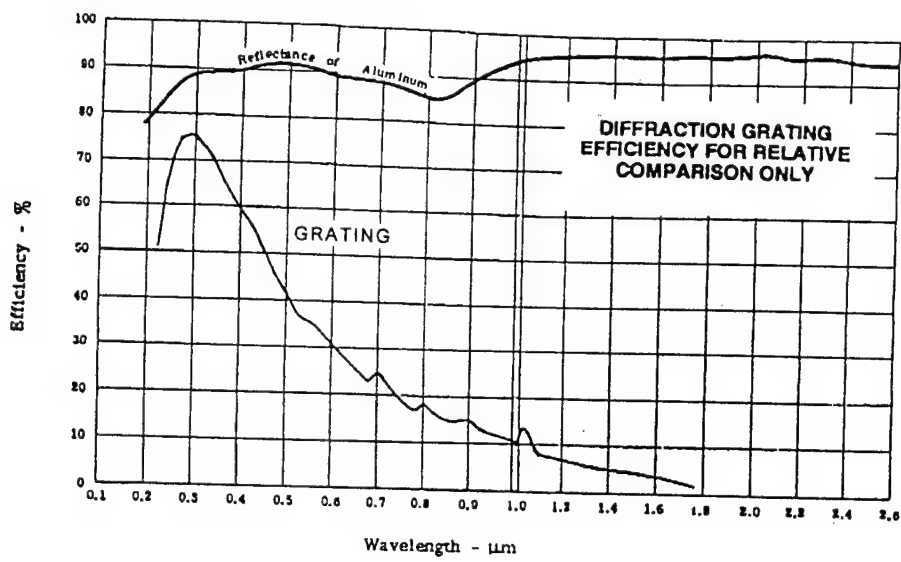


Figure 6.7 Diffraction efficiency for a 300 g/mm grating with 300 nm blaze wavelength. [36]

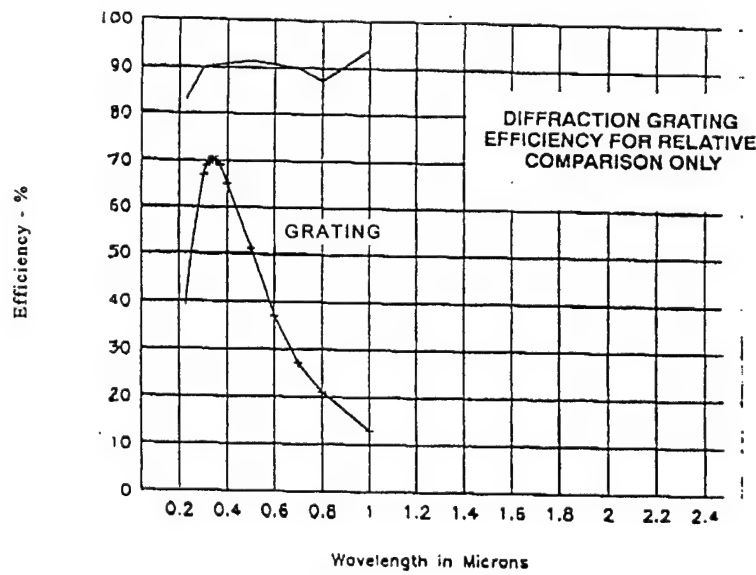
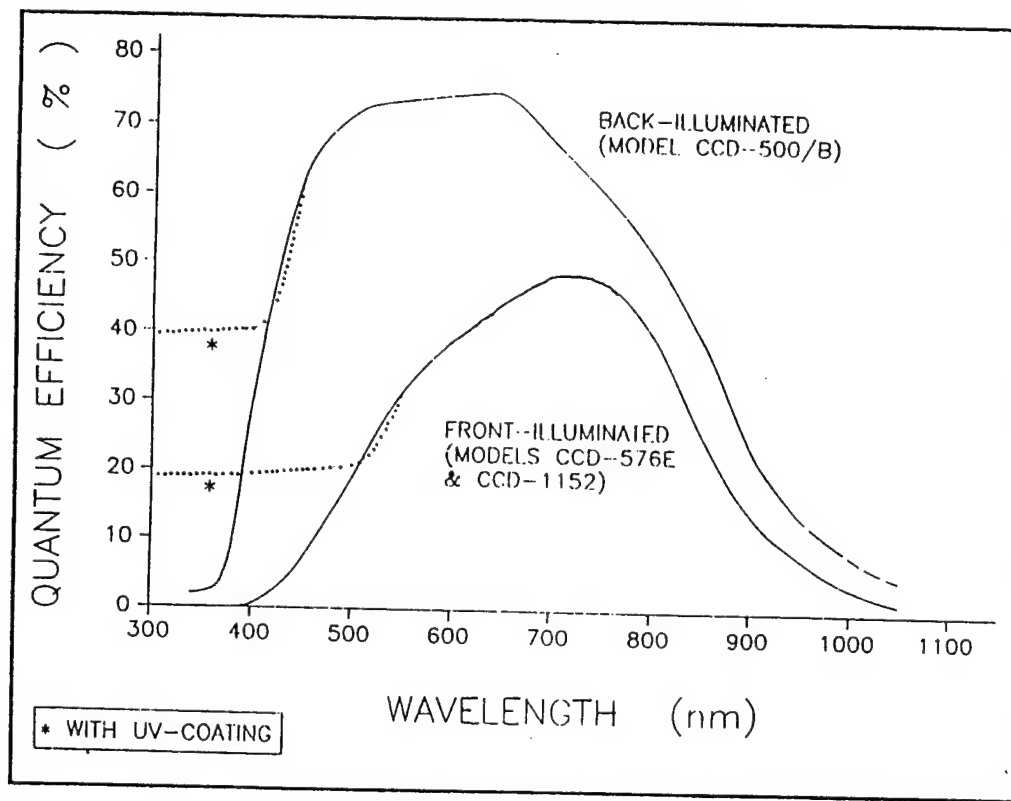
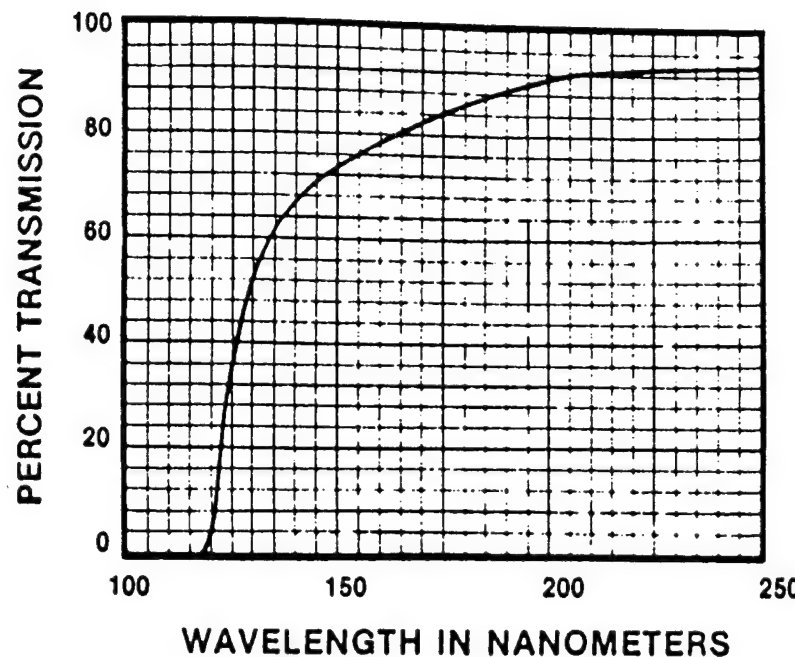


Figure 6.8 Diffraction efficiency for a 150 g/mm grating with 300 nm blaze wavelength. [36]

A CCD detector can be front- or back illuminated. The difference in quantum efficiency is shown in Fig. 6.9. A front illuminated CCD was used in our set-up. The CCD had a UV-to-visible coated converter which, as shown in the diagram, results in a higher quantum efficiency below 500 nm. Notice that the quantum efficiency is constant between 300 and 500 nm. The resolution of the CCD depends on the grating and the entrance slit. The resolution with a 1200 grooves /mm grating and a 20  $\mu\text{m}$  wide entrance slit would be 0.18 nm according to [1].



**Figure 6.9** Spectral response of a CCD with UV-coating. Note: A Front-Illuminated CCD was used in our experiments. [38]



**Figure 6.4** Transmission curve for vacuum UV grade Calcium Fluoride of 2-3 mm thickness. [1]

Optical materials may fluoresce even though they do not seem to absorb a great deal of light. UV fused silica does not fluoresce in the UV, while fluorescence from calcium fluoride has been seen in our experiments.

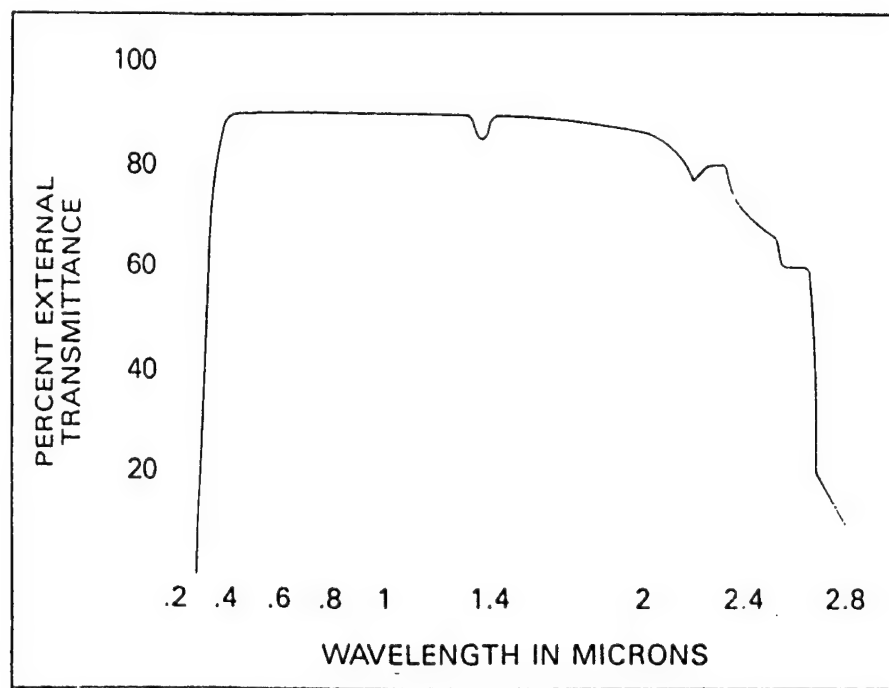


**Figure 6.5** Transmittance curve for Pyrex 7740 glass (8 mm thick). [35]

## 6.4 Properties of Monochromators and Detectors

The entrance slit in front of the spectrometer determines the amount of light entering the spectrometer. The resolution depends on the slit width in two ways. The narrower the slit is, the narrower is the image of the slit on the detector. But if the incoming light is too faint (too few photons), the detection decreases and hence results in a lower resolution.

The monochromator has a grating to resolve the incoming fluorescence light. The groove density of the grating determines the resolution according to  $\mathfrak{R} = N \cdot m$ , where  $N$  is the total number of illuminated lines on the grating and  $m$  the diffraction order.  $\mathfrak{R}$  is called the resolving power. The resolution is  $\delta\lambda = \lambda / \mathfrak{R}$ . For a 150 grooves / mm grating with an illuminated width of 68 mm, the resolving power would be 10200 and the resolution at 300 nm for the grating would be 0.03 nm. This is the theoretical resolution for a perfect grating. Limiting effects such as slit width, number of photons and detector decrease the resolution considerably.

The grating has different reflectance efficiency over the wavelength range. The efficiency is highest at the blaze wavelength where the reflectance normally is up to 70%. The efficiencies for the three gratings used in our set-up can be seen in Figs. 6.6 - 6.8. The efficiencies were measured with  $7.5^\circ$  between incident and diffracted beams. This is similar to the angle conditions in the monochromator. The mirrors inside the monochromator are UV coated to increase the efficiency of the monochromator.

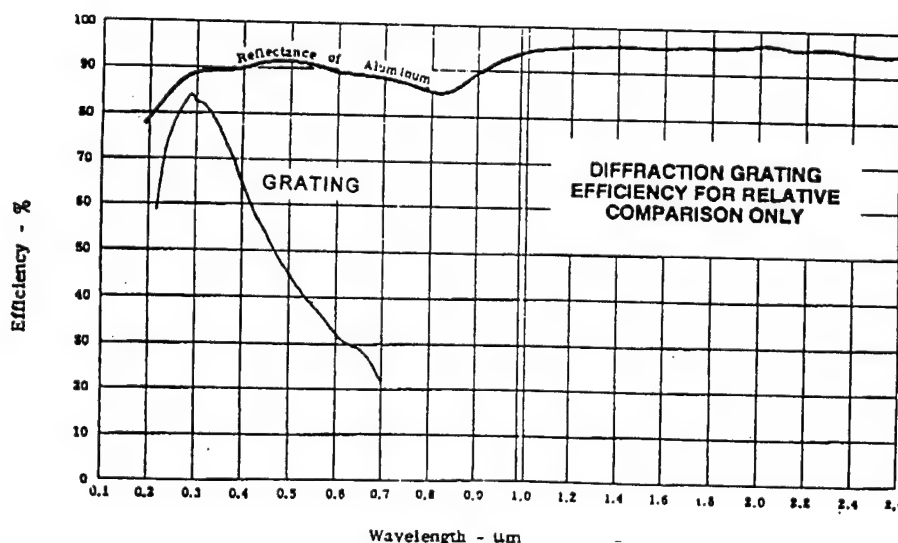


**Figure 6.6** Diffraction efficiency for a 600 g/mm grating with 300 nm blaze wavelength. [36]

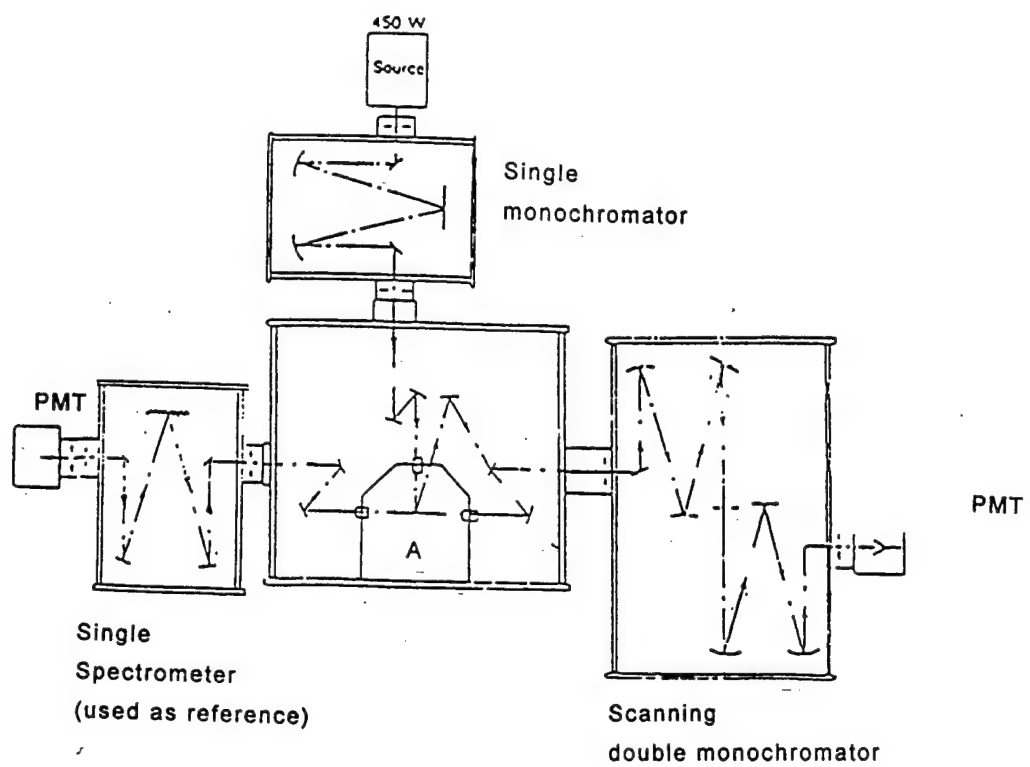


**Figure 7.3** Schematic diagram of a fluorescence experiment. A 450 W Xenon lamp and a single monochromator is used as light source. The sample is placed in A. The fluorescence signal is spectrally resolved in a scanning double monochromator and detected with a PMT. [49]

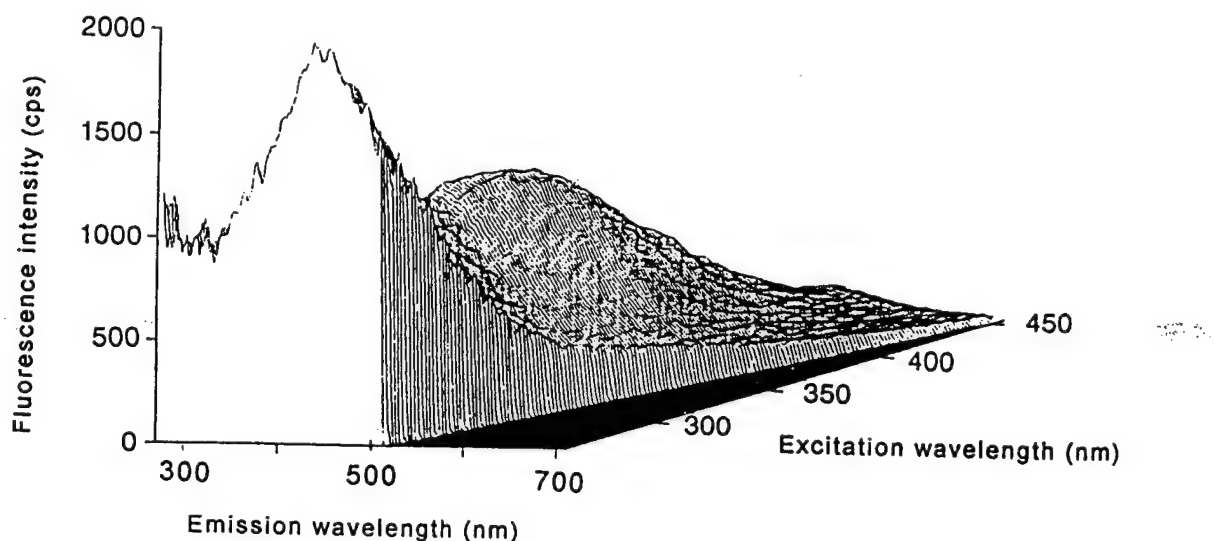


**Figure 7.4** Typical Excitation-Emission Matrix (EEM) spectrum for seawater measured with a double monochromator set-up [11].

monochromator. The light is finally detected with a PMT. The obtained spectrum is corrected for the variance in the lamp intensity and the non-linearity of the PMT. Figure 7.4 shows an EEM fluorescence spectrum for dissolved organic matter (DOM) in seawater from the Black

Sea. Figure 7.5 shows an EEM fluorescence spectrum for a plastic contaminant in water. The EEM spectrum is normalised to the concentration of a standard. This plastic contaminant has been used in our EEM spectroscopy experiments.

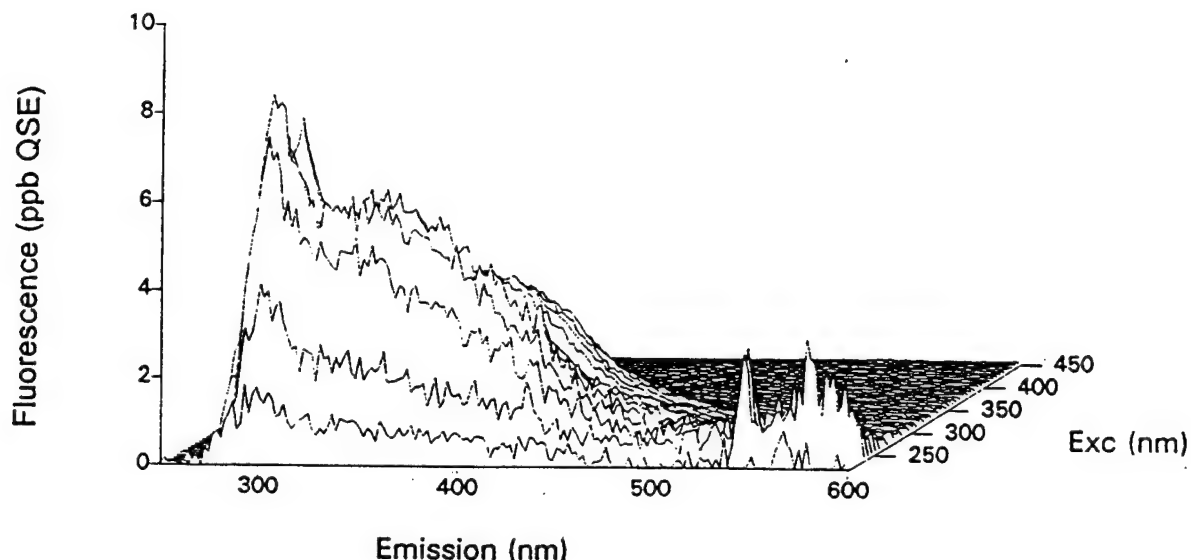


Figure 7.5 EEM spectrum for a plastic contaminant, diglycidal ether of bis-phenol A, in water [14].

### 7.3 Use of Quinine Sulphate as a Standard

There are two ways to compare fluorescence spectra acquired at different places and with different equipment. First, by measuring the signal in absolute radiometric units, which is often difficult to do. Second, by measuring the compound under investigation relative to that obtained for a reference sample. Quinine sulphate (QS) is such a standard used in many fluorescence studies.

The linearity of the fluorescence signal as a function of QS concentration is very good, with less than 1% deviation. The most important property of QS is that the emission spectrum does not overlap with the absorption spectrum as shown in Fig. 7.6. It can also be seen, at the top of the figure, that the photon yield is relatively constant over the wavelength range which increases the accuracy in the concentration calibration. Other considerations are purity and emission spectra as a function of temperature. It has been shown that QS is unstable in solution when exposed to intense radiation. It is not considered being a problem when exposing the QS to the light of a Xenon lamp (a drop of ~1% during 12 hours). The instability increases with small sample sizes, wide excitation bands and high excitation intensity. [55]

## CHAPTER 7

### PREVIOUS FLUORESCENCE MEASUREMENTS OF QUININE SULPHATE AND COMPOUNDS IN WATER

Fluorescence measurements and evaluations of organic and plastic compounds in water have been made by several authors [11-13,54]. This chapter contains a discussion of the optical properties of water and the previous use of Excitation-Emission Matrix (EEM) spectroscopy. Finally, the use of quinine sulphate as a standard for fluorescence experiments is discussed.

#### 7.1 Optical Properties of Water

The main optical processes in water are absorption and scattering. The total absorption coefficient,  $a_w(\lambda)$  [ $\text{m}^{-1}$ ], as a function of wavelength for pure freshwater is shown in Fig. 7.1. However, the absorption coefficient is increased the more impure the water is.

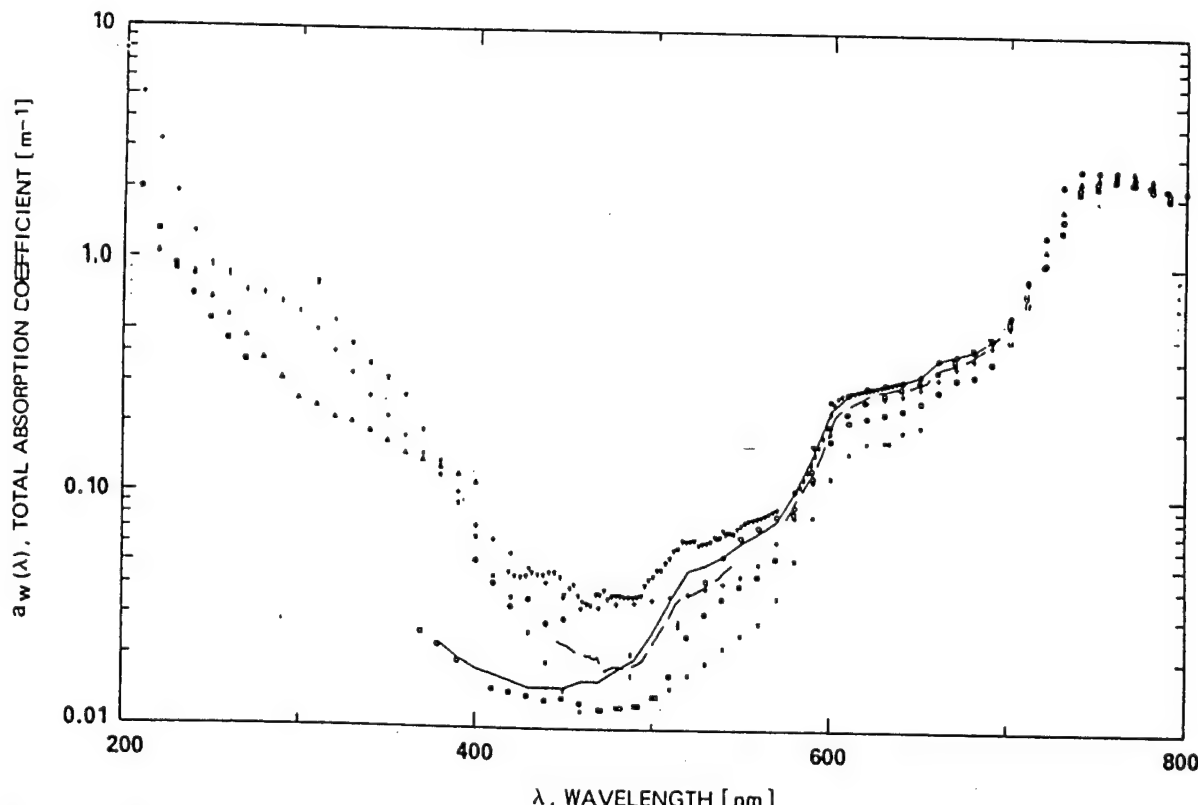


Figure 7.1 Typical absorption coefficients, ( $a_w(\lambda)$  [ $\text{m}^{-1}$ ]) vs wavelength ( $\lambda$  [nm]) measured for pure freshwater by several authors [44].

The scattering depends on purity and solvent. The Rayleigh scattering is rather independent of the purity of the water while Mie scattering is highly dependent on the number of particles in the water. The Raman peak in water is often used as a reference in fluorescence experiments. The Raman shift for water is  $3640\text{ cm}^{-1}$  [25].

While pure distilled water has a low fluorescence, seawater fluoresces considerably more. A typical fluorescence spectrum of seawater is shown in Fig. 7.2. It can be seen that the seawater has a fluorescence peak at 450 nm.

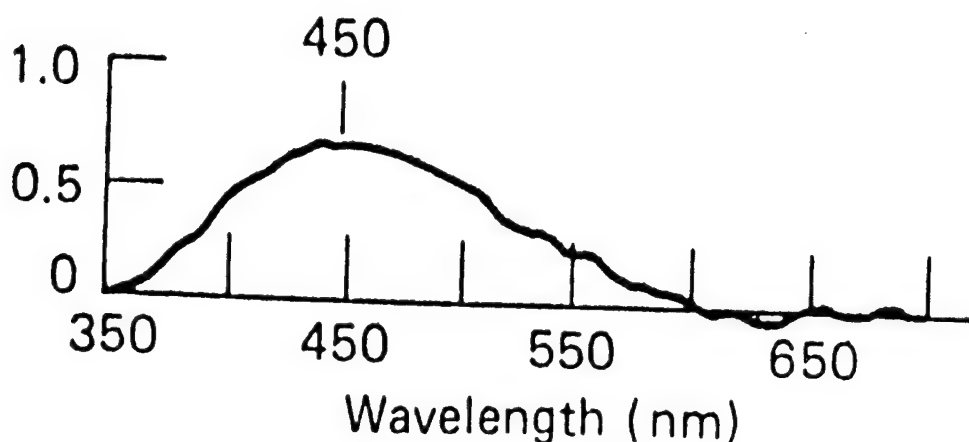


Figure 7.2 Typical fluorescence emission from seawater measured for excitation wavelength 337 nm [34].

## 7.2 Fluorescence of Organic and Plastic Compounds in Water

A lot of research have been done in the environmental field monitoring natural organic compounds in water as well as plastic and oil compounds in water. The monitoring has been done by several authors using different techniques [11-13, 51, 54]. The most frequent method is normal fluorescence spectroscopy using a high-pressure gas lamp or a laser as excitation source. The spectra show the fluorescence intensity as a function of emission wavelength. This technique is used when the characteristics of a compound are well known. EEM spectroscopy uses the tunability of the excitation source and a three dimensional spectrum is obtained, fluorescence intensity as a function of excitation wavelength as well as emission wavelength.

A typical spectrofluorometer used for EEM spectroscopy is shown in Fig. 7.3. The light source is a 450 W Xenon lamp and the wavelength is chosen by a single monochromator. The light passes through the sample and the fluorescence light is sent into a scanning double

## CHAPTER 8

### LASER-INDUCED FLUORESCENCE EXPERIMENTAL SETUP

The tuneable narrow-linewidth UV OPO described in Chapter 3 and 4 was used as the light source for the LIF experiments. The fluorescence light from the LIF experiments was collected by a two lens system and a single grating spectrometer was used to resolve the fluorescence signal spectrally onto a liquid nitrogen cooled UV-enhanced CCD camera. The spectrometer and the CCD were controlled by a PC computer. Figure 8.1 shows a schematic of the LIF experimental equipment and Fig. 8.2 shows a photograph of the set-up. In this chapter a description of the equipment that was used is presented and the experiment alignment and calibration procedures are explained.

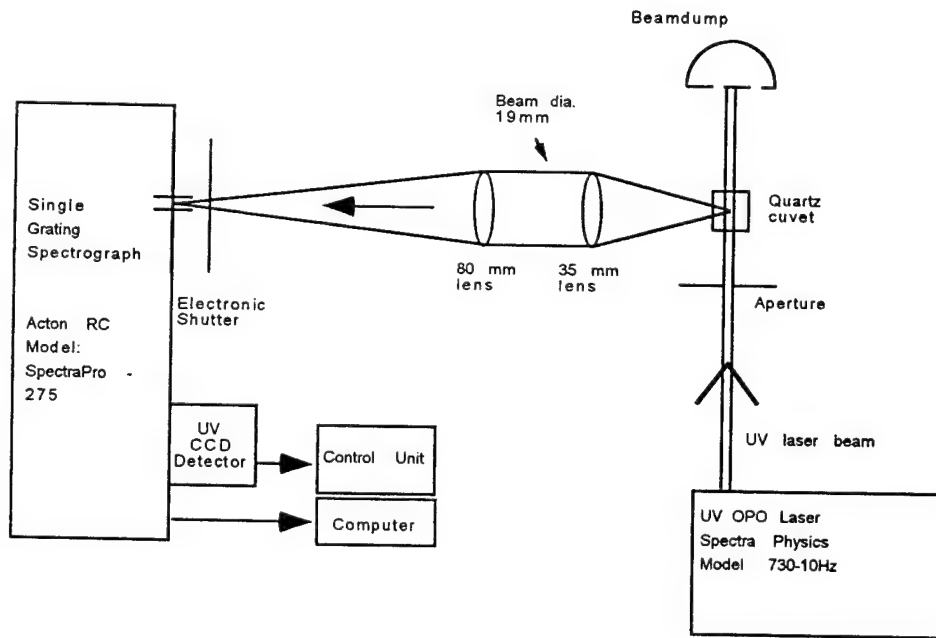


**Figure 8.1** Experiment set-up for laser-induced fluorescence. The set-up was covered with black baffles and black curtains to reduce stray light.

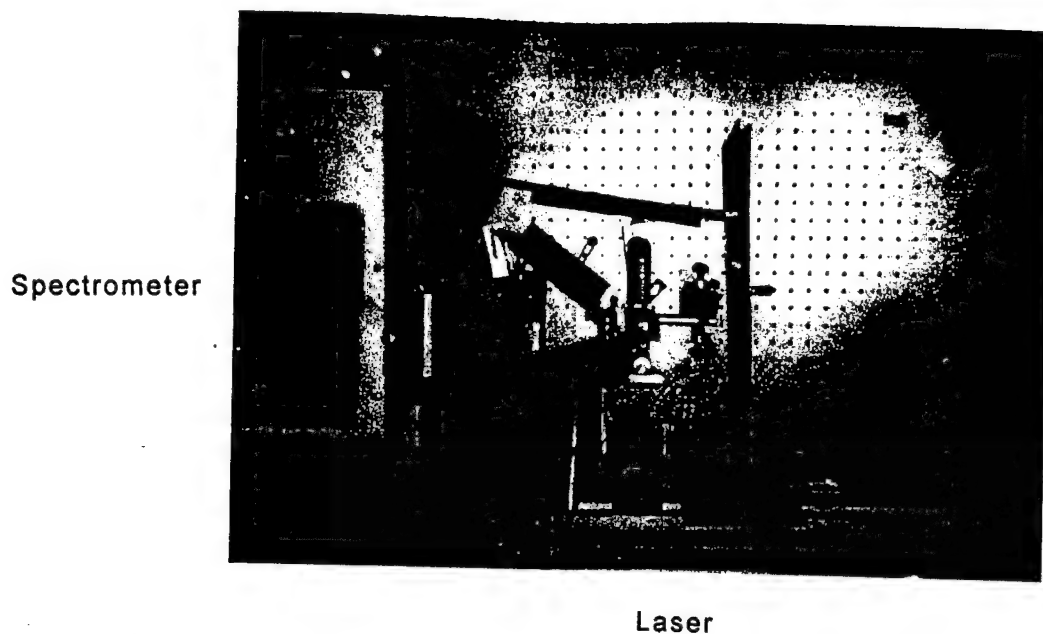


**Figure 8.2** Top-view photo of experiment set-up for laser-induced fluorescence showing laser power meter, cuvet in the centre, collection lenses and light baffles.

## 8.1 Laser Source

As seen in Fig. 8.1, the laser excitation source was a frequency doubled, tuneable, narrow-linewidth UV OPO from Spectra-Physics described in Chapter 3 of this thesis. The tuning range of the UV OPO during the fluorescence experiments was 220 - 330 nm and the laser output energy varied between 0.1 - 7.0 mJ per pulse over the tuning range. The laser beam was directed toward a quartz cuvet which held the fluorescence sample. A 5.2 mm aperture was used to achieve a well-defined size of the excitation beam and to avoid scattering on the edges of the cuvet. The non-absorbed laser beam was sent into a beampump.

## 8.2 Cuvet and Collection Optics

A quartz cuvet was used to hold the fluorescence sample, and to provide an optical window for the excitation laser and the fluorescence light. Figure 8.3 shows a schematic of the cuvet. The cuvet was made of SUPRASIL quartz, had a capacity of 3 ml and was 45 x 12.5 x 12.5 mm in size. The cuvet was mounted in a holder and was tilted to avoid back reflections into the OPO and to decrease the risk of burning the surfaces of the cuvet with the high intensity beam when a focusing lens was used. The pathlength inside the cuvet was 11 mm.

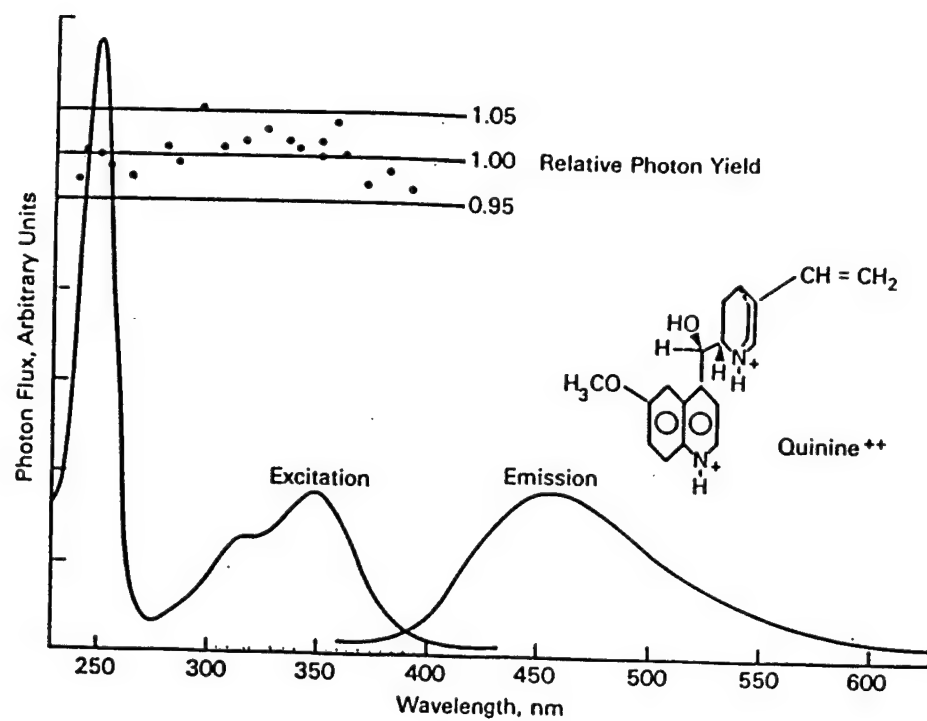


Figure 7.6 Excitation and emission spectra for quinine sulphate in acid media [14].

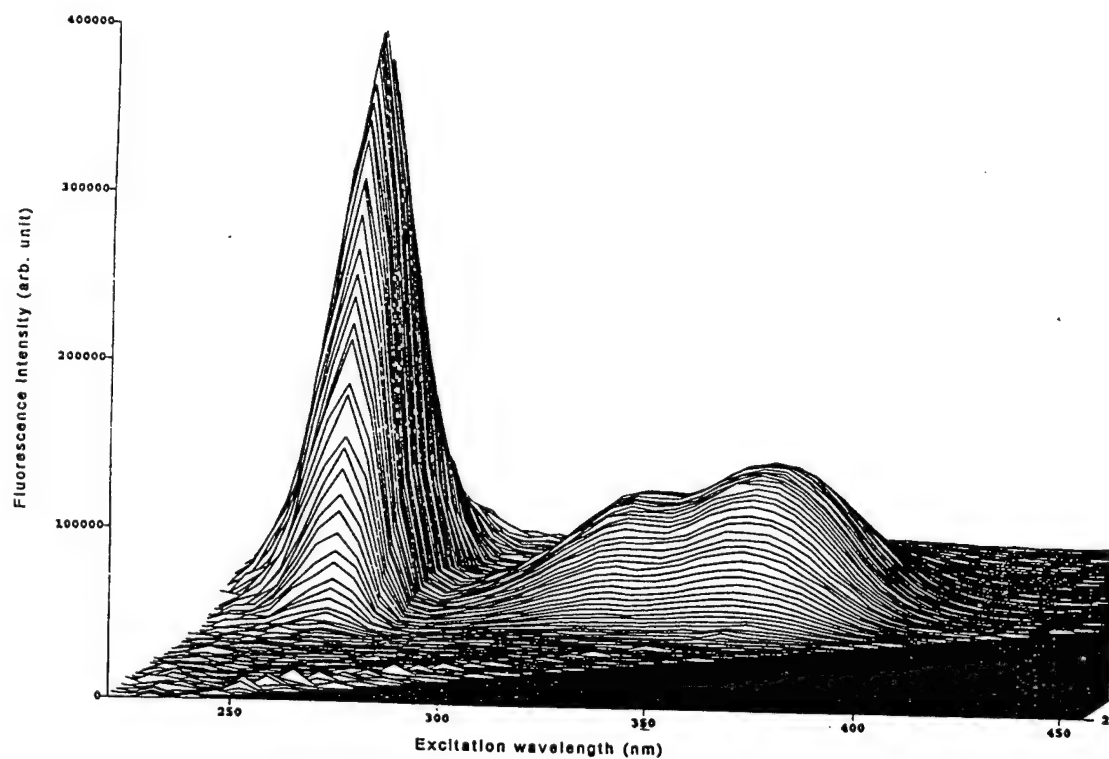
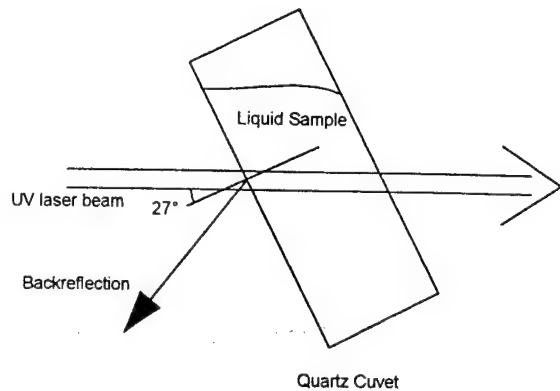


Figure 7.7 EEM spectrum for 10 ppb quinine sulphate using a double monochromator set-up [14].

The quinine sulphate is diluted in sulphuric acid and ultra pure water and should be stored in a dark refrigerator. The primary solution has a lifetime of a month while every dilution of the primary solution should be prepared fresh every week. The primary solution has a concentration of 1 ppm. It is common to normalise the spectra on a daily basis with help of the strength of the Raman peak. In this way, it is not necessary to prepare QS solutions every day.

It was recommended to measure the emission spectrum with a similar set-up to the one used by [55]. Figure 7.7 shows an EEM fluorescence spectrum for 10 ppb QS. The set-up is shown in Fig. 7.3. The spectrum is corrected for nonlinearities in the set-up and shows the same characteristics as the excitation spectrum in Fig. 7.6.

The collection lenses were made of UV fused silica to reduce the fluorescence of the lenses. The diameter of the lenses was 25 mm but was reduced to 19 mm by the lens mount.



**Figure 8.3** Laser beam / cuvet geometry: To avoid backreflection the cuvet was tilted. The fluorescence signal was collected perpendicular to the UV laser beam.

The focal length of the first collection lens was 35 mm and the second lens was 80 mm. The focal length of the second lens was chosen to match the  $F\#$  (3.8) of the spectrometer.

As can be seen in Fig. 8.2, black light baffles surrounded the set-up to decrease stray light from the tripled Nd:YAG laser at 355 nm. The light baffles were placed close to the first collection lens to minimise the amount of scattered laser light entering the spectrometer.

### 8.3 Spectrometer

A single grating spectrograph from Acton Research Corporation (Model SpectraPro - 275) was used. The gratings and mirrors in the spectrometer were mounted in a Czerny-Turner arrangement, as shown in Fig. 8.4. The spectrograph had three different gratings installed on a turret. The three gratings were all blazed at 300 nm and had ruled lines of 150, 300 and 600 grooves / mm. The 150 grooves / mm grating was used in our experiments and had a dispersion of  $\sim 24$  nm/mm and a grating efficiency shown in Figure 6.8.

The mirrors in the spectrograph were UV coated. The width of the entrance slit was adjustable from  $10 \mu\text{m}$  to 3 mm. The exit slit was replaced by a UV-enhanced CCD camera. The stepper motor for the grating was controlled by a separate unit. The control unit was interfaced to a PC computer through the COM-2 port. [1]

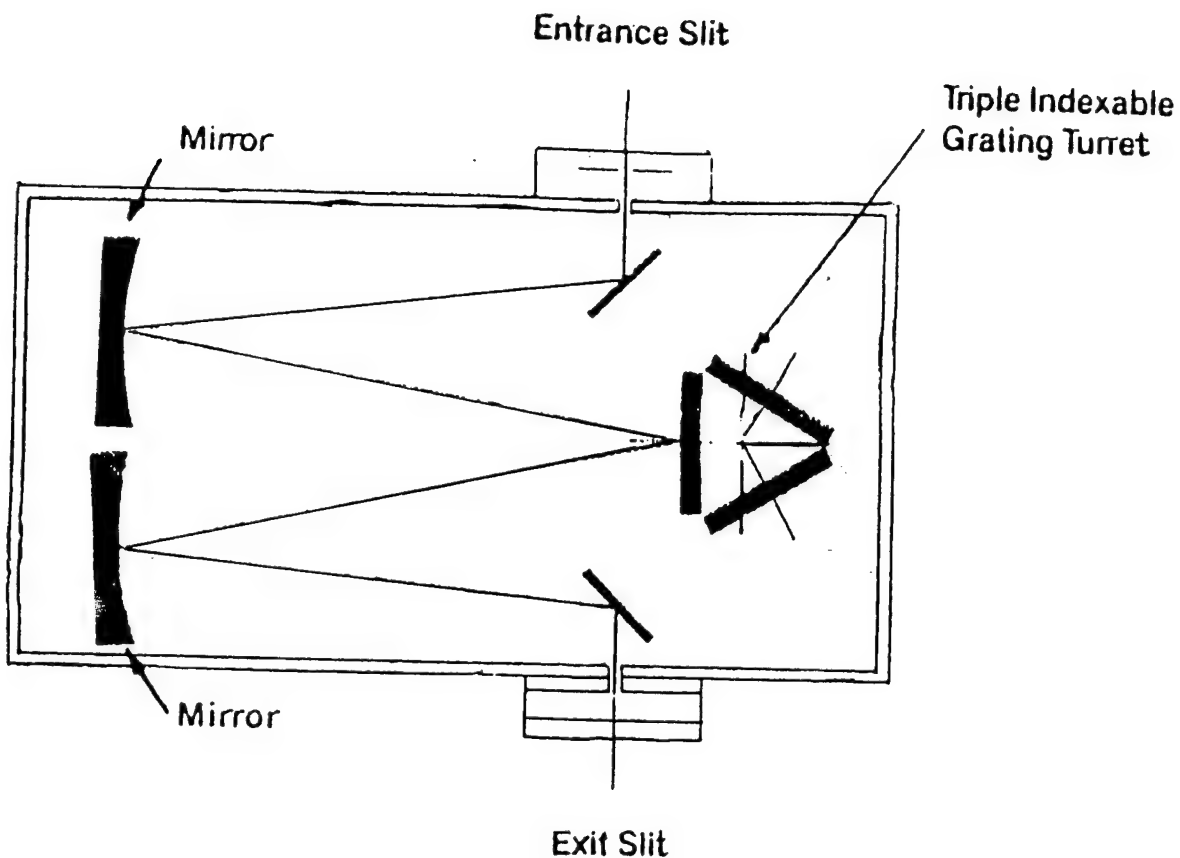


**Figure 8.4** Schematic of ARC Model SP-275 spectrograph. The mirrors are UV coated and the exit slit was replaced by the UV CCD camera. [1]

#### 8.4 CCD Detector

The exit slit of the spectrometer was removed and a CCD detector was placed at the exit focal plane. The liquid nitrogen cooled, front illuminated CCD detector was from Princeton Instruments, Inc. (Model LN/CCD - 576 E/UV) and used a CCD chip from EEV (Model 86 230) with a 576 (row) x 384 (column) pixels format. The pixel dimensions were 22 x 22  $\mu\text{m}$  and the total array size was 13.6 x 6.8 mm. The CCD was controlled by a Princeton Instruments controller (Model ST - 130). The spectral range of the CCD was 200 - 1060 nm, and had a dynamic range of 16 bits (65000:1). The operating temperature for the CCD was -120°C. The readout noise was 7 electrons and the dark charge was 2 electrons / pixel / hour according to the specifications [38]. The light exposure time on the CCD was controlled by a shutter mounted on the spectrometer in front of the entrance slit. The shutter was controlled by

# CHAPTER 9

## LASER-INDUCED FLUORESCENCE EXPERIMENTS

The laser-induced fluorescence set-up and tuneable UV OPO were used to obtain initial fluorescence measurements of several samples. Fluorescence for different purities of water and comparisons between different concentrations of quinine sulphate were studied. The LIF signal to noise ratio (SNR) was measured and compared to that obtained using a commercial spectrofluorometer system.

### 9.1 LIF Measurements of Quinine Sulphate

A sample of quinine sulphate at a concentration of 1000 ppb was placed in the LIF set-up in order to obtain the spectral output. The spectrometer used the 150 g/mm grating to see

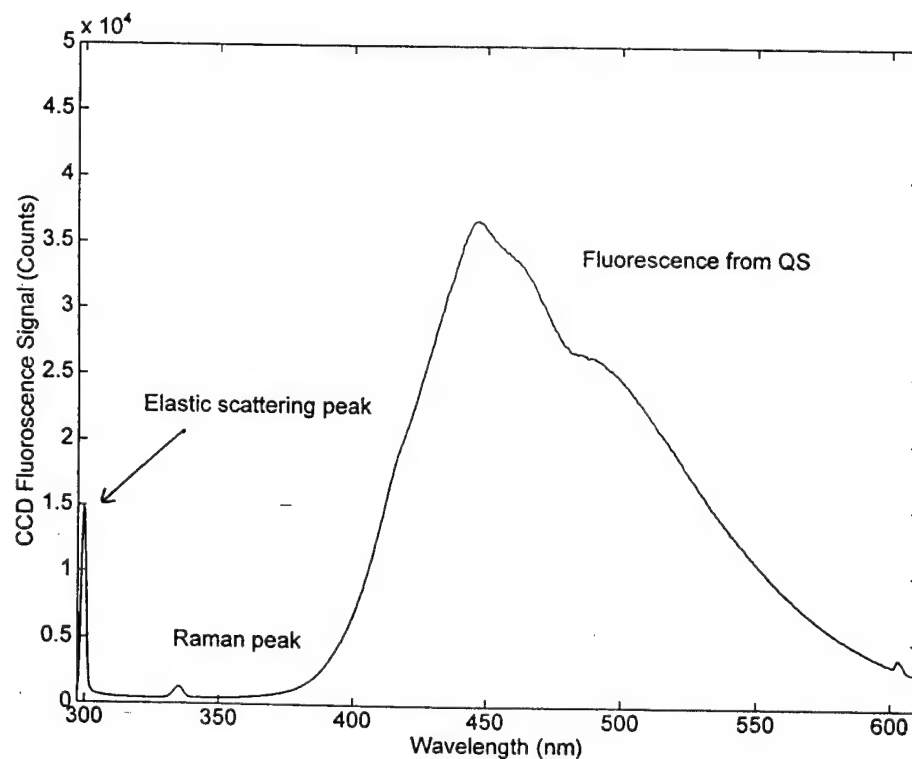


**Figure 9.1** Spectrum showing fluorescence from quinine sulphate (QS) and elastic and Raman scattering peaks. The quinine sulphate had a concentration of 1000 ppb. The excitation wavelength was 300 nm. The exposure time was 20 s and UV laser energy was 0.15 mJ per pulse.

as wide a spectral range as possible and the grating was positioned at 450 nm, close to the emission peak of QS. The entrance slit of the spectrometer was 50  $\mu\text{m}$  wide and the excitation wavelength was 300 nm.

Figure 9.1 shows the measured raw fluorescence spectrum of the quinine sulphate sample. As can be seen, the fluorescence maximum is at 447 nm and the peak from elastic scattering at the excitation wavelength is at 300 nm. The Raman peak from water at 337 nm can also be seen. The small peak at 600 nm is the second order elastic scattering. The measured output of the UV OPO was about 1 mJ per pulse. It should be added that the laser energy in the LIF experiments were unfortunately measured in front of the aperture as the power meter also served as a beamblock between sets of experiments. This has caused an error in the energy values of a factor not more than 2. This, however, does not affect the qualitative results presented in this thesis. The laser energy for the photodestruction measurements in Chapter 9.2 was measured after the aperture.

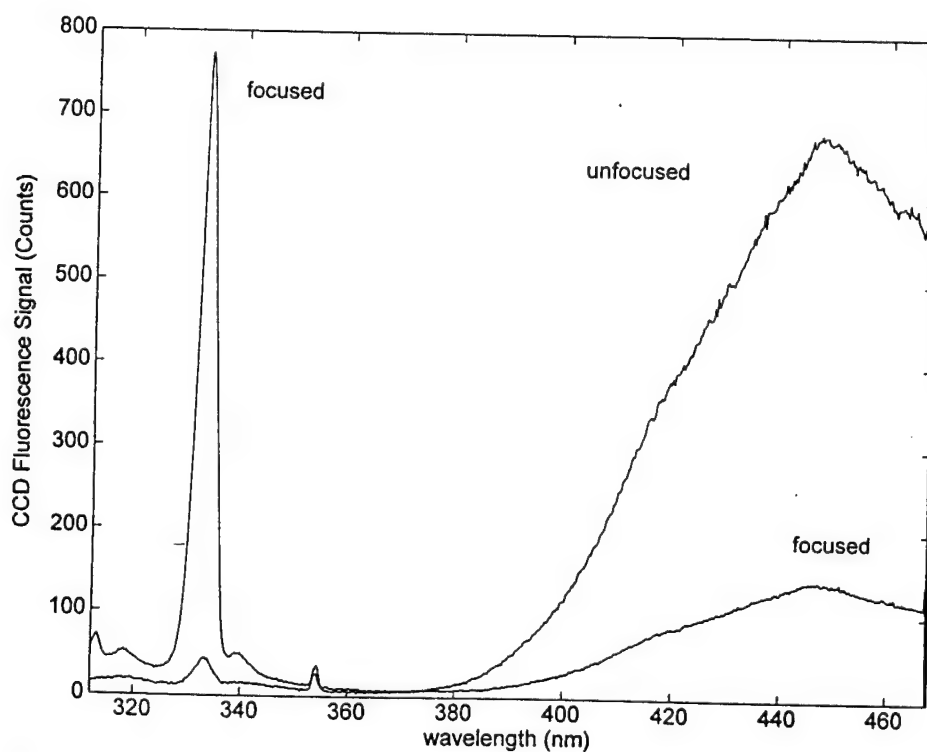


**Figure 9.2** QS fluorescence spectra for focused and unfocused UV laser beam. The quinine sulphate concentration was 1000 ppb and both curves were normalised for UV energy and exposure time. The excitation wavelength was 300 nm. The exposure time was 10 s in both cases but the pump beam energy was 1 mJ per pulse for the focused beam and 0.5 mJ per pulse for the unfocused beam.

the detector controller. The detector controller was interfaced to a PC computer through a Princeton Instruments, Inc. signal board, as shown in Fig. 8.5.

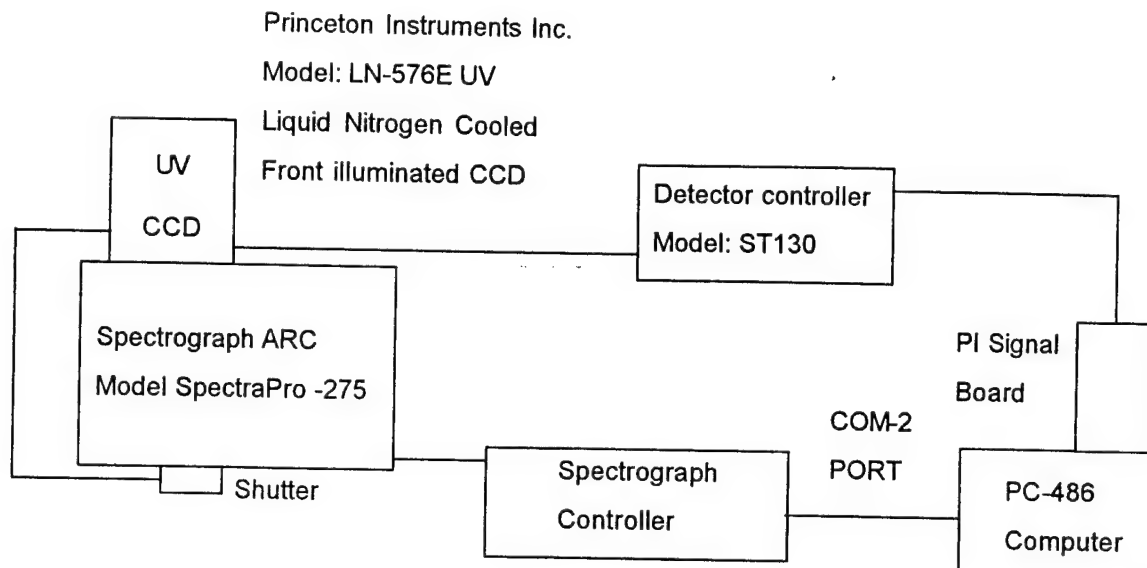


Figure 8.5 Schematic of spectrometer and detector interface with computer.

## 8.5 Spectrometer Control and CCD Data Processing

The spectrometer and the CCD detector were controlled using a 486DX2-50MHz computer with 8MB RAM and 240MB harddrive. A software package CSMA (CCD Spectrometric Multichannel Analyzer) which came with the CCD controller was used to collect signals, subtract background noise and store data. The data files were exported to ASCII files for further signal analysis in MATLAB. The software also allowed hardware as well as software "binning" (i.e. adding several pixels together) of the CCD signals. Hardware "binning" allows on-chip grouping of pixels along a whole spectral line. This results in a larger photon collection area while the readout noise remains constant. Hardware "binning" is used for low light spectrometric applications. Software "binning" is used for higher light levels to increase SNR and the dynamic range. Hardware "binning" for higher light levels results in pixel saturation. In our experiments, the vertical columns of pixels were "binned" in 578 superpixels each the size of 384x1 pixels.

## **8.6 Alignment and Calibration Procedures of Spectrometer and CCD**

The CCD camera was placed in the exit focal plane of the spectrometer through use of a mounting holder from Princeton Instruments. Since all vertical pixels were "binned" together it was important that these were perpendicular to the spectrometer plane to avoid reduced spectral resolution. This was accomplished by using a mercury lamp in place of the cuvet and observing the image of the mercury emission lines on the CCD. Good alignment was established by rotating the CCD camera until the lines on the image were vertical on the monitor.

The spectrometer was aligned with the collection optics and the cuvet using a small light bulb as a point source. These alignment procedures are given in Appendix A because they are different than the normal alignment used for a two slit spectrometer.

The spectrometer wavelength was calibrated using the lines from the mercury lamp (404.66 nm, 407.78 nm, 435.83 nm).

time of 0.09 s was chosen to ensure that only one pulse was captured per acquisition. The risk of capturing half a pulse was considered zero because of the pulse length (5 ns). The readout time was 0.3 s. A decrease in laser energy was obtained by detuning the frequency doubler crystal slightly.

As can be seen in Figs. 9.4 and 9.5, the photodestruction is faster for a higher laser energy. The fluorescence intensity was halved after only one or two laser pulses. It is also possible that saturation of the optical transitions could have occurred simultaneously with the above photobleaching of the QS. However, this is very hard to estimate or quantify because of lack of knowledge of the upper state lifetimes of the QS.

### 9.3 Noise Measurements

The noise level is a determining factor when it comes to maximise the sensitivity of the system. A list of possible noise sources in LIF experiments is shown in Table 9.1.

**Table 9.1** List of possible LIF noise sources

List of possible noise sources
Electronic noise
Shot noise
Scattering (Elastic and Raman)
Scattering in grating
Spill-over effects in CCD caused by pixel saturation
Fluorescence from optics and solvent
Stray light from lab environment

The signal is collecting noise when transferred from the CCD to the computer via the detector controller. The electronic noise level is independent to exposure time and was measured with the spectrometer shutter closed. The electronic DC bias was about 210 counts as shown in Fig. 9.6. The electronic noise was automatically subtracted from our acquired spectra by CSMA software.

The main stray light source in our set-up was the tripled Nd:YAG laser light that was scattered all over the room. The stray light from the laboratory environment was reduced con-

siderably by using light baffles and black curtains during the experiments. All measurements were performed with the room lights turned off.

The laser light is elastically scattered in the sample and gives a bright signal into the spectrometer and detector. Besides that the elastic scattering peak itself is hitting the CCD, which is easy to subtract, it increases other noise due to scattering in the grating and pixel spill-over effect.

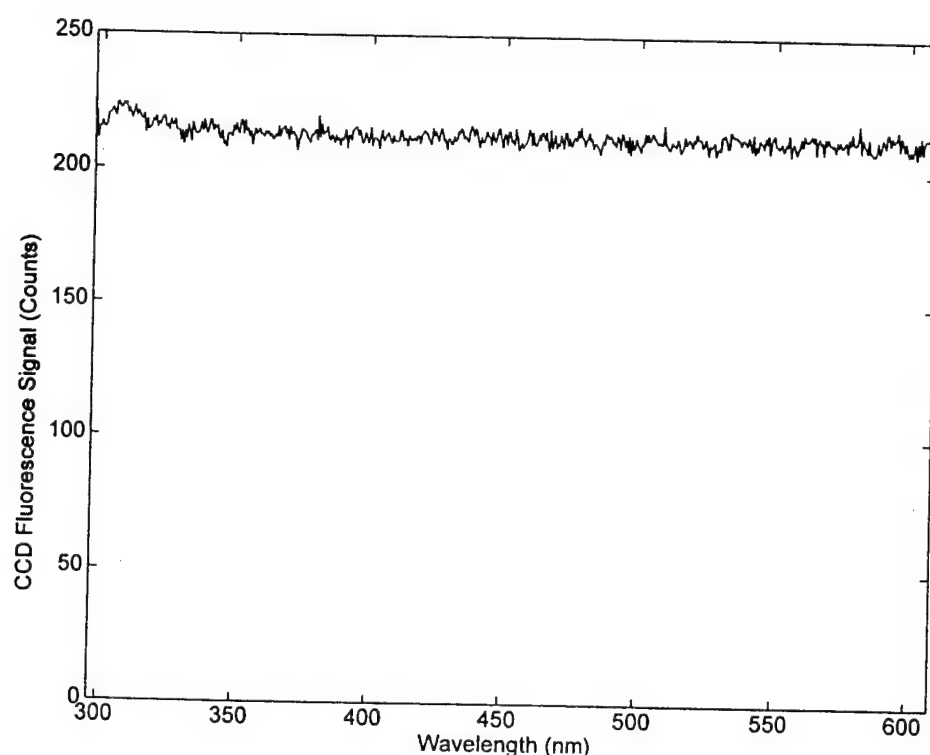


**Figure 9.6** Noise output of CCD detector with spectrometer shutter closed showing DC bias of electronics and noise fluctuations.

Since the samples used contained water, Raman scattering from water occurred. The Raman shift in water is  $3640\text{ cm}^{-1}$ . The Raman peak causes an increase of other noise due to scattering in the grating and pixel spill-over effects.

In the low UV region, UV fused lenses may fluoresce. Fluorescence in a calcium fluoride lens was observed at excitation wavelength below 310 nm. The fluorescence occurred as two peaks at 320 and 340 nm.

As shown in Fig. 9.7, the QS solvent ( $\text{H}_2\text{SO}_4$ ) is also fluorescing, with an emission peak at 350 nm. This fluorescence is not a severe problem since it is the QS emission peak at 450 nm that is of interest. A weak fluorescence signal can be seen but the spill-over (discussed

## 9.2 Measurements of Photobleaching and Possible Saturation

The effect of the laser excitation intensity was studied. Figure 9.2 shows the fluorescence signal and the Raman peak for an unfocused laser beam compared to a focused laser beam for a QS sample of 1000 ppb. The focused beam was obtained by using a lens of focal length 25 mm in place of the aperture. The short focal length was used to diminish the volume of high intensity to avoid burning the cuvet. As can be seen in Fig. 9.2, the fluorescence signal decreased as the excitation intensity increased. However, a larger fluorescence signal should have been obtained with the focused laser beam as indicated by the increased Raman signal. The results indicate that some form of saturation (photo-induced chemical bleaching or absorption saturation) must have occurred.

It is known that QS is photosensitive and degrades after a couple of hours in room light [55]. This was studied further in our experiments and is discussed in the following section.

An estimation of the photodestruction effect was obtained by acquiring signals sequentially. The experiments were made at an excitation wavelength of 250 nm where the highest UV output energy was measured and where QS has its excitation peak as shown in Fig. 7.6. The photodestruction was studied at the emission peak at 447 nm. Figure 9.3 shows the de-

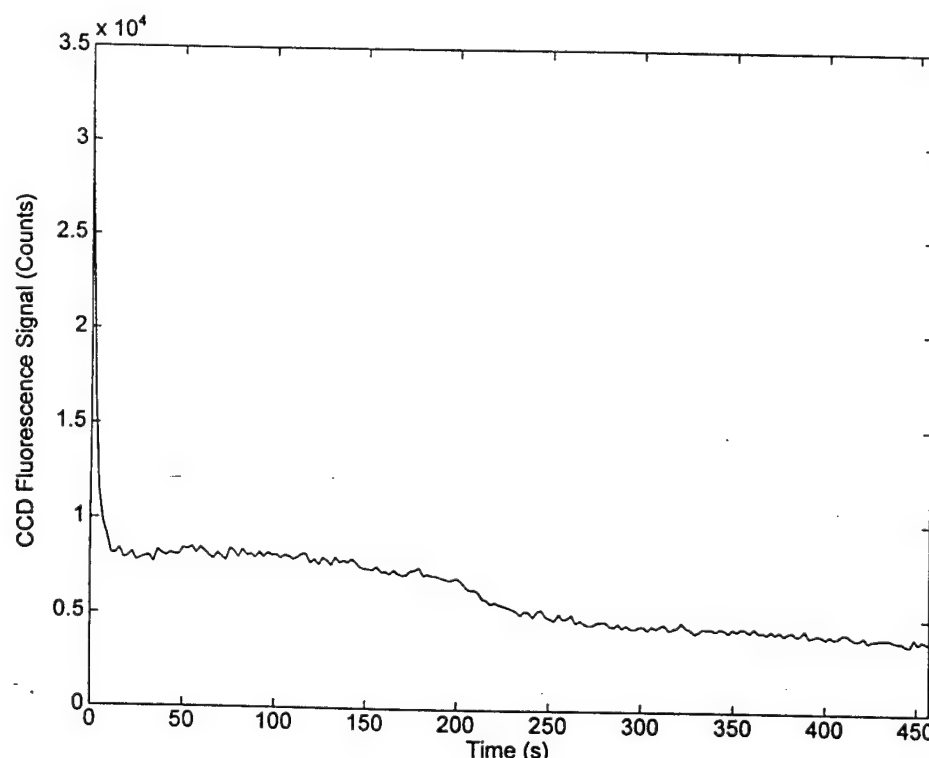


**Figure 9.3** Temporal decay of LIF signal from QS solution (1000 ppb) showing bleaching occurring after a few seconds with laser excitation at 250 nm. The laser energy was 4.0 mJ per pulse.

gradation of the QS over 460 s. The exposure time was 2 s and 200 sequential measurements were obtained. The laser energy through the sample in this experiment was 4.5 mJ per pulse. The accuracy was  $\pm 5\%$  since a two-second shot may contain 19 - 21 laser pulses.

Figures 9.4 and 9.5 show the photodestruction at a higher time resolution. An exposure

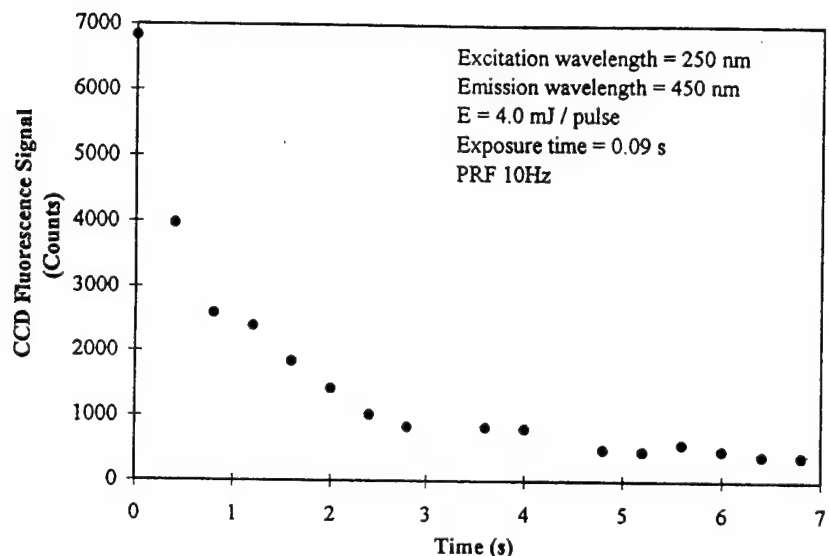


**Figure 9.4** Temporal decay of LIF signal from QS solution showing bleaching for low power excitation (4.0 mJ / pulse).

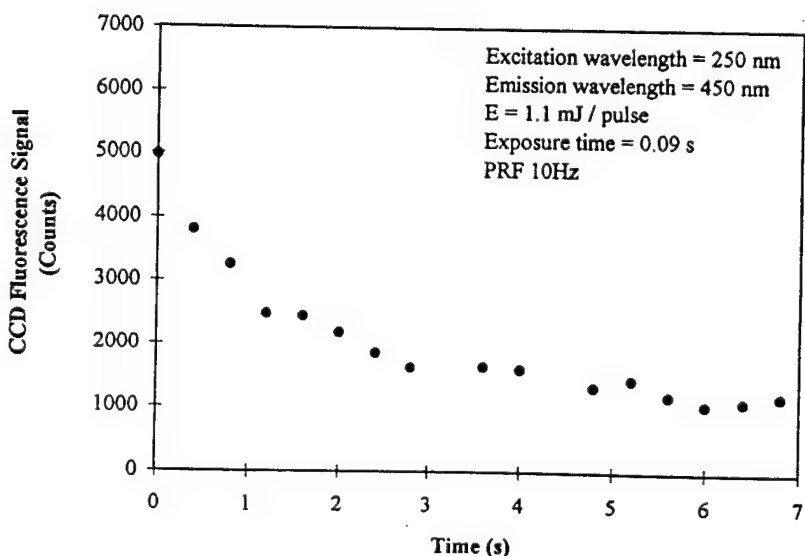


**Figure 9.5** Temporal decay of LIF signal from QS solution showing bleaching for high power excitation (1.1 mJ / pulse).

below) and scattering noise seem to be a greater problem.

The grating in the spectrometer is not perfect, meaning that some of the incoming light is scattered throughout the spectrometer. The scattering distribution over the CCD is a complex function of the angle.

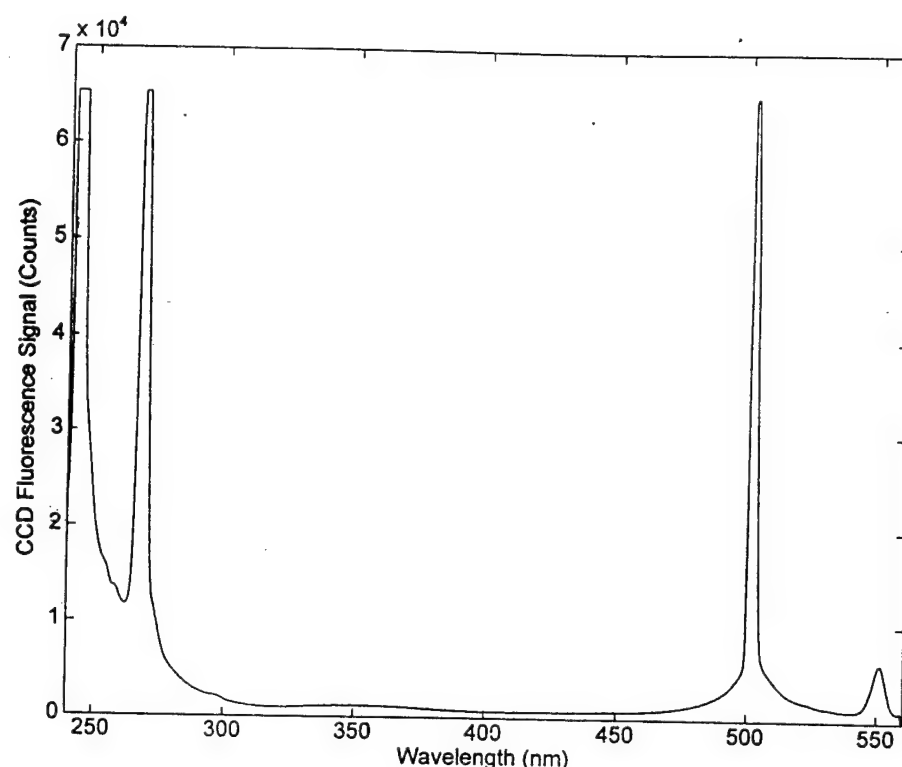


**Figure 9.7** LIF fluorescence spectrum of  $\text{H}_2\text{SO}_4$  solvent. The excitation wavelength was 250 nm. The fluorescence peak was at 350 nm. The peaks at 500 nm and 550 nm were the second order elastic and Raman scattering peaks.

There are two main noise sources in a CCD, shot noise and pixel spill-over effects.

Shot noise is caused by the discreteness of electronic charge [41] and was measured for different exposure times. Figure 9.8 shows typical shot noise from our CCD detector (cf. Fig. 9.6). This spectrum was obtained over a 20 s exposure time and the UV laser beam blocked. The fluctuation of the signal was about  $\pm 6$  counts.

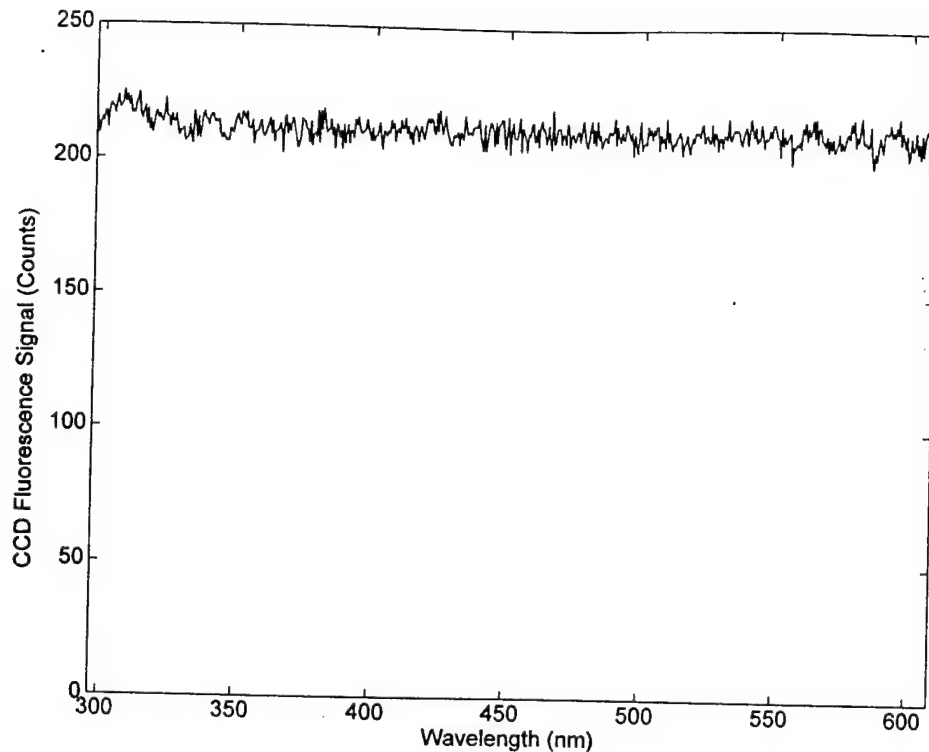


**Figure 9.8** Background shot noise from CCD detector with laser beam blocked but shutter open to room light showing the DC bias level of 210 counts and a fluctuating noise component of  $\pm 6$  counts.

Spill-over effects occur when the CCD pixels cannot hold all the electrons but the electrons are spilling over to nearby pixels. The spill-over probability increases when the number of electrons is close to the maximum in a pixel.

#### 9.4 Measurements of Different Water Samples

Fluorescence spectra were obtained for some different water samples with a laser excitation wavelength of 300 nm. The spectra were normalised for exposure time and UV energy.

Figure 9.9 shows a LIF fluorescence spectrum for ultra pure distilled water. This sample was used to investigate spill-over effects, scattering noise and fluorescence from the optics. A very small fluorescence signal was seen around 400 nm. This may be fluorescence from the lenses. Figure 9.10 shows the measured LIF fluorescence spectrum for normal tapwater. A fluorescence signal was seen with peaks at 420 nm and 500 nm. This result follows previous experiments [14]. It can also be seen that the elastic scattering is higher in the tapwater than the ultra pure distilled water, probably due to more Mie scattering.

the case and this indicates that differences in the photodestruction may have occurred due to the differences in the UV laser exposure time. Figure 9.14 shows a fluorescence spectrum for QS 10 ppb. The fluorescence signal is about a tenth of the fluorescence signal for QS 100 ppb. Figure 9.15 shows a fluorescence spectrum for QS 1 ppb and the SNR is estimated to about 1. The sensitivity limit is in this concentration range for our set-up. By comparing Figs. 9.12-15, it can be concluded that the four QS samples have been differently affected by the UV laser light.

Changing grating and augmenting the exposure time may move the sensitivity limit further down in concentration. Reducing the laser intensity would increase the sensitivity since the photodestruction would be reduced.

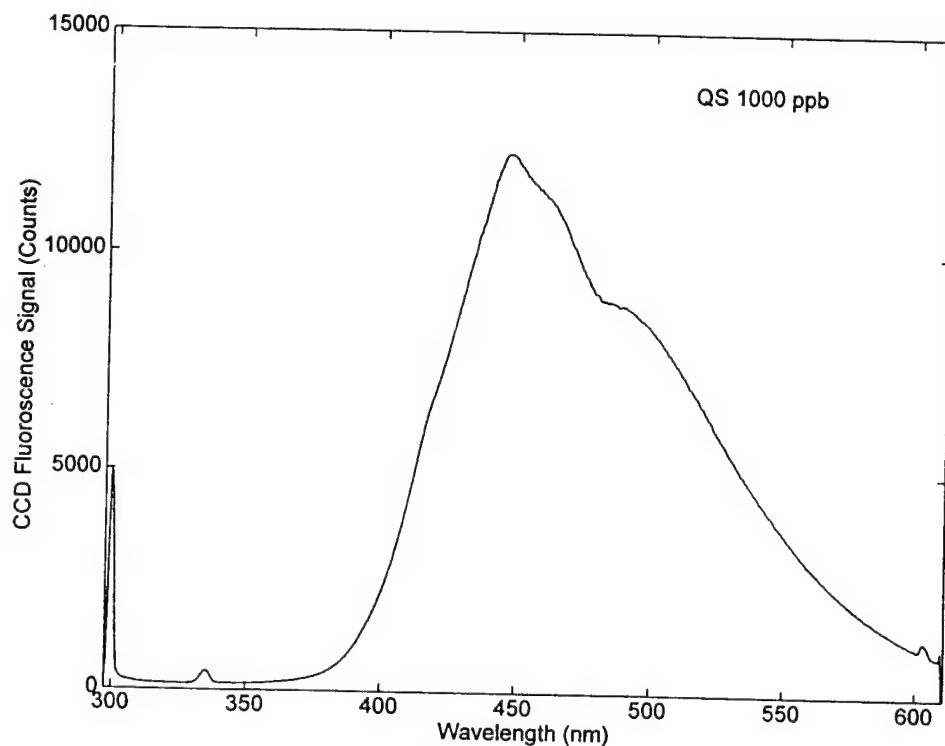


**Figure 9.12** LIF normalised fluorescence spectrum for quinine sulphate 1000 ppb. The excitation wavelength was 300 nm. The UV energy was 0.15 mJ and the exposure time was 20 s. The peak at 600 nm was the second order of elastic scattering.

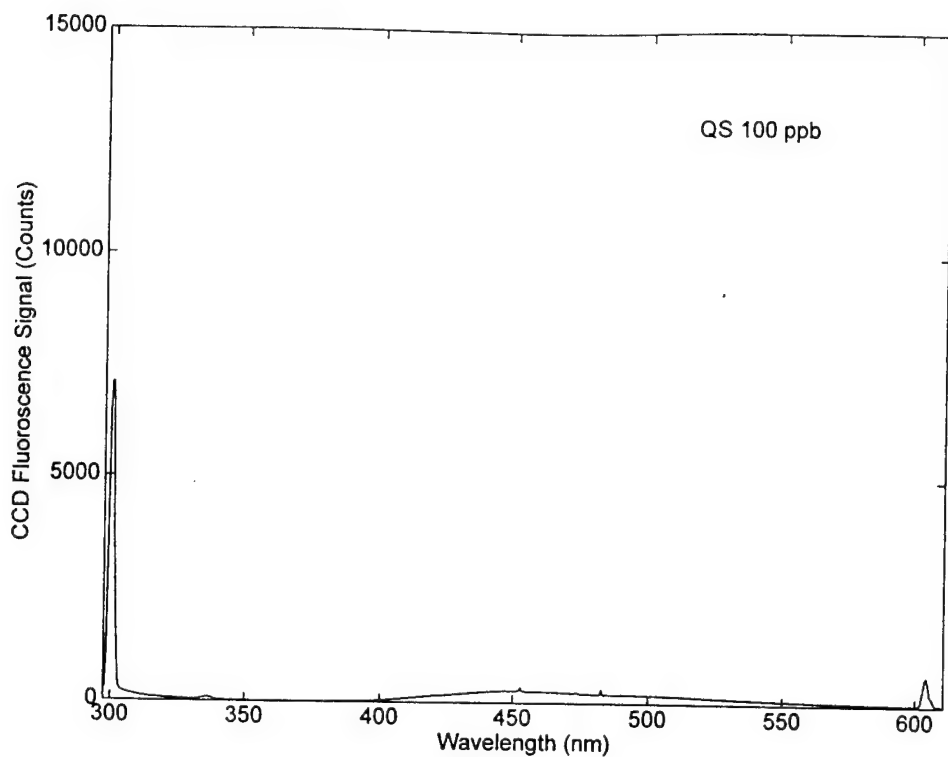


**Figure 9.13** LIF normalised fluorescence spectrum for quinine sulphate 100 ppb. The excitation wavelength was 300 nm. The UV energy was measured to 0.23 mJ and the exposure time was 40 s. The peak at 600 nm was the second order of elastic scattering.

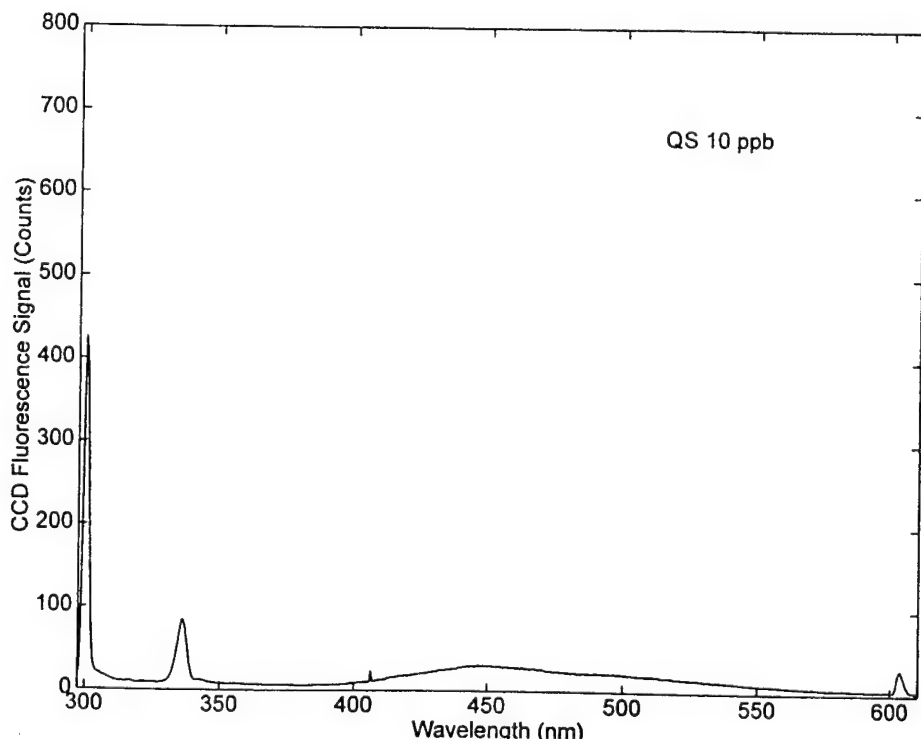


**Figure 9.14** LIF normalised fluorescence spectrum for quinine sulphate 10 ppb. The excitation wavelength was 300 nm. The UV energy was measured to 0.23 mJ and the exposure time was 80 s. The peak at 600 nm was the second order of elastic scatter-

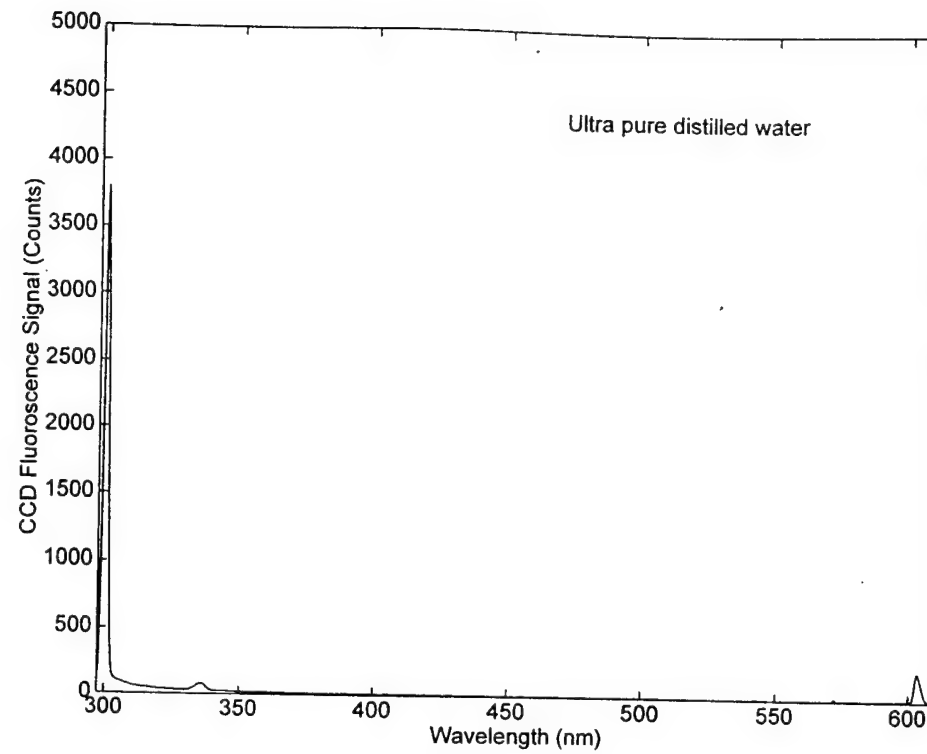


**Figure 9.9** LIF fluorescence spectrum of ultra pure distilled water normalised to laser energy and exposure time. The excitation wavelength was 300 nm. The UV energy was 0.3 mJ and the exposure time was 40s. The peak at 600 nm was the second order of elastic scattering.

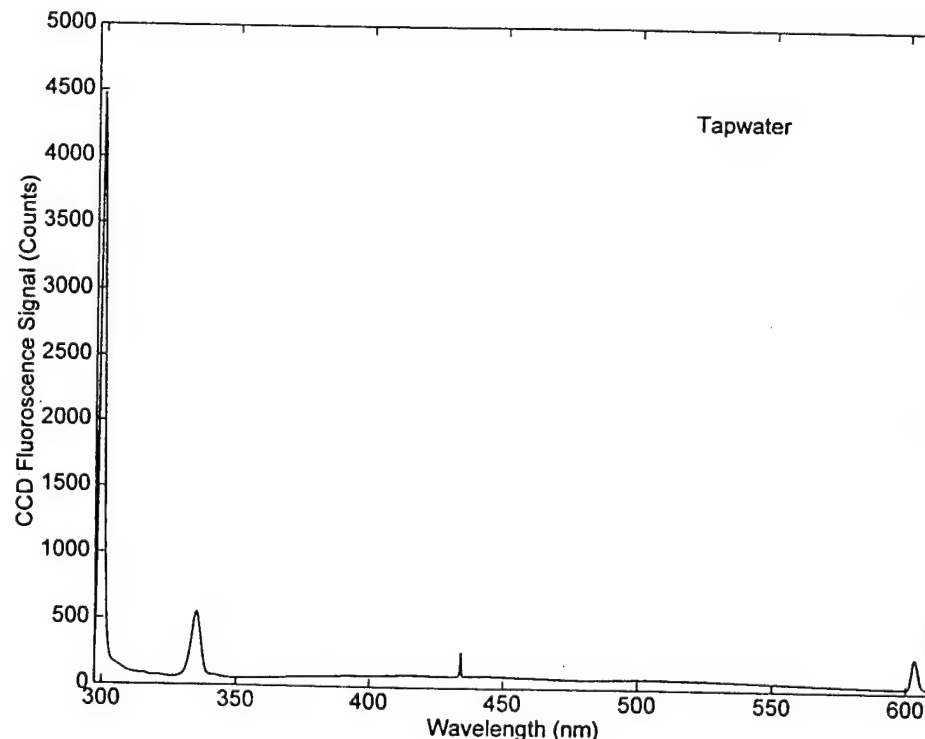


**Figure 9.10** LIF normalised fluorescence spectrum of tapwater. The excitation wavelength was 300 nm. The UV energy was 0.5 mJ and the exposure time was 20 s. The peak at 600 nm was the second order of elastic scattering.

A normalised LIF fluorescence spectrum of QS solvent ( $\text{H}_2\text{SO}_4$ ) is shown in Fig. 9.11. The elastic scattering peak is remarkably low and the fluorescence signal is negligible compared to the two previous spectra. These two factors are characteristic for solvents used in fluorescence experiments.

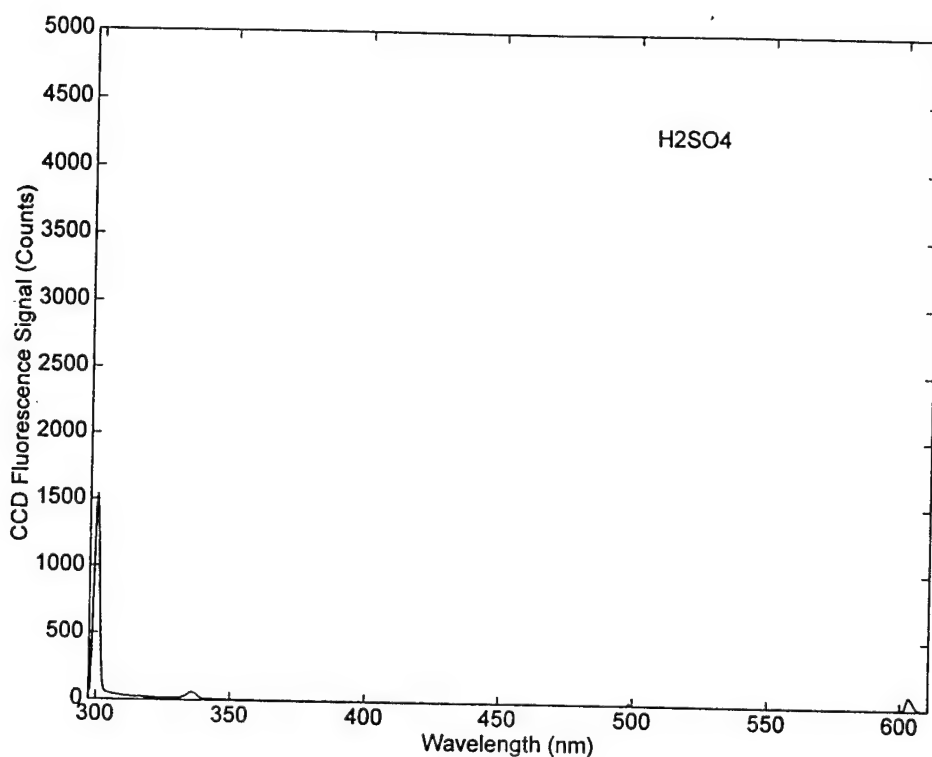


**Figure 9.11** LIF normalised fluorescence spectrum of  $\text{H}_2\text{SO}_4$ . The excitation wavelength was 300 nm. The UV energy was 0.3 mJ and the exposure time was 40 s. The peak at 600 nm was the second order of elastic scattering.

## 9.5 Comparison between Different Concentrations of Quinine Sulphate

A survey of LIF fluorescence for different concentrations of QS was done to estimate the sensitivity of the LIF system. All the spectra were acquired within the first minute the sample was exposed to the UV laser light. The excitation wavelength was 300 nm and the exposure time varied between 20 and 160 seconds. The fluorescence spectra were normalised to laser energy and exposure time. Figure 9.12 shows the fluorescence spectrum for QS 1000 ppb. The fluorescence spectrum for QS 100 ppb is shown in Fig. 9.13. Since the fluorescence signal is proportional to the concentration, the emission peak for QS 100 should be 1/10 (~1200 counts) of the emission peak for QS 1000 ppb. However, as seen in the data, this is not

species in water. These results indicate that while further studies are required to better quantify the technique, the system has the potential to be a very sensitive instrument for EEM analysis. In addition, the sensitivity is expected to improve by several orders of magnitude with the elimination of the photobleaching through use of a flow type cell and the use of signal averaging of several (100's) laser excitation pulses.

## CHAPTER 10

### TUNEABLE UV LASER EXCITATION-EMISSION MATRIX (EEM) EXPERIMENTS

In this chapter, the results from two experiments using the EEM technique are presented. Two species have been investigated namely quinine sulphate (QS), 1000 ppb and a plastic contaminant dissolved in water. The OPO was tuned to 12 wavelengths between 220 nm - 330 nm and data was acquired for the two samples consecutively at every wavelength.

#### 10.1 EEM for Quinine Sulphate

Figure 10.1 shows the measured EEM fluorescence spectrum for QS 1000 ppb. For every new wavelength, a new and fresh sample was placed in the cuvet holder. The acquisition was done within the first 30 seconds the sample was exposed to laser light. The exposure time varied between 1.5 and 10 seconds to maximise the signal without saturating the CCD. The

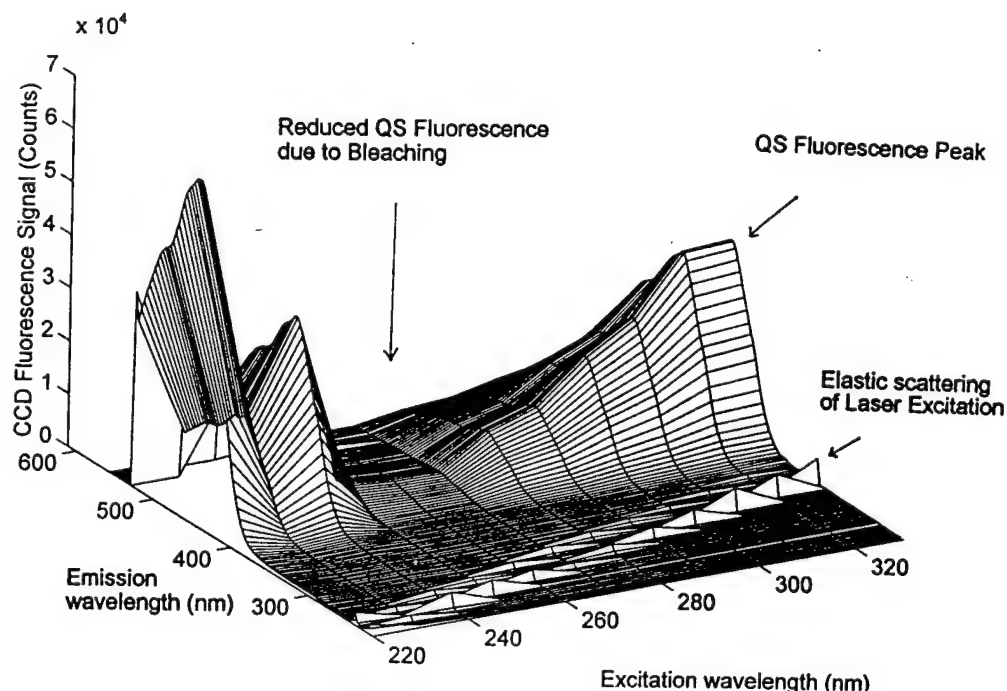


**Figure 10.1** Measured EEM spectrum for quinine sulphate (1000 ppb), using 12 different excitation wavelengths from the tuneable UV OPO.

spectrum was normalised to the exposure time and laser energy. When comparing the EEM to Fig. 7.7, it is noticeable that the supposed peak at excitation wavelength 250 nm is missing. This is due to bleaching of the sample. 250 nm is a resonant wavelength for QS and the laser energy was considerably higher at this wavelength compared to the rest of the wavelength range as shown in Fig. 4.15. Raman and elastic scattering can be seen in the foreground. The scattering seemed fairly constant over the excitation wavelength range.

## 10.2 EEM for a Plastic Contaminant Dissolved in Water

Figure 10.2 shows an EEM fluorescence spectrum for a plastic contaminant in water (digycidal ether of bis-phenol A). The exposure time varied between 2 and 80 seconds to maximise the signal without saturating the CCD. The EEM spectrum has been normalised to

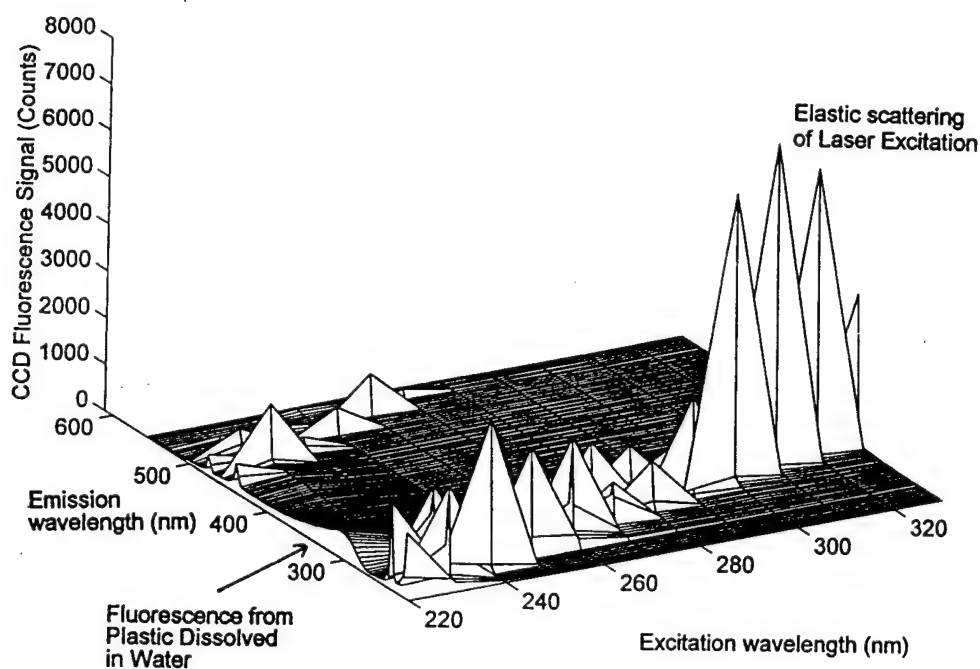


**Figure 10.2** Measured EEM spectrum for plastic contaminant in water, using 12 different excitation wavelengths from the tuneable UV OPO.

exposure time and laser energy. The elastic scattering had a very high peak which resulted in a fairly poor fluorescence signal. The emission peak can be seen around 300 nm, which agrees well with Fig. 7.5 [14].

In summary, the above EEM spectra show that the UV OPO system is able to obtain fairly complex spectra and should be a useful tool for future spectroscopic detection of trace

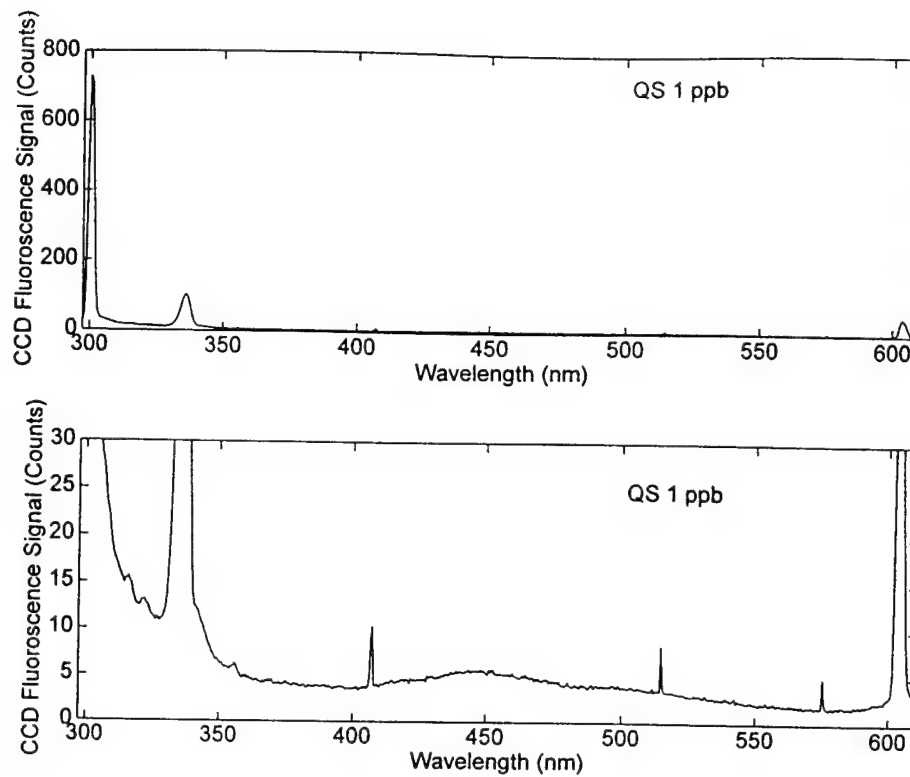


**Figure 9.15** LIF normalised fluorescence spectrum for quinine sulphate 1 ppb. The excitation wavelength was 300 nm. The UV energy was measured to 0.26 mJ and the exposure time was 160 s. The peak at 600 nm was the second order of elastic scattering.

## 9.6 Signal to Noise Ratio

Table 9.2 shows a preliminary value of the estimated signal-to-noise ratio (SNR) for the measurements made with this LIF experimental set-up. The emission peak at 447 nm was used as the signal level and the noise bias at 365 nm was subtracted. The appropriate normalised value of N was obtained from the  $\pm 0.6$  fluctuation in the counts shown in Fig. 9.15 near 365 nm (QS 1 ppb). This is consistent with using the  $\pm 6$  counts of the raw noise fluctuation in Fig. 9.8 after being normalised to a typical laser energy of 0.25 mJ and a 40 s exposure time. The SNR is about an order of magnitude smaller than that for the spectrofluorometer system. This is due to several things. First, the equipment is totally different and a double monochromator reduces the scattering noise. A PMT often has a better SNR than a CCD camera. The laser emits a higher light intensity but also bleaches the sample and may saturate the absorption transitions in the sample. The former effect destroys the sample and thus the actual concentration of the sample is not known. The latter effect makes the laser energy normalisation more difficult.

**Table 9.2** Measured peak fluorescence values and estimated relative S/N values for different samples of QS compared to that using a commercial spectrofluorometer system [14]. The signal levels were deduced after subtracting the bias level at 365 nm.

	LIF System		Spectrofluorometer (Commercial System)			
Light source	UV OPO Laser		Xenon lamp			
Spectrometer	Single monochromator		Double monochromator			
Detector	LN cooled CCD		PMT			
Sample	Laser Power (mJ)	Fluorescence Signal @ 447 nm	Noise Bias Level @ 365 nm	Corrected Signal Level	Estimated S/N with $N \approx 0.6$	Estimated S/N with Xenon lamp
1000 ppb	0.15	12300	220	12080	20000	
100 ppb	0.23	270	9.02	261	434	5420
10 ppb	0.23	30.6	6.30	24.3	40	480
1 ppb	0.26	5.50	4.32	1.18	2.0	4.8

Note: For LIF  $S_{MAX} = 65000$  counts

It should be added that further LIF experiments using our set-up but conducted by others at USF after the conclusion of our thesis experiments were better able to quantify the above results. Instead of integrating the CCD detected fluorescence signal (and thus integrating the photobleaching effects) they modified the CCD software to only detect a single LIF pulse. They were able to measure the fluorescence signal of a fresh sample of QS for different concentration levels. These results showed a linear relationship of the fluorescence signal with concentration and intensity and a LIF SNR of 1 at a concentration of QS of about 0.1 ppb.

## CHAPTER 11

### CONCLUSIONS AND FUTURE WORK

Our studies have covered the development and optical testing of a new, tuneable UV OPO/LIF system which we used to obtain preliminary EEM fluorescence spectra of QS, water and plastic compounds. These results demonstrated for the first time the use of a tuneable UV OPO for the EEM detection of plastic trace contaminants in water and the observation of photobleaching under certain conditions.

Future studies will include the quantification and improvement of the sensitivity of the system, and the role which photobleaching plays in the measurements.

There are several ways to reduce the photobleaching; diminish the laser intensity, decrease the time the sample is exposed to the laser light, avoid critical wavelenghts or continuously renew the sample. The photobleaching occurs from the excited energy state and is thus a strong function of the laser intensity [28]. As can be seen in Fig. 10.1, the photobleaching seems to have a maximum around 250 nm and is due to the absorption peak QS has at this wavelength which follows the above theory. The effect of the laser intensity on the photobleaching will be further investigated at USF to make the concentration determination more accurate.

Decreasing the exposure time is an alternative to reducing the photobleaching. Further analysis at USF has shown an increased sensitivity by a factor of 10 by detecting fluorescence from only one laser pulse. By using a flowcell, the sample will be exchanged between the pulses and several fluorescence signals may be summarised without increasing the photobleaching, thus increasing the sensitivity.

After evaluation of the photobleaching, the saturation of optical transitions should be estimated to further increase the accuracy of the method.

The noise can be reduced in several ways. A double grating spectrometer reduces the scattered light and an optical filter can be placed in front of the CCD to reduce the elastic scattering from the sample.

The data processing was not optimised in our set-up. This could, however, be done by interfacing the MOPO control box with the PC computer controlling the detector. Thus, the

spectra can easily be normalised to the relative laser intensity at different wavelengths achieved from the pyroelectric detector in the OPO frequency doubler.

31. R. A. Mathies and K. Peck, *Optimization of High-Sensitivity Fluorescence Detection*. Anal. Chem., **62**, 1786 (1990)
32. R. A. McClatchey et al., Handbook of Optics. McGraw-Hill (1978)
33. R. M. Measures, *Laser Remote Chemical Analysis*. John Wiley&Sons, Inc., New York (1988)
34. R. M. Measures, *Laser Remote Sensing Fundamentals and applications*. John Wiley&Sons, Inc., New York (1984)
35. Optics Guide 4. Melles Griot
36. Grating specifications. Milton Roy, ARC
37. S-G. Pettersson, S. Borgström, and H. Hertz, *Optisk Teknik*. KFS (1994)
38. Operation Manual for Detector Controller and CSMA. Princeton Instruments Inc.
39. L. J. Radziemski et al., *Laser Spectroscopy and its applications*, Marcel Dekker, Inc., New York (1987)
40. D. A. Roberts, *Simplified Characterization of Uniaxial and Biaxial Nonlinear Optical Crystals: A Plea for Standardization of Nomenclature and Conventions*. IEEE Journal of Quantum Electronics, **28**, 2057 (1992)
41. W. D. Rogatto, *The Infrared and Electro-Optical Systems Handbook*. Vol. III, Infrared Information Analysis Center and SPIE Optical Engineering Press (1993)
42. Y. R. Shen, *The Principles of Nonlinear Optics*. John Wiley and Sons (1984)
43. A. Siegman, *Lasers*. University Science Books (1986)
44. R.C. Smith and K.S. Baker, *Optical properties of the clearest natural waters (200nm-800nm)*. Appl. Optics, **20**, 177 (1981)
45. MOPO-FDO, Frequency Doubler Option, User's Manual, Spectra-Physics
46. Pulsed Nd:YAG Lasers, User's Manual, GCR Series, Spectra-Physics
47. Quanta-Ray MOPO-730 Optical Parametric Oscillator, Instruction Manual, Spectra-Physics
48. Model 6300, Model 6350, Instruction Manual, Spectra-Physics
49. SPEX Operation Manual
50. S. Svanberg, *Atomic and Molecular Spectroscopy*. Springer-Verlag, Berlin (1992)

51. S. Svanberg, *Laser fluorescence spectroscopy in environmental monitoring*. Optoelectronics for Environmental Science, Plenum Press, New York (1990)
52. V. Sychra, *Atomic fluorescence spectroscopy*. Van Nostrand Reinhold Co., Prague (1975)
53. Chuang L. Tang, Walter R. Rosenberg, Takashi Ukashi, Randall J. Lane, and L. Kevin Cheng. "Optical parametric Oscillators. Proceedings of the IEEE", 365 (1992)
54. E. D. Traganza, *Fluorescence excitation and emission spectra of dissolved organic matter in sea water*. Bul. of Marine Science, **19**, 897
55. R. A Velapoldi and K.D Mlelenz, *A Fluorescence Standard Reference Material: Quinine Sulfate Dihydrate*. National Measurements Laboratory, National Bureau of Standards (1980)
56. N. B. Vogt, and C. E. Sjoegren, *Investigation of chemical and statistical methods for oil-spill classification*. Anal. Chem. Acta, **222**, 135 (1989)
57. A. Yariv, *Quantum Electronics*, John Wiley and Sons (1967)
58. J. Y. Zhang, J.Y. Huang, Y. R. Shen, and C. Chen, *Optical parametric generation and amplification in barium borate and lithium triborate crystals*. J. Opt. Soc. Am. B, **10**, 1758 (1993)
59. F. C. Zumsteg, J. D. Bierlein, T. E. Gier,  *$K_xRb_{1-x}TiOPO_4$ : A new nonlinear optical material*. J. Appl. Phys., **47**, 4980 (1976)

## List of References

1. Operation Manual for SpectraPro -275, Acton Research Corporation
2. P. S. Andersson, S. Montán, and S. Svanberg, *Remote Sample Characterization Based on Fluorescence Monitoring*. Appl. Phys. B, **44**, 19 (1987)
3. J. A. Armstrong, N. Bloembergen, J. Ducuing, and P.S. Pershan, *Interactions between Light Waves in a Nonlinear Dielectric*. Phys. Rev., **127**, 1918 (1962)
4. N. P. Barnes, *Tunable Mid-Infrared Sources Using Second-Order Nonlinearities*. International Journal of Nonlinear Optical Physics, **1**, 639 (1991)
5. M. Born and E. Wolf, *Principles of Optics*. Pergamon Press (1964)
6. R. W. Boyd, *Nonlinear Optics*. Academic Press, Inc. (1992)
7. E. S. Casseddy, M. Jain, *A Theoretical Study of Injections Tuning of Optical Parametric Oscillators*. IEEE Journal of Quantum Electronics, **15**, 1290 (1979)
8. C. Chen, Y. Wu, A. Jiang, B. Wu, G. You, R. Li, and S. Lin, *New nonlinear optical crystal: LiB<sub>3</sub>O<sub>5</sub>*. J. Opt. Soc. Am. B, **6**, (1989)
9. D. K. Cheng, *Field and Wave Electromagnetics*. Addison-Wesley Publishing Company (1991)
10. L. K. Cheng, W. R. Bosenberg, and C.L. Tang, *Broadly tunable optical parametric oscillation in β-BaB<sub>2</sub>O<sub>4</sub>*. Appl. Phys. Lett., **53**, 175 (1988)
11. P. G. Coble, *Characterization of marine and terrestrial DOM in seawater using excitation-emission matrix spectroscopy*. Marine Chemistry, **51**, 325 (1996)
12. P. G. Coble, S. A. Green, N. V. Blough, and R. B. Gagosian, *Characterization of dissolved organic matter in the Black Sea by fluorescence spectroscopy*. Nature, **348**, 432 (1990)
13. P. G. Coble C. A. Schultz, and K. Mopper, *Fluorescence contouring analysis of DOC Intercalibration Experiment samples: a comparison of techniques*. Marine Chemistry, **41**, 173 (1993)
14. Paula G. Coble, Personal information 1996
15. R. C. Eckerdt, H. Masuda, Y. X. Fan, and R. L. Byer, *Absolut and Relative Nonlinear Optical Coefficients of KDP, KD\*P, BaB<sub>2</sub>O<sub>4</sub>, LiIO<sub>3</sub>, MgO:LiNbO<sub>3</sub>, and KTP Measured by Phase-Matched Second-Harmonic Generation*. IEEE Journal of Quantum Electronics, **26**, 922 (1990)

16. Y. X. Fan, R. C. Eckardt, and R. L. Byer, *Visible BaB<sub>2</sub>O<sub>4</sub> optical parametric oscillator pumped at 355 nm by a single-axial-mode pulsed laser*. Appl. Phys. Lett., **53** (1988)
17. A. Fix, T. Schröder, R. Wallenstein, J. G. Haub, M. J. Johnson, and B. J. Orr, *Tunable β-barium borate optical parametric oscillator: operating characteristics with and without injection seeding*. J. Opt. Soc. Am. B, **10**, 1744 (1993)
18. A. Giordmaine, and R.C. Miller, *Tunable coherent parametric oscillation in LiNbO<sub>3</sub> at optical frequencies*. Phys. Rev. Lett., **14**, 973 (1965)
19. G. G. Guilbault, *Practical fluorescence; theory, methods, and techniques*. M. Dekker, New York (1973)
20. H. Haken, and H. C. Wolf, *The Physics of Atoms and Quanta; Introduction to Experiments and Theory*. Springer Verlag (1993)
21. Editor D. R. Lide, *Handbook of Chemistry and Physics*, 74th Edition, CRC Press (1993-1994)
22. J. G. Haub, R. M. Hentschel, M. J. Johson, and B. J. Orr, *Controlling the performance of a pulsed optical parametric oscillator: a survey of techniques and spectroscopic applications*. J. Opt. Soc. Am. B, **12**, 2128 (1995)
23. E. Hecht, *Optics*. Addison-Wesley, 1987
24. L. A. W. Gloster, I. T. McKinnie, Z. X. Jiang, T. A. King, J. M. Boon-Engering, W. E. van der Meer, and W. Hogervorst. *Narrow-band β-BaB<sub>2</sub>O<sub>4</sub> optical parametric oscillator in a grazing-incidence configuration*. J. Opt. Soc. Am. B, **12**, 2117 (1995)
25. Jerlov, and Nielsen, *Optical Aspects of Oceanography*. Academic Press, London (1974)
26. G.F. Kirkbright, *Atomic absorption and fluorescence spectroscopy*. Academic Press, London (1974)
27. H. Komine, *Average-power scaling for ultra-violet β-barium borate and lithium triborate optical parametric oscillators*. J. Opt. Soc. Am. B, **10**, 1751 (1993)
28. G. Kristensson, *Elektromagnetsik vågutbredning*. KFS (1994)
29. N. M. Kroll, *Parametric Amplification in Spatially Extended Media and Applications to the Design of Tunable Oscillators at Optical Frequencies*. Phys. Rev., **127**, 1207 (1962)
30. B. C Johnson, V. J. Newell, J. B. Clark, and E. S. McPhee, *Narrow-bandwidth low-divergence optical parametric oscillator for nonlinear frequency-conversion applications*. J. Opt. Soc. Am. B, **12**, 2122 (1995)

## **ACKNOWLEDGEMENTS**

We would like to express our most sincere thanks to Dr. Dennis Killinger and Dr. Sune Svanberg who made this thesis work possible. They have been a great help throughout the work. We would also like to thank Dr. Paula Coble and her staff at the Department of Marine Science at University of South Florida (USF) for their expertise help in issues concerning marine chemistry. Bert Johnson and Steve Katnik at Spectra-Physics have been very helpful and patient with all our OPO and laser questions which we appreciate. We would also like to thank everybody in the lab and the Physics Department at USF for their support and friendship. Finally, we thank the Department personnel in Lund for all their help and assistance.